NOVA
NOVA SCHOOL OF
SCIENCE & TECHNOLOGY

ANDREIA SOFIA DA SILVA MENDES

BSc in Mechanical Engineering Sciences

ON THE USE OF VIRTUAL SENSING FOR DAMAGE IDENTIFICATION ON WIND TURBINE BLADES

MASTER IN MECHANICAL ENGINEERING

ON THE USE OF VIRTUAL SENSING FOR DAMAGE IDENTIFICATION ON WIND TURBINE BLADES

ANDREIA SOFIA DA SILVA MENDES

BSc in Mechanical Engineering Sciences

Adviser: Tiago Alexandre Narciso da Silva
Assistant Professor, NOVA University Lisbon

Examination Committee

Chair: Raquel Albuquerque Soares Brás de Almeida
Assistant Professor, NOVA University Lisbon

Rapporteur: Hugo Filipe Diniz Policarpo
Assistant Professor, Naval School

Adviser: Tiago Alexandre Narciso da Silva
Assistant Professor, NOVA University Lisbon

On the use of virtual sensing for damage identification on wind turbine blades

Acknowledgements

The academic journey one takes and experiences should be everlasting, and this dissertation marks only one more step in mine. Neither would have been possible without the help and companionship of some along the way, to whom I'm grateful for.

To the NOVA University Lisbon, the NOVA School of Science and Technology, the Department of Mechanical and Industrial Engineering (DEMI) and especially the Structural Mechanics group and teaching staff, for providing the best education and foundation for my future.

To Daniela and Maria, for being present in every step of the way, for never bringing lunch, for always being my examples and helping me grow alongside you.

To Fábio, Francisco, Rodrigo and Ana, for sharing my frustrations, for your listening ears and for always leaving me thoughtful and understood.

To the friends and classmates who I've crossed paths with, for walking this journey with me.

To my family, for their constant support, and to my parents and sister, for giving me the room I need to fail and always helping me get back on my feet.

My many and deepest thanks.

"The time is always right to do what is right."

(Martin Luther King Jr.)

Abstract

With the recent growth in size and complexity of wind turbine blades, continuous monitoring has become imperative in reducing costs and downtime by preventing difficult maintenance and repair works. Using ambient excitation, dynamic responses are analysed with Vibration-based Structural Health Monitoring (VSHM) techniques to obtain modal parameters such as natural frequencies, mode shapes and damping ratios. For that, this study uses two output-only modal identification methods to identify those modal parameters from numerical and experimental responses, aiming to detect changes in those parameters attributed to damage. Using a cantilever beam, damage is introduced as a localized change in mass where, in the presence of damage, natural frequencies may present a decrease in value. Given the limitations of placing physical sensors on wind turbine blades, specially the ones in-service, this study uses measured responses from the structure and estimated ones at unmeasured locations, using data estimation techniques to create virtual sensors. The present objectives are to compare two modal identification methods and two response estimation ones, with the goal of understanding whether the use of virtual sensors improves damage detectability. The numerical comparison between the modal identification methods showed that both are capable of identifying modal parameters close to each other and to the numerical model ones. The results from both methods indicate that using virtual responses increases damage detectability for the same set of measurements. One of the methods provides more consistent results but requires higher computational efforts, whereas the other is much faster and simpler to use, although its results present slight variations. The comparison between the response estimation methods showed that, even with limitations, both were capable of identifying close modal parameters to each other. The experimental application validated the conclusions found with the numerical results, from all the methods' behaviour to the enhancement of damage detectability.

Keywords: Wind turbine blades, Vibration-based Structural Health Monitoring, Damage detection, Virtual sensing

Resumo

Com o recente crescimento em dimensão e complexidade de pás de turbinas eólicas, a sua monitorização contínua torna-se imperativa na redução de custos e de inatividade ao prevenir manutenções e reparações difíceis. Usando excitação ambiente, as respostas dinâmicas são analisadas através de técnicas de Monitorização da Condição Estrutural baseada em Vibrações para obter parâmetros modais, tais como frequências naturais, modos de vibração e fatores de amortecimento. Para tal, este estudo usa dois métodos de identificação modal para identificar esses parâmetros de respostas numéricas e experimentais, procurando detetar neles alterações atribuídas a dano. Numa viga encastrada, dano é introduzido como a alteração local de massa onde, na sua presença, frequências naturais podem apresentar uma redução de valor. Dadas as limitações na colocação de sensores físicos nas pás, especialmente naquelas em funcionamento, este estudo usa respostas medidas da estrutura e estima respostas em localizações não medidas através de técnicas de estimação com sensores virtuais. Os objetivos passam por comparar dois métodos de identificação modal e dois de expansão de respostas, procurando perceber se a utilização de sensores virtuais melhora a detetabilidade de dano. A comparação numérica entre os métodos de identificação modal mostrou que ambos são capazes de identificar parâmetros modais próximos entre si e aos do modelo numérico. Os resultados de ambos indicam que a utilização de respostas virtuais melhora a detetabilidade de dano para os mesmos conjuntos de respostas. Um dos métodos obtém resultados mais consistentes mas exige maior esforço computacional, enquanto que o outro é mais rápido e simples de usar, mas os resultados apresentam ligeiras variações. A comparação entre métodos de expansão de respostas mostrou que, mesmo com as limitações, ambos são capazes de identificar parâmetros modais próximos entre si. A aplicação experimental validou as conclusões obtidas através dos resultados numéricos, desde dos comportamentos dos métodos até à intensificação da detetabilidade de dano.

Palavras-chave: Pás de turbinas eólicas, Monitorização da Condição Estrutural baseada em Vibrações, Deteção de dano, Sensoriamento virtual

Contents

List of Figures

xi

xiv

List of Tables

Acronyms

AUC Area Under the Curve

DOF Degree of Freedom

EFDD Enhanced Frequency Domain Decomposition
EMA Experimental Modal Analysis

FDD Frequency Domain Decomposition
FEM Finite Element Model
FFT Fast Fourier Transform
FRF Frequency Response Function

IFFT Inverse Fast Fourier Transform

MAC Modal Assurance Criterion
MD Mahalanobis Distance
MDE Modal Decomposition and Expansion
MDOF Multi Degree of Freedom

OMA Operational Modal Analysis

PSD Power Spectral Density

ROC Receiver Operating Curve

SDOF Single Degree of Freedom

SEREP	System Equivalent Reduction Expansion Process
SHM	Structural Health Monitoring
SSI	Stochastic Subspace Identification
SSI-COV	Covariance-driven Stochastic Subspace Identification
SVD	Singular Value Decomposition
VSHM	Vibration-based Structural Health Monitoring

1

Introduction

The present work inserts itself in a research group studying damage detection through the analysis of structural dynamic responses, where this thesis focuses on damage detection and detectability on wind turbine blades. When damage occurs, it is expected that the dynamic characteristics of a structure will change [1], and as such, by continuously monitoring the responses of that structure, those changes can be detected soon enough to prevent unnecessary maintenance procedural costs and catastrophic outcomes [2].

In this Chapter, a contextualization is first given on the recent and steady growth of wind energy and wind turbines, the need for continuous monitoring of these structures and how damage is detected. Secondly, the methodology followed in this thesis is explained, following all the steps necessary to perform damage detection and assess damage detectability considering recent techniques, like virtual sensing. The final Sections set the objectives of this work and the thesis outline.

1.1   Contextualization

The industrial growth of any country depends on creating a balance between energy production and its consumption. The production of energy in turn depends on the availability of renewable and non-renewable energy resources [3].

In the *2030 Climate Target Plan* set by the European Commission, the proposal to cut greenhouse gas emissions by at least 55% by 2030 sets Europe on a responsible path to becoming climate neutral by 2050 [4]. As such, and given the heavy pollution always associated with fossil-fuel consumption, renewable energy resources emerge as the best alternatives with the most potential, as they are constantly replenished naturally, meaning a non-ending supply of eco-friendly sources of energy available to humanity [3].

Being a renewable and green source of energy, wind energy has become a pillar of the energy systems in many countries and is recognized as a reliable and affordable source of electricity [5], given the vast potential that wind has to offer. All countries in the world experience wind and wind turbines can be set up onshore or offshore. Outside of hydroelectric power, wind energy consumption is the largest component of the renewable energy category [6].

Wind turbines convert the kinetic energy of the wind to electrical energy using a set of equipment from which the blades are one of the key components. Having been studied for over forty years, the most recent research techniques into wind turbine technology are producing stronger, lighter and more efficient blades for the turbines [7].

Accordingly, wind turbines have become physically larger so as to meet the rising capacity needs, and this increase in size generates problems as far as maintenance and repair procedures are concerned. Figure 1.1 represents the growth in wind turbines and blades so far, as well as prospects for future sizes and capacities. It is operationally difficult and hazardous to perform inspection and maintenance. Furthermore, the usually remote location of the wind turbines generates added difficulty [2].
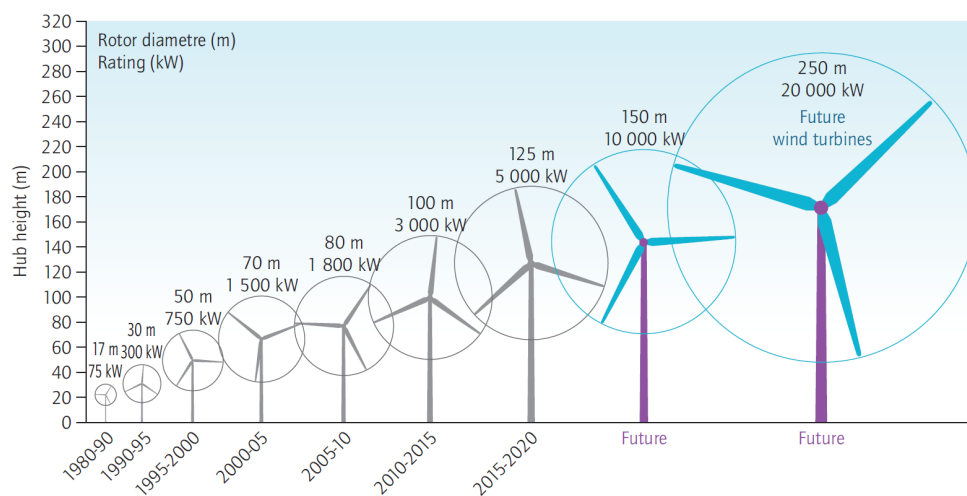
Figure 1.1. Wind turbine growth in size and capacity since 1980 and prospects for future sizes and capacities, from [8].

Unlike conventional power stations, wind turbines are exposed to highly variable and harsh weather conditions that could cause damage to the structures, including calm to severe winds, tropical heat, lightning, arctic cold, hail, and snow [9]. Although damage can occur to any component or part of the wind turbine, blade failures are a prominent structural failure and are the most common type of damage that occurs in a wind turbine system, all the while being shown that blade damage is the most expensive type of damage to repair and requires

considerable repair time [5]. As such, it becomes important to detect damage before the blade fails catastrophically, which could destroy the entire wind turbine [10].

That being said, Structural Health Monitoring (SHM) has gained much interest lately as it offers enhanced safety, optimized inspection cycles by the use of non-destructive testing techniques (like Acoustic Emissions or the Thermal Imaging Method), minimization of downtime and avoidance of extended damage [2]. Besides damage detection, routinely monitoring wind turbines also ensures good condition to ultimately provide reliable power generation [11]. Furthermore, the application of SHM in supporting the process of lifetime extension has also been studied recently – for example in [12, 13] –, directly aiding the reduction of the heavy pollution associated with these equipments when they reach their end-of-life, as they are currently considered unrecyclable because of the materials of which they are made – composite materials [14].

1.1.1 Structure Health Monitoring: definition and techniques

In [15], Sohn and Farrar define SHM as "the process of implementing a damage detection strategy for engineering infrastructure related to aerospace, civil and mechanical engineering". Damage can be generally understood as changes introduced into a system that adversely affect its current or future performance, therefore implying that damage is not meaningful without a comparison between two different states of the system, the reference state being an assumed initial and often undamaged one [16].

However, many damage detection methods are either visual or localized experimental methods which require that the vicinity of the damage is known *a priori*, and that those locations are readily accessible for inspection [16]. So, for more efficient detection, the need arises for monitoring on a global basis.

When applied to wind turbine systems, many SHM techniques can be performed on any of their components. A few of those techniques are as follows [11, 17]:

- Analysis of oil pressure or temperature;
- Power generation or performance monitoring;
- Strain measurements;
- Vibration analysis.

This thesis will focus on the last item, also known as Vibration-based Structural Health Monitoring (VSHM). The basis of VSHM is to analyse a structure's dynamic responses, and obtain and monitor the structure's modal properties, in a technique called Modal Analysis.

1.1.2 Modal Analysis on Structure Health Monitoring

The basic premise of Modal Analysis that damage will alter the stiffness, mass or energy dissipation properties of a system, which, in turn, alter the measured dynamic response of that system. Damage identification based upon changes in dynamic responses is one of the few methods that monitor changes in the structure on a global basis [15], and because of their somewhat simple implementation on any size structure – needing only ambient excitation and sensors to measure the dynamic responses –, they are among the earliest and most common damage detection methods used [18].

The basic concept behind these methods is that modal parameters, notably natural frequencies, mode shapes and damping ratios are functions of the physical properties of the structure (mass, stiffness and damping). Therefore, changes in the physical properties, such as reductions in stiffness resulting from the onset of cracks or loosening of a connection, will cause detectable changes in the modal properties [16, 19, 20].

So, considering any structure, by using periodically sampled dynamic response measurements from an array of sensors, extracting damage-sensitive features from those measurements and statistically analysing those features, it is possible to determine that structure's current state of structural health [18].

1.1.3 Damage detection

Damage detection methods can be divided into 4 levels, as introduced by Rytter in [1]:

Level 1 Methods that determine whether damage is present – *detection*;
Level 2 Methods that determine the location of the damage – *localization*;
Level 3 Methods that quantify the severity of the damage – *assessment*;
Level 4 Methods that predict the remaining service life of the structure – *consequence*;

Most VSHM methods can be classified as Level 1 or Level 2, which usually do not make use of a structural model, and Level 3 when requiring the coupling with a structural model of the structure. Level 4 methods are usually associated with specific fields of fracture mechanics, fatigue-life analysis or structural design assessment [21, 19].

As for the modal properties used in the damage detection, the most common are natural frequencies, mode shapes and damping ratios. The most popular of these are natural frequencies, as they are easily determined with a relatively high level of accuracy, and are sensible to both local and global damage [1].

4

Traditionally, the presence of damage is related to a decrease in stiffness and thereby in the natural frequencies [1]. As most wind turbine blades are made of composite materials [14], a specific application should also be considered where damage detection was tested in panels made of composite materials and, in accordance to the initial statement, natural frequency reduction was also reported [22].

As well as changes to natural frequencies (reduction, for this property), changes to mode shapes and damping ratios are also to be expected. It is important to monitor these changes through a SHM system that analyses periodic dynamic responses, as they reflect developing damage and accelerate structure degradation [23].

1.1.4 Operational Modal Analysis

During the first several decades of research in the field of structural dynamics, structures were often excited by measured forces (using actuators, shakers or impact hammers), responses were measured and modal parameters were extracted from the identified system model, in what is known as Experimental Modal Analysis (EMA). However, these experimental methods are not suited for large civil and mechanical engineering structures because the contribution of artificial excitation forces to the total response of the structure is rather low [24]. Besides, in terms of continuous monitoring of structural health, it is unthinkable to have an artificial excitation, as testing would become too costly [25].

As such, new damage detection methods have been developed to make use of the ambient excitation that is always present, even when the input forces are unknown and unmeasured. The subsequent Modal Analysis, using only output measurements (like strains, displacements, velocities or accelerations, among others), is known as Operation Modal Analysis (OMA).

OMA techniques can be divided into time domain and frequency domain, and their distinction will be explained in the next Chapter.

1.1.5 Response estimation and virtual sensing

In the context of VSHM methods, many types of sensors can be used to sample the dynamic responses, depending on the properties to be extracted. The most common are accelerometers, strain gauges and fiber optic cables [26].

As seen in Subsection 1.1.2, the first step in the monitoring of a structure's health is sampling dynamic response measurements from an array of sensors. So, damage detection is

heavily dependant on the sensors placed on the structure.

However, given the continuous growth in size of wind turbines and their blades and the harsh conditions they operate in, placing sensors along the length of the blades becomes a difficult task, as sensors are usually costly, need to be maintained and are sometimes unreliable [27]. Also, many of these equipments are already in service, making the placement of sensors an increasingly difficult task. That being said, a great alternative arises in the use of response estimation and virtual sensing.

Physical sensors placed on the structure take direct measurements, and virtual sensors (also known as smart sensors) take the readings from the physical sensors and estimate responses of the structure in locations where there are no physical sensors. Virtual sensors need system models or transfer functions to process the data from physical sensors, so the model accuracy is critical [27].

Many response estimation techniques exist, but they all have the same objective, and that is to use physical sensing data and a suitable model to predict information in difficult or inaccessible areas of interest [27]. In other terms, response estimation techniques (either reduction or expansion) are used to estimate the motion at all degrees of freedom (DOFs) of a Finite Element Model (FEM) of the structure based on measured information, under the minimal assumption that sensor measurements can be linearly related to finite element DOFs [28].

In a recent study by Roberts et al. – see [29] –, dynamic responses were measured in several locations and using an expansion method, responses were estimated to a virtual location. By placing a real, physical sensor in that same location to verify the results, it was proven that it is possible to predict the responses at any point in a structure.

1.2 Methodology

The process of detecting and assessing damage in wind turbines blades envolves many steps and techniques applied in several stages. This Section focuses on the sequence followed, at the end of which a flowchart is presented to synthesise and connect those steps.

1.2.1 Ambient excitation and modal parameter extraction

Following the distinction made between EMA and OMA in Subsection 1.1.4, OMA methods can be defined as output-only or stochastic system identification methods, where the (ambient) forces are modelled as stochastic quantities with unknown parameters but with known behaviour (for instance, white noise time series with zero mean and unknown covariances) [24].

Any Modal Analysis technique – experimental, operational or combined – is performed in three steps [24]:

1. Data collection;
2. System identification;
3. Determination of the modal parameters.

As per the collection of data, time-series responses are used. The present work uses computer generated responses from a simulated model, for it allows a more controlled environment for the adjustment of necessary parameters. As to validate the methods used and results obtained, the present thesis will, in a secondary stage, use (real) experimental responses from an experimental application.

The system identification can be defined as the construction of a mathematical system model from measured data. Many system models exist, depending on the system identification used: time domain or frequency domain identifications, or even parametric or non-parametric identifications. One of the system models used in this study is the FEM, which provides an approximation of the system with a limited number of DOFs [30].

The final step is the extraction of the modal parameters and their respective analysis, as to determine the state of the structure [24]. The modal identification methods used in this study are the focus of Chapter 2.

So, after applying the ambient forces to the structure, the time responses are registered and the modal parameters can be extracted, as seen in Subsection 1.1.2.

1.2.2 Model Updating

With the modal parameters identified from the structure's time responses, it becomes imperative to assess if the system model identified is in fact correctly representing the structure. Because FEM is used in this study to model the structure, that assessment is then performed

through Finite Element (FE) Model Updating.

The main goal of Model Updating methods is to correct the inaccurate parameters in the numerical model so as to obtain a better agreement between numerical results and test data or, in other words, minimize the error between those two sets of data [31]. For that, functions need to be formulated between those two sets, as a way to quantify their correlation.

An example of that is the Modal Assurance Criterion (MAC), which is computed between the mode shapes of each analysis. Introduced by Allemang and Brown in [32], MAC compares the directions of two eigenvectors (mode shapes) based on their inner product and yields values between 0 and 1 (where 0 represents poor correlation and 1 good correlation), arranged in matrix form: diagonal values are expected to be closest to 1 and non-diagonal values are expected to be closest to 0. It is one of the best known methods in model validation of structural dynamics [33].

In the present study, a set value of 0.8 has to be achieved in order to obtain the estimation of time responses to locations where no measurements are taken. At this point, the goal is to assess if adding these response estimations (or virtual responses) enhances the damage detectability. The response estimations methods used in this study are approached later on, being the focus of Chapter 3.

1.2.3 Damage detectability

With the goal of comparing damage detectability between using only (real) time responses and using real and virtual time responses, healthy testing and training (undamaged) references are taken to establish a baseline. Then, damage is applied to a single element of the FEM, corresponding to a specific DOF, as the localized percentual reduction of the second moment of area. Increasing damage is applied, resulting in a set of damaged responses, all with the same number of observations.

Modal parameters are then extracted for each set of responses. Next, the obtained natural frequencies are used by the Mahalanobis Distance (MD) – introduced in [34] as a metric to determine the distance between a point and a distribution –, in this case to determine the distance between every damaged measurement and the healthy reference ones, allowing for a good indication of the damage extent [35].

With the increasing extent of damage, it is expected that MDs increase as well, so the greater the damage, the greater the MDs obtained. However, the MD alone might not be a sufficient tool in assessing the damaged condition of the structure, and applying a threshold

value to the obtained MDs allows for a better classification of the current state of the structure. As such, when plotting the MDs for each set of responses, their values are expected to increase and to exceed the threshold established. For this study, the threshold is defined for all sets of responses as the mean value of the MDs from the healthy measurements plus its standard deviation.

Afterwards, in order to quantify the damage detectability, two additional steps are taken. Firstly, the Receiver Operation Curve (ROC) – introduced in [36] – is obtained, which plots the test *sensitivity* over *1-specificity* – in other terms, true positive rate is plotted against false positive rate, respectively. When comparing undamaged measurements with the healthy reference, the ROCs are expected to fit a diagonal line (meaning the healthy references are being considered as such), serving a threshold to the damaged reference ROCs, which are expected to fit closest to the top left corner. Secondly, for each ROC the respective Area Under the Curve (AUC) is determined. When comparing undamaged measurements to the healthy reference, ROCs should fit a diagonal line and so, AUCs should have a value close to 0.5 (representing half the area of the plot). When comparing damaged measurements to the healthy reference, ROCs should approximate the top left corner, and as such AUCs should increase and approximate the value of 1. The greater the value of the AUC, the better the test results – in this case, the greater the damage and its detectability.

Following all these steps, the full methodology for this study is complete. For a better (and visual) understanding, a flowchart of said methodology is presented in Figure 1.2, where two modal identification methods and two response estimation methods are compared – blue shaded boxes for the first case and green shaded box for the second case. The comparison between results obtained is presented in Chapter 4.

1.3 Problem statement

Applying four different methods – two modal identification and two response estimation methods – allows the comparison between four separate sets of results, and thus it permits a more thorough analysis of the damage detection on this case, where a cantilever beam is used to model a wind turbine blade.

Given the limitations of placing physical sensors on wind turbine blades, only four sensors will be used in this study. Can damage be detected using only those four sensors? And can damage detection be improved when adding responses estimated at unmeasured locations to those measurements taken? Results obtained from each method are compared, as to better understand which methods are better suited for the structure considered in this study.
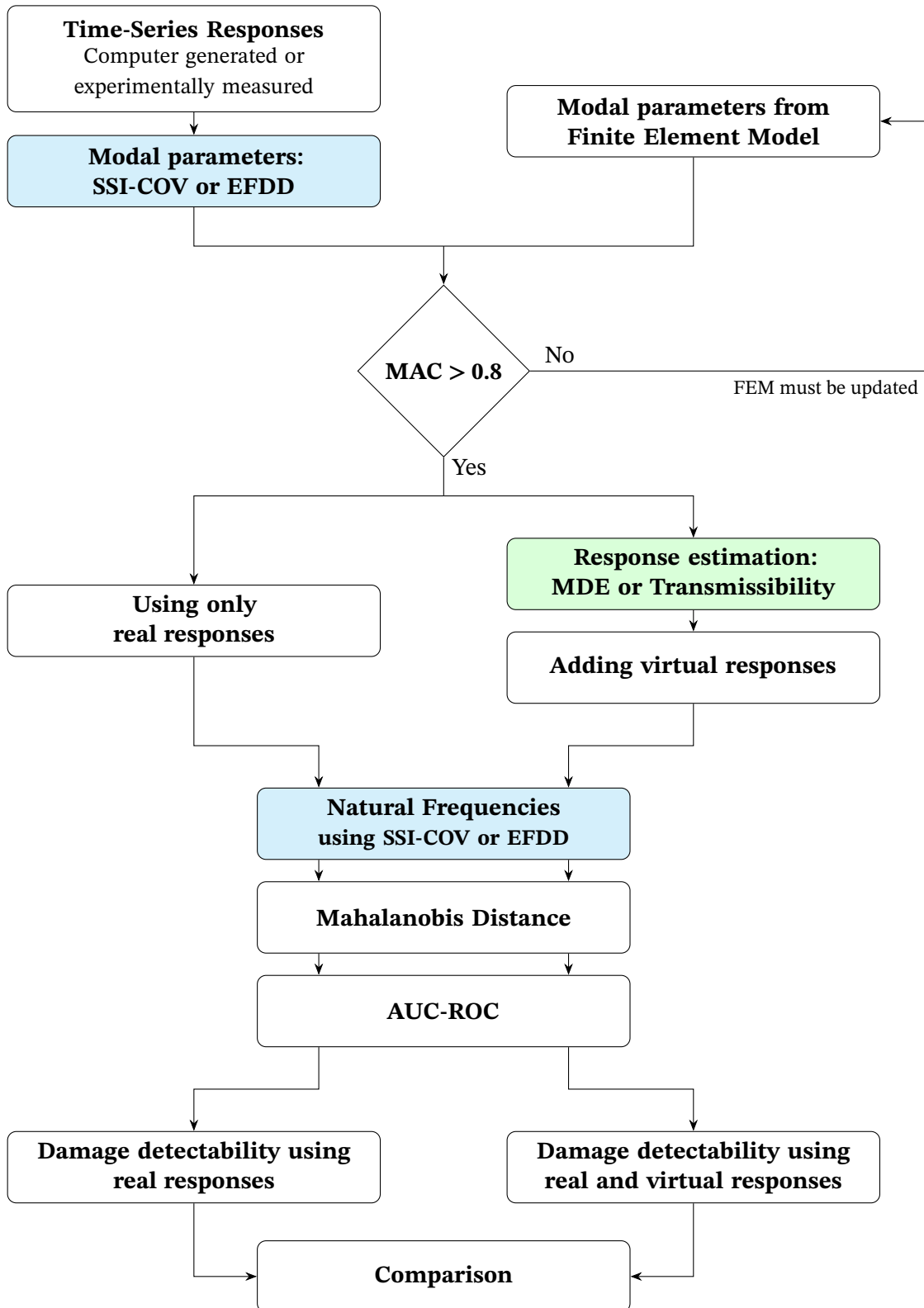
Figure 1.2. Flowchart of the methodology used in both previous and present theses.

Finally, with the experimental application, the same methodology is applied, as to verify if the findings and conclusions of the numerical study are validated. Do the methods behave the same way as they did in the numerical application? And can they be applied to measured responses acquired from wind excitation?

1.4 Thesis outline

This first Chapter provided the contextualization needed and the presented the methodology performed throughout this work. The remaining Chapters of this thesis approach the following topics:

Chapter 2 The second Chapter focuses on the theoretical and mathematical backgrounds of the two output-only modal identification methods used in this study;

Chapter 3 The third Chapter presents three response estimation methods and their respective formulations;

Chapter 4 The fourth Chapter focuses on the numerical application of the methods introduced in Chapters 2 and 3; for each method, damage detection is measured and compared using only (real) measured responses and using real and virtual responses; results are presented and discussed;

Chapter 5 The fifth Chapter focuses on the experimental application, where sensors were placed on a cantilever beam and the beam was placed outside to be excited by wind; the same methodology was applied, where responses were estimated to unmeasured locations and damage detectability measured for both methods; results are presented and discussed;

Chapter 6 The sixth and final Chapter contains the conclusions gathered from both applications, and presents future work recommendations.

2

Modal identification methods

As seen in Subsection 1.2.1, different system models can be considered when tackling the system model identification. Aside from a FEM of the structure to assure the accurate simulation results, this study uses two distinct modal identification methods, each with their own system models.

As such, this Chapter focuses on those two modal identification methods to extract the modal parameters from the structure's time responses: Covariance-driven Stochastic Subspace Identification (SSI-COV) and Enhanced Frequency Domain Decomposition (EFDD). Because these methods belong to different domains, a distinction is first given between time domain and frequency domain.

Time domain and frequency domain

It was seen in Subsection 1.1.4 that the basis of OMA techniques lies in using ambient excitation that is naturally available to measure the dynamic responses of a structure and extract its modal parameters. Also, in Subsection 1.2.1, it was seen that the referred ambient excitation can be modelled as white noise. As per Brincker and Ventura in [37], when white noise is modelled using random samples from a Gaussian distribution, all the information in the signal is concentrated in the second order properties, which are described completely by correlation functions or spectral densities, as these two form a Fourier Transform pair and therefore carry the same information. The main difference between this pair is that whereas time domain techniques use correlation functions (which display signal variation over a span of time), frequency domain techniques use spectral densities (which display signal intensity over a frequency band).

One of the earliest OMA techniques, the Natural Excitation Technique (NExT), a time domain technique developed in [38], has shown that the correlation function can be expressed as a summation of decaying sinusoids, each having a damped natural frequency, damping ratio and mode shape coefficient, identical to the ones of their corresponding structural modes [39]. In other words, with white noise excitation, the structural response can be decoupled into single degree of freedom (SDOF) systems, each of which describing the random response of one mode. This means that the correlation function can be interpreted as free decays, and via the Fourier Transform, spectral densities can be interpreted as the corresponding frequency domain functions [37].

When structures vibrate, they tend to have higher oscillatory amplitudes near their natural frequencies, and measuring these variations in intensity (or energy) is a great tool in SHM techniques – as used in the second method presented in this Chapter. Because spectral densities show the distribution of energy as a function of frequency, they can also be known as Power Spectral Density (PSD) [40, 37].

In the time domain, all the modes present in the signal are present at any time during the free decay considered, meaning the identification problem has full rank, and this is one of the disadvantages of the system identification in the time domain. Their main advantage is that they obtain bias-free data, meaning results less prone to issues of signal processing. In the frequency domain, each mode has a small frequency band where that mode dominates, making this the advantage over time domain methods: modes can be identified by decomposing the frequency range into different smaller bands; this way, modes outside the considered band have reduced influence over the results. However, their main disadvantage is that they suffer some kind of bias in the spectral density estimates [37].

2.1 Stochastic Subspace Identification

Stochastic Subspace Identification (SSI) algorithms are classified as time domain techniques, and they have been around for several decades. Introduced by Van Overschee and De Moor in [41], SSI allows the identification of a stochastic state-space model from response measurements only, as the state-space model is very general and can describe a linear vibrating structure excited by white noise [42].

2.1.1 State-space models

When studying the dynamic behaviour of a mechanical system, the equations of motion can be written in the following differential matrix form [43],

$$\mathbf{M}\ddot{\mathbf{y}}(t) + \mathbf{D}\dot{\mathbf{y}}(t) + \mathbf{K}\mathbf{y}(t) = \mathbf{f}(t) \tag{2.1}$$

where $\mathbf{M}$, $\mathbf{D}$ and $\mathbf{K}$ are the mass, damping and stiffness matrices, $\mathbf{f}(t)$ is the excitation force (or load vector), and $\mathbf{y}(t)$ is the displacement vector in continuous time t, where a dot over a time function denotes its derivative with respect to time [44]. In the context of civil and mechanical engineering structures, these equations are obtained as the finite element approximation of the system with a limited number of DOFs [30], as stated in Subsection 1.2.1.

Even though Equation 2.1 can accurately represent the structure's dynamic response in continuous time, it is not directly useful in an experimental modelling context. Firstly, because generally in Modal Analysis, the response measurements are sampled at discrete time instants. Secondly, it is not possible to measure all DOFs of the FEM. Lastly, there may be other unknown excitation sources apart from $\mathbf{f}(t)$, and noise related to the measurements themselves are always present, so it is necessary to perform noise modelling [30]. Therefore, in defining the state vector $\mathbf{u}(t)$ as a function of the displacement vector $\mathbf{y}(t)$,

$$\mathbf{u}(t) = \begin{Bmatrix} \mathbf{y}(t) \\ \dot{\mathbf{y}}(t) \end{Bmatrix} \tag{2.2}$$

the second order system equation given by Equation 2.1 is simplified into a set of first order equations, which describe the state-space system model [45],

$$\begin{aligned} \dot{\mathbf{u}}(t) &= \mathbf{A}\mathbf{u}(t) + \mathbf{B}\mathbf{f}(t) \\ \mathbf{y}(t) &= \mathbf{C}\mathbf{u}(t) \end{aligned} \tag{2.3}$$

in which $\mathbf{A}$ is the system matrix, in continuous time, that completely characterises the dynamics of the system by its eigenvalues (natural frequencies), $\mathbf{B}$ is the load (or input) matrix and $\mathbf{C}$ is the output matrix that specifies how the internal states are transformed to the outside world [46]. This way, the first two matrices define the properties of the system and the last one is determined by the particular selection of output variables. Matrices $\mathbf{A}$ and $\mathbf{B}$ can also be written as functions of the system's property matrices (from Equation 2.1),

$$\mathbf{A} = \begin{bmatrix} 0 & \mathbf{I} \\ -\mathbf{M}^{-1}\mathbf{K} & -\mathbf{M}^{-1}\mathbf{D} \end{bmatrix}; \quad \mathbf{B} = \begin{bmatrix} 0 \\ \mathbf{M}^{-1} \end{bmatrix} \tag{2.4}$$

15

2.1.2 Covariance-driven Stochastic Subspace Identification

From this formulation, the SSI algorithm applied is the Covariance-driven Stochastic Subspace Identification (SSI-COV). It assumes the stochastic and discrete state-space model just described and uses the discrete time responses sampled to compute the output covariance matrix, also known as the cross-correlation matrix.

Sampling the outputs at k time lags Δt gives $\mathbf{y}_k = \mathbf{y}(k\Delta t)$ vectors, which can be represented as the system response, in discrete time, by the data matrix $\mathbf{Y}$ [45]:

$$\mathbf{Y} = \begin{bmatrix} \mathbf{y}_1 \\ \mathbf{y}_2 \\ \vdots \\ \mathbf{y}_N \end{bmatrix} \tag{2.5}$$

with dimensions $N \times l$ (with N sensors and $\mathbf{y}$ vector length l) from which the discrete covariance matrix $\mathbf{R}_i$ at time lag i can be estimated as [47]:

$$\mathbf{R}_i = \mathrm{E}\left[\mathbf{y}_{k+i} \cdot \mathbf{y}_k^T\right] \tag{2.6}$$

in which E denotes mathematical expectation. The output covariances can be gathered in a Block Hankel matrix $\mathbf{H}_i$ with $2i$ block rows, or in a square Block Toeplitz matrix $\mathbf{T}_i$ with dimensions $li \times li$,

$$\mathbf{T}_i = \begin{bmatrix} \mathbf{R}_i & \mathbf{R}_{i-1} & \cdots & \mathbf{R}_1 \\ \mathbf{R}_{i+1} & \mathbf{R}_i & \cdots & \mathbf{R}_2 \\ \cdots & \cdots & \ddots & \vdots \\ \mathbf{R}_{2i-1} & \mathbf{R}_{2i-2} & \cdots & \mathbf{R}_i \end{bmatrix} \tag{2.7}$$

where the value of i is usually determined so that $li > n$ in which n is the model order.

According to the property of the stochastic state-space model, the Toeplitz matrix can be decomposed into the product of the observability matrix and the controllability matrix. Then, by performing Single Value Decomposition (SVD) of the Toeplitz matrix and equalling those two equations, allows to solve for the estimated system matrices $\mathbf{A}$ and $\mathbf{C}$ in discrete time, respectively $\mathbf{A}_d$ and $\mathbf{C}_d$ [48].

Matrices $\mathbf{A}$ and $\mathbf{B}$ can be related, both in continuous and in discrete time, and performing eigenvalue decomposition of matrix $\mathbf{A}_d$ gives, for the P eigenvalues considered,

$$\mathbf{A}_d = \mathbf{\Psi}\mathbf{\Lambda}\mathbf{\Psi}^{-1} = \sum_{r=1}^{P} \boldsymbol{\psi}_r \lambda_r \boldsymbol{\psi}_r \tag{2.8}$$

where $\mathbf{\Lambda}$ is a diagonal matrix containing the discrete time eigenvalues (or poles) λ_r and $\mathbf{\Psi}$ is the mode shape matrix containing the discrete time eigenvectors (or mode shapes) $\boldsymbol{\psi}_r$. Continuous time poles λ_{cr} are obtained from the discrete time poles λ_r as:

$$\lambda_{cr} = \frac{\ln(\lambda_r)}{\Delta t} \tag{2.9}$$

where natural frequencies and damping ratios are respectively given by

$$f_{cr} = \frac{|\lambda_{cr}|}{2\pi}; \quad \zeta_{cr} = \frac{-100\,\mathrm{Re}(\lambda_{cr})}{|\lambda_{cr}|} \tag{2.10}$$

Finally, continuous time mode shapes are given by

$$\boldsymbol{\phi}_{cr} = \mathbf{C}\boldsymbol{\psi}_r \tag{2.11}$$

2.1.3 Relevant parameters in SSI-COV

Like other OMA techniques, SSI-COV is heavily dependant on the chosen parameters. For this method, the most important parameters are, as mentioned above, the model order n and the number of blockrows $2i$, and the stabilisation level.

The model order directly affects the eigenvalues and eigenvectors obtained, and should theoretically equal the number of non-zero singular values of the Toeplitz matrix, but since singular values converge to zero due to the influence of noise, it becomes difficult to determine the model order when only observing those singular values [47]. To help the selection of n, stabilization diagram are used, as they separate physical eigenvalues from spurious ones by estimating the model parameters for a range of orders [49].

Several criterion can be set for the analysis of this stabilization diagram, where a pole is considered stable if criteria is met. Usually, maximum deviance of natural frequencies, damping ratios and mode shapes are the criteria used (where the mode shape deviance is commonly checked with the respective MAC value).

The stabilization level is also related to the number of blockrows, as a low stabilization level combined with a high number of blockrows results in a very cluttered stabilization diagram, which in turn adds difficulty to the separation of physical from spurious modes. As

17

for the number of blockrows $2i$, it should be large enough that the time lags represented in the covariance matrix (Equation 2.6) have enough length to provide sufficient resolution to identify the lowest frequencies of interest. If $2i$ is too low, the frequency resolution won't be low enough. If $2i$ is too high, the number of spurious modes will increase, so adequate selection of parameters is essential in this method [49].

Given this difficulty in setting adequate parameters, another method will be studied and compared to SSI-COV, both in terms of use (as in, setting parameters) and results.

2.2 Enhanced Frequency Domain Decomposition

As a method in frequency domain, Enhanced Frequency Domain Decomposition (EFDD) is known for its user-friendliness and fast computer processing speed. In the first topic of Chapter 2, the main differences between time domain and frequency domain, and the significance of white noise excitation in OMA techniques in more mathematical terms have been reviewed. This Chapter focuses on the EFDD method, namely its history, developments and relevant parameters.

2.2.1 From the basic Peak-Peaking technique, to EFDD

Even though output-only methods have been deeply researched in recent times, as Peeters states in [25], "the problem of obtaining modal parameters from output-only data is basically solved since a few decades: this basic solution consists of selecting the peaks of the spectra of the output signals", which is also referred to as the Basic Frequency Domain (BFD), or the Peak-Picking (PP) technique.

As the name suggests, the Enhanced Frequency Domain Technique is a development of a simpler method, the Frequency Domain Decomposition (FDD), which, in turn, is presented as an extension of the PP technique. The basis of the latter is that the system's natural frequencies can be identified from the peaks in the power spectral densities (PSD) computed from the time-series responses measured using simple signal processing, as introduced by Bendat and Piersol in [50].

However, this simple method does not come without its issues: for closely spaced modes, their detection becomes difficult and the results become heavily biased; also, the frequency estimates are limited by the frequency resolution of the spectral density estimates; lastly, damping estimation is uncertain or impossible. As such, the FDD technique is then developed

by Brincker et al. in [51] to overcome the shortcomings of the PP technique.

For that, FDD uses SVD of the PSD matrix, allowing the detection of close modes and mode multiplicity. From the SVD matrix, singular values are sorted according to the singular vectors and for each peak identified, the first singular vector was chosen as the mode shape estimate. The corresponding singular values, where MAC values are highest between the singular vectors and the mode shape estimates, is the estimated natural frequency. This method allows for accurate estimations of natural frequencies and mode shapes. However, there are limitations to this method, as it cannot estimate damping ratios [51, 52].

Then, to overcome this limitation, FDD was further developed into EFDD (also known as a second generation of FDD) by Brincker et al. in [53], where damping ratios are now estimated, along with more accurate estimations of natural frequencies and mode shapes.

As first presented by Bendat and Piersol in [54], the PSD expresses the relationship between unknown inputs and measured outputs, as functions of frequency ω,

$$\mathbf{G}_{yy}(\omega) = \overline{\mathbf{H}}(\omega) \cdot \mathbf{G}_{xx}(\omega) \cdot \mathbf{H}(\omega)^T \tag{2.12}$$

where $\mathbf{G}_{xx}$ and $\mathbf{G}_{yy}$ are the input and output PSD matrices, and $\mathbf{H}$ is the Frequency Response Function (FRF) matrix, where the overline and the superscript T denote complex conjugate and transpose, respectively.

In this method, SVD of the PSD matrix is also used, and from the SVD matrix, singular vectors are estimates of the mode shapes, and the corresponding singular values are the auto-spectral density functions of the corresponding SDOF systems. Performing SVD of the output PSD matrix at discrete frequencies $\omega = \omega_i$ [53] gives:

$$\hat{\mathbf{G}}_{yy}(\omega_i) = \mathbf{U}_i \cdot \mathbf{S}_i \cdot \mathbf{U}_i^H \tag{2.13}$$

where $\mathbf{U}_i = [u_{i1}, u_{i2}, ..., u_{im}]$ is a unitary matrix of single vectors u_{ij}, $\mathbf{S}_i$ is a diagonal matrix of scalar singular values s_{ij}, and the superscript H denotes complex conjugate transpose (or Hermitian). Near a peak where only one mode is dominating, the mode shape estimate for that peak $\hat{\phi}_p$ is the respective first singular vector:

$$\hat{\phi}_p = u_{p1} \tag{2.14}$$

For singular vectors with the highest MAC values between the mode shape estimates at the peaks, the corresponding truncated singular values near the peaks are taken back to time

domain using the Inverse Fourier Fast Transform (IFFT). In the time domain, spectral densities become correlation functions that can be interpreted as free decays. So, for each free decay, the logarithmic decrement δ can be determined with:

$$\delta = \frac{2}{m} \ln\left(\frac{r_0}{|r_m|}\right) \tag{2.15}$$

in which r_0 is the initial value of the correlation function, m extremes are considered and r_m is the function value at that extreme.

Finally, the damping ratios are given by:

$$\zeta = \frac{\delta}{\sqrt{\delta^2 + 4\pi^2}} \tag{2.16}$$

and using both the linear regressions of the crossing times and the damped natural frequencies f_d, the undamped natural frequencies f_n are defined as:

$$f_n = \frac{f_d}{\sqrt{1 - \zeta^2}} \tag{2.17}$$

FDD techniques are known for their user-friendliness, and when compared to other time domain methods, they are faster and simpler to use, since it is not highly demanding from a computational point of view [55].

2.2.2 Implementation of EFDD in python

For the purposes of this study, FEM analysis can be performed through several programs and programming languages. The best suited software for the study at hands is python, which is developed under an open-source license, making it freely usable and distributed. Many researchers make use of this open-source tool to develop their studies, programming efficient new methods to solve many different problems, and making complex models and algorithms available to students, other researchers or any other person with access to a computer.

As such, the EFDD method was implemented in python using an open-source package developed in the original software publication by Carini and Rocha in [56]. This package contains two modules: `MRPy` for pre-processing with auxiliary functions and `CESSIPy` with the main functions needed.

The `EFDD` function from this last module allows for both interactive and batch mode identifications, and because the goal of the present study is to analyse the dynamic responses of the

structure over a long period of time, extracting the modal parameters for each daily observation, continuous user interaction is not favourable. Nevertheless, user interaction is necessary when first learning how to use this package, as it allows for a better understanding of all the steps necessary in the modal parameter identification, as well as the definition of adequate parameters.

2.2.3   Relevant parameters in EFDD

Like the SSI-COV method, several parameters have to be defined when applying the EFDD method. Following the procedural description of this method in Subsection 2.2.1, the parameters that need to be defined are as follows:

- The indexes of the peaks in the PSD;
- The indexes of the singular values chosen for the fittings – for simplicity, all the first singular values were selected;
- The frequency intervals used in the curve fittings;
- The time intervals for the auto-correlation functions (free decays).

Given that slight changes to these parameters greatly alter the results obtained, and that this package does not allow for automated modal identification, the definition of this set of parameters was found to be somewhat difficult. These parameters were then tested by trial and error, as no better way of defining them has been found so far.

The model used in this study is a cantilever beam which was excited with white noise using random samples from a Gaussian distribution, with set values for mean and standard deviation. Also, given the meteorological conditions in which wind turbines operate all year round, daily temperature variations were also considered, which are translated into daily variations of the Elasticity modulus. So, because the time-responses are different for each observation, and because damage is applied to the structure in increasing values, it is expected that modal parameters change throughout this study, as seen in Subsection 1.1.3.

As such, a semi-automated process of the modal identification was obtained via some integral python functions, where, for each observation, new parameters are set. First, all the PSD peaks were searched and sorted, and since this study focuses on the first four natural frequencies, the four highest peaks (within the expected values) were selected from the sorted values. The frequency intervals were then defined based on the values of those four peaks found.

The exceptions to this semi-automated process were the time intervals for the auto-correlation

functions. Because of the slight variations observed in the natural frequencies in the presence of damage, no relevant changes were seen in the free decays. Even still, several intervals were tested in order to assess which set of parameters gave the best and most consistent results.

2.2.4 Modal identification process with EFDD

Having mentioned the parameters needed in this package, this Subsection details all the steps necessary to perform the modal identification, as well as specify the inputs, outputs and functions used from the available modules. Using the time-series responses from a random chosen day as an example, a figure is obtained for each function used, as seen below.

Two inputs are required to initiate the process: the time responses for the chosen observation and the sampling frequency. As per the Nyquist theorem, the sampling frequency should be at least twice the maximum frequency present in the signal [40] – in this case, the sampling frequency is the first power of two value above the doubled fourth natural frequency, 512 Hz. The first step is to obtain the accelerations from the time responses (displacements) using two successive differentiate functions, `MRPy.differentiate(·)`.

Then, the length of each time segment and the frequency resolution are defined as powers of two 2^n, given the nature of the Analog signal (discrete time-series). With the accelerations, the time segment length and the frequency resolution, the PSD is computed using the `SDM` function. In this case, the Cross Power Spectral Density matrix is obtained, which compares each signal with all the signals considered. Because this study looks to obtain the first four modal parameters, four time responses are generated for each observation. In Figure 2.1, the Cross PSD matrix components are plotted in amplitude and phase against frequency. Noting that this matrix is squared and symmetric, the diagonal components have null phases as these components are in phase with themselves.

The next step is to obtain the Averaged Normalized Power Spectral Density (ANPSD), to allow for better identification of the peaks, with the `ANPSD_from_SDM` function; see Figure 2.2.

The final step is then to obtain the estimations of the natural frequencies, mode shapes and damping ratios with the `EFDD` function. After selecting the peaks from the ANPSD function, MAC values are obtained for the frequency intervals established in the singular values selected, as presented in Figure 2.3, where all MAC values are above 0.9. The normalized auto-correlation functions for each free decay are presented in Figure 2.4, with the specified time intervals, where natural frequencies and damping ratios estimations are presented. For each observation, the modal parameters are saved to python files to be accessed later on.
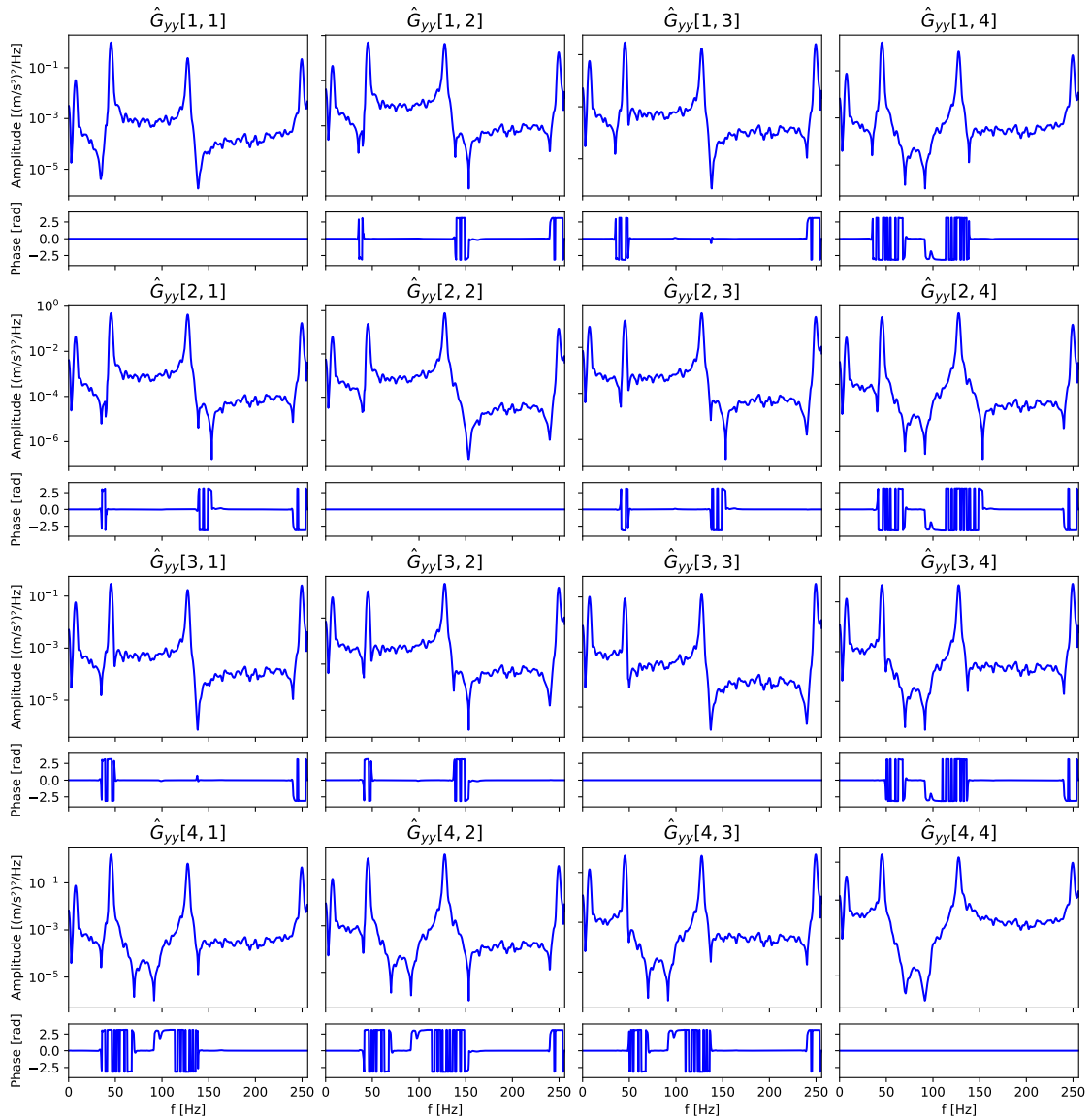
Figure 2.1. Cross Power Spectral Density matrix plot of amplitude and phase over frequency, for each matricial component of the practical example chosen.
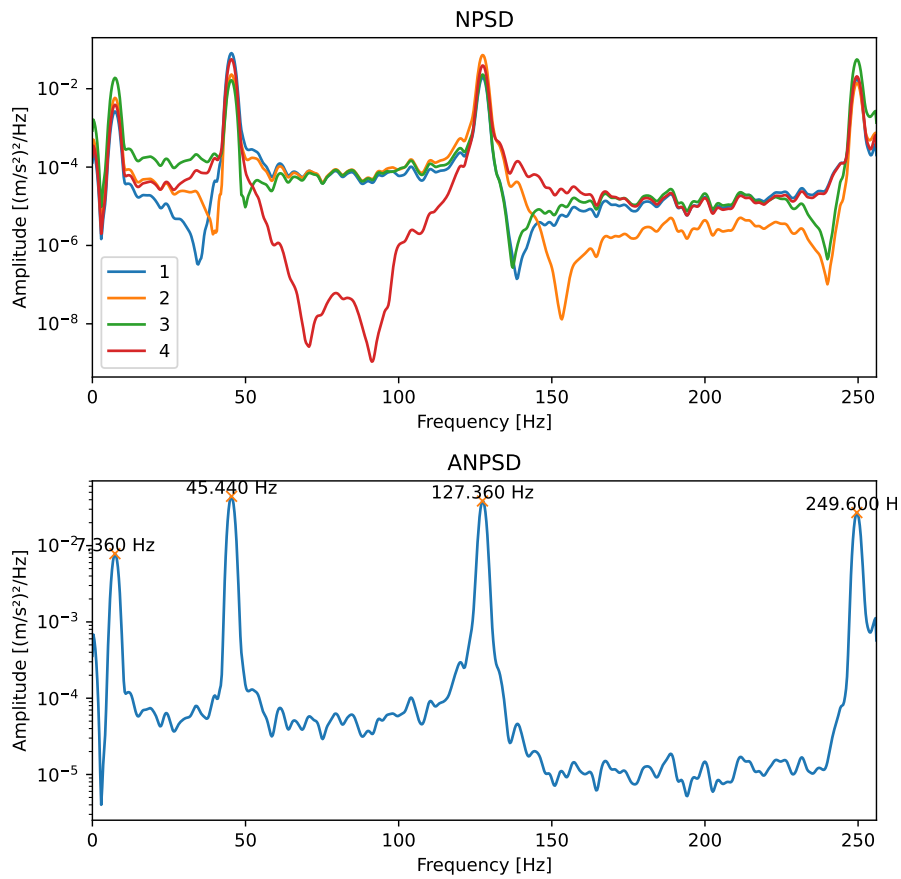
Figure 2.2. Normalized Power Spectral Density and Averaged Normalized PSD of the practical example chosen, with the selection of the four peaks of interest to this study.
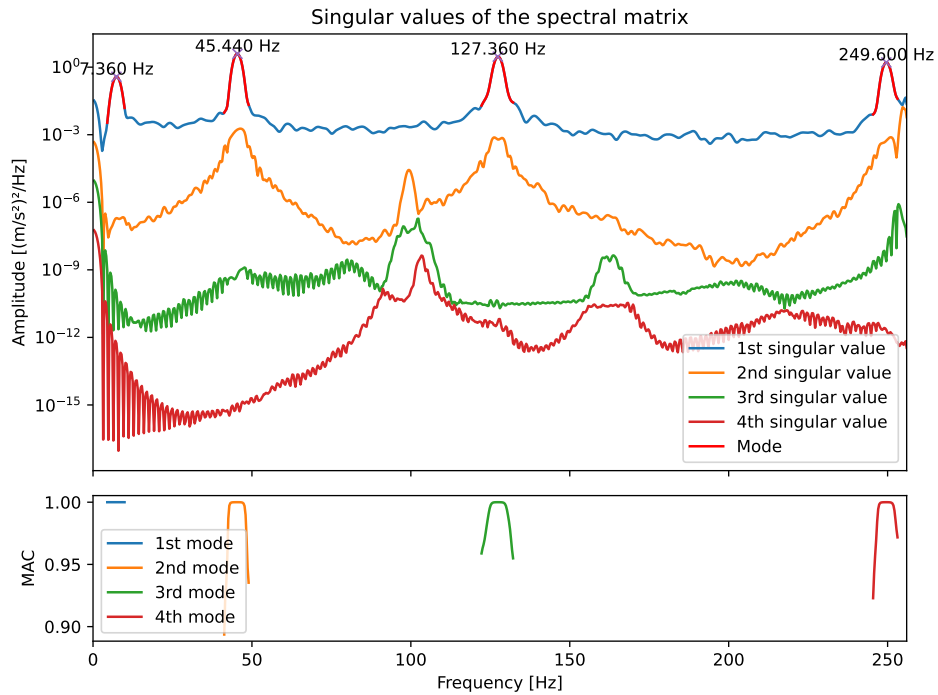
Figure 2.3. Singular values, frequency intervals and MAC values for each peak (and respective interval) of the practical example chosen.
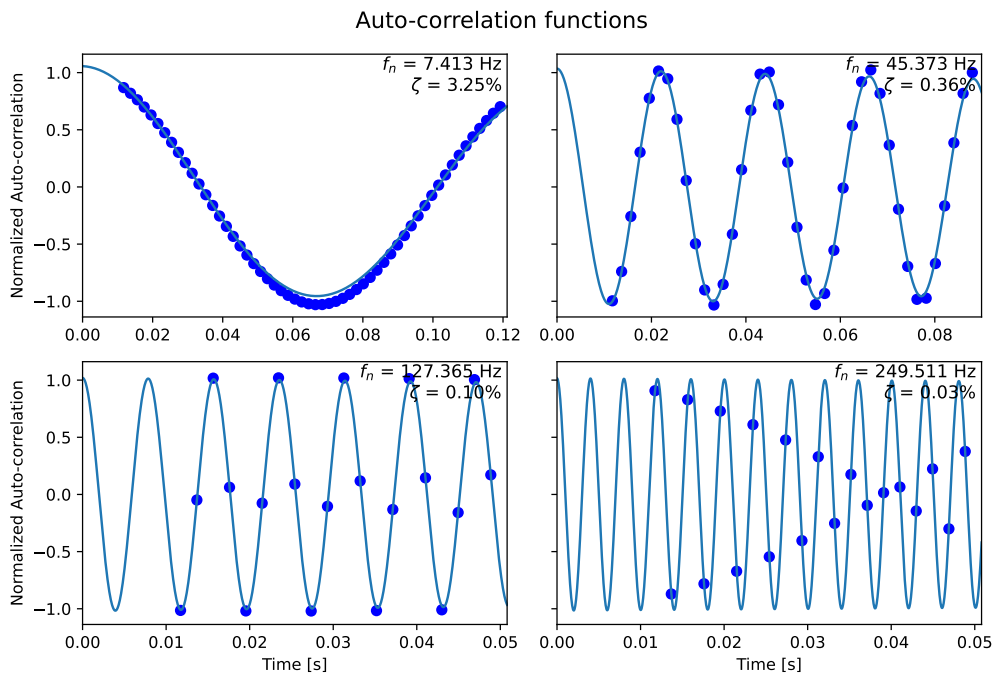
Figure 2.4. Normalized auto-correlation functions for each free decay of the practical example chosen, with the respective estimations of natural frequencies and damping ratios.

25

$$3$$

Response estimation methods

As seen in Subsection 1.1.5, response estimation based on reduction or expansion methods use measured information and a FEM of the structure, accurately representing the system in study, to predict responses in locations where no physical (real) sensors are placed. In general terms, with p measurements taken from the real sensors on the experimental model and using an updated FEM with N DOFs, responses from different DOFs can be related, and so, responses can be predicted for all N DOFs of the FEM, whether they were measured (from real sensors) or not (to virtual locations).

This Chapter focuses on the methods used in this study: System Equivalent Reduction Expansion Process (SEREP), Modal Decomposition and Expansion (MDE) and Transmissibility.

3.1 System Equivalent Reduction Expansion Process

As introduced by O'Callahan et al. in [57], this method is suitable for both model reduction and modal data expansion, with the same level of accuracy. In order to obtain the numerical model, it requires the solution of the generalized eigenproblem, defined by the natural frequencies and mode shapes. Taking the mode shapes from the numerical model $\mathbf{\Phi}_{FEM}$ (which are partitioned into a set of primary DOFs and a set of secondary DOFs) and performing the Moore-Penrose pseudo-inverse of the primary DOFs only $\mathbf{\Phi}_{FEM,p}$ results in the transformation matrix $\mathbf{T}$ [58]:

$$\mathbf{T} = \mathbf{\Phi}_{FEM} \cdot \mathbf{\Phi}_{FEM,p}^{+} \tag{3.1}$$

where the superscript + represents the aforementioned Moore-Penrose pseudo-inverse, and primary DOFs can be seen as active DOFs from which measurements are takes. SEREP can only be applied if the number of primary DOFs is greater than or equal to the number of

available mode shapes, but since it uses the full numerical model, it preserves the natural frequencies and mode shapes used to form $\mathbf{T}$.

Therefore, from a set of experimental responses $\mathbf{Y}_p^e$ acquired by a limited number of sensors (at active DOFs, from Equation 2.5) and using the transformation matrix defined above, the full set of estimated responses $\hat{\mathbf{Y}}_{full}$ is given by:

$$\hat{\mathbf{Y}}_{full} = \mathbf{T} \cdot \mathbf{Y}_p^e \tag{3.2}$$

To minimize the chance of overfitting, the Moore-Penrose pseudo-inverse should be preferably squared (with the same number of primary DOFs and mode shapes) given that this way, the pseudo-inverse becomes the general inverse. As such, MDE is used as an alternative, as it allows, for a set number of primary DOFs, the expansion of the same number of responses to virtual locations [59].

3.2   Modal Decomposition and Expansion

The Modal Decomposition and Expansion (MDE) consists of two steps in estimating responses: modal decomposition of the measured outputs, and subsequent modal expansion to obtain the outputs estimations at unmeasured (virtual) locations [60].

The modal decomposition approach [61] states that the displacement vector $\mathbf{y}(t)$ can be written as a combination of the mode shape vectors [62, 63]:

$$\mathbf{y}(t) = \mathbf{\Phi} \cdot \mathbf{q}(t) \tag{3.3}$$

where $\mathbf{\Phi}$ is the mode shape matrix (containing said vectors) and $\mathbf{q}(t)$ is the vector of the modal coordinates for each time instant t. For the sake of simplicity, time notation is omitted from this point forward.

Having guaranteed that the FEM is accurately representing the structure and that there is a high correlation between FEM and measured mode shapes through MAC, both the FEM mode shape matrix $\mathbf{\Phi}_{FEM}$ and the experimentally measured mode shape matrix $\mathbf{\Phi}_{EXP}$ can be used to estimate responses at any DOF of the structure. However, since only a limited number of DOFs are measured experimentally, the FEM mode shape matrix describes the full behaviour and the experimental mode shape matrix describes the behaviour at only the measured primary DOFs.

For a set of measured responses at primary DOFs $\mathbf{Y}_p^e$, containing each displacement vector $\mathbf{y}$, and using the mode shape matrix becomes $\mathbf{\Phi}_{EXP}$ containing only the respective measured DOFs, the modal coordinate vector $\mathbf{q}$ is then given by:

$$\mathbf{q} = \mathbf{\Phi}_{EXP}^+ \cdot \mathbf{Y}_p^e \tag{3.4}$$

Similarly, when considering the full set of responses $\mathbf{Y}_{full}$,

$$\mathbf{Y}_{full} = \mathbf{\Phi}_{FEM} \cdot \mathbf{q} \tag{3.5}$$

meaning the transmissibility matrix can be defined as:

$$\mathbf{T} = \mathbf{\Phi}_{FEM} \cdot \mathbf{\Phi}_{EXP}^+ \tag{3.6}$$

Finally, the full set of estimated responses $\hat{\mathbf{Y}}_{full}$, composed of the estimated displacement vectors $\hat{\mathbf{y}}$, can be obtained through Equation 3.2.

Like the two previous methods, the Transmissibility method also needs the time responses, and could need the mode shapes (measured and/or from the model) to estimate responses at unmeasured locations (as will be seen ahead, this method needs the Frequency Response Functions (FRF), which can be obtained using the mode shapes (like SEREP and MDE), or the modal matrices from the model). This method is detailed in the next Section, as one of the goals of this study is the comparison between MDE and Transmissibility.

3.3 Transmissibility

By definition, transmissibility in a SDOF system is the ratio between the amplitude of the response displacement and the amplitude of the displacement imposed at the foundation [43]. After successful efforts in generalizing both displacement and force transmissibility to multi degree of freedom (MDOF) systems, new applications of these concepts gain interest. Specific to the case at hands, when only a limited number of measurements are possible, and if knowing the transmissibility matrix of a system, then it would be possible to estimate responses at unmeasured (virtual) locations [64, 65].

First presented by Ribeiro et al. in [66], the general approach considers three sets of coordinates: *A* where forces are applied (both unknown and unmeasured, as this case considers ambient excitation (see Subsection 1.2.1)), *K* where responses are known (and measured) and

U where responses are unknown (and estimated). Figure 3.1 represents a schematic illustration of an arbitrary set of coordinates, along with forces applied $\mathbf{F}_A$ and responses, both known $\mathbf{Y}_K$ and unknown $\mathbf{Y}_U$.
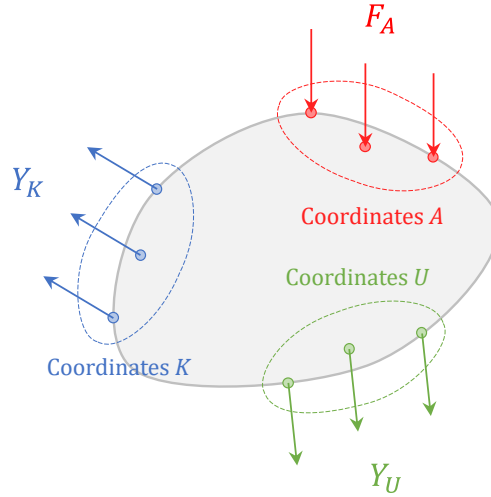
Figure 3.1. Arbitrary sets of coordinates: A and respective forces applied $\mathbf{F}_A$, known K and respective known responses $\mathbf{Y}_K$, and unknown U and respective unknown responses $\mathbf{Y}_U$.

In the frequency domain, relating the forces applied $\mathbf{F}_A$ to both the known responses $\mathbf{Y}_K$ and the unknown responses $\mathbf{Y}_U$ gives:

$$\mathbf{Y}_K = \mathbf{H}_{KA} \cdot \mathbf{F}_A \tag{3.7}$$

$$\mathbf{Y}_U = \mathbf{H}_{UA} \cdot \mathbf{F}_A \tag{3.8}$$

where $\mathbf{H}_{KA}$ and $\mathbf{H}_{UA}$ are the receptance matrices (or FRFs) between coordinates K and A, and U and A, respectively. The expression that defines the unknown responses $\mathbf{Y}_U$ is obtained in solving Equation 3.7 and 3.8:

$$\mathbf{Y}_U = \mathbf{H}_{UA} \cdot \mathbf{H}_{KA}^+ \cdot \mathbf{Y}_K \tag{3.9}$$

from which the transmissibility matrix is defined as:

$$\mathbf{T}_{UK} = \mathbf{H}_{UA} \cdot \mathbf{H}_{KA}^+ \tag{3.10}$$

Like SEREP, the number of measured DOFs K must be greater than or equal to the number of excited coordinates A. Now the goal is to define the transmissibility matrix is order to

estimate the responses to unknown and unmeasured locations, using the measured ones. A way of obtaining the receptance matrices needed is through the modal properties of the system. Considering a number of K modal properties obtained from the same number of known responses $\mathbf{Y}_K$, $\mathbf{H}_{KA}$ becomes a square matrix $\mathbf{H}_{KK}$ regardless of the number of excited DOFs A.

The equations of motion describing the dynamic behaviour of a mechanical system were presented Equation 2.1 in matricial form and in the time domain t, but they can also be written in the frequency domain ω, assuming harmonic excitation, with [43]:

$$[-\omega^2 \mathbf{M} + j\omega \mathbf{D} + \mathbf{K}] \cdot \mathbf{Y}(\omega) = \mathbf{F}(\omega) \tag{3.11}$$

where $j = \sqrt{-1}$. Given that the receptance matrix $\mathbf{H}$ relates the responses with the applied forces, it can be defined in the frequency domain as a function of the property matrices $\mathbf{M}$, $\mathbf{D}$ and $\mathbf{K}$ with,

$$\mathbf{H}(\omega) = [-\omega^2 \mathbf{M} + j\omega \mathbf{D} + \mathbf{K}]^{-1} \tag{3.12}$$

For N mass-normalized mode shapes $\phi_1, \phi_2, ..., \phi_N$, Equation 3.12 becomes,

$$\mathbf{H}(\omega) = \sum_{k=1}^{N} \frac{\phi_k \phi_k^T}{-\omega^2 + 2j\zeta_k \omega_k \omega + \omega_k^2} \tag{3.13}$$

which, at natural frequencies $\omega = \omega_i$, gives:

$$|\mathbf{H}(\omega_i)| = \frac{|\phi_i \phi_i^T|}{2\zeta_i \omega_i^2} \tag{3.14}$$

Even though the present thesis does not focus on force transmissibility, this method proves capable of even obtaining the force transmissibility without actually measuring forces, requiring only the measurements of displacements, given the relation between displacement and force transmissibilities [67].

4

Numerical application

With the goal of comparing the results obtained between the two modal identification methods and the two response estimation methods, this thesis bases its work and further develops that of a previous thesis developed in the same research group, studying damage detection through the use of virtual sensing – [68]. That work focused on performing modal identification with SSI-COV and response estimation with MDE. The present work aims to numerically apply two new methods and later, experimentally obtain responses to validate the results and conclusions obtained in the numerical part.

As such, this Chapter focuses on the first part of the work developed on the present thesis, which is the numerical application of two new methods – EFDD for modal identification and Transmissibility for response estimation. For that, the next Sections focus on reviewing the most relevant studies performed and the main conclusions obtained in the previous work, presenting the current numerical application and lastly, discussing and comparing the results obtained.

4.1   Studies performed and results obtained in previous works

Even though the wind turbine blades are complex structures made of composite materials, this study uses a simpler structure to model the real one: a cantilever beam with rectangular cross-section, in which one end is referred to as the fixed edge and the other as the free edge. Therefore, the Euler-Bernoulli beam finite element is used for the FEM analysis, in which the DOFs per node are nodal displacement and rotation [69].

The next step is to determine the mesh size, having in mind the fact that a more discretized mesh can more accurately describe the system, but discretizing the mesh too much will severely increase computational effort and processing times. Thus, a convergence study was performed

to determine the most adequate mesh size for the beam in study, in which was found that a minimum of 20 finite elements must be present in the mesh. Therefore, the mesh size chosen is that of 40 finite elements, as this number provides sufficient discretization without the noticeable increase of the processing time.

As mentioned in Subsection 2.2.3, the numerical model is excited with white noise (as to model the ambient excitation of the real structure) and daily temperature variations are applied through the daily variations of the Elasticity modulus. Also, some healthy (undamaged) observations are measured before damage is introduced in increasing (percentual) values.

Several test were performed in the previous study, using different real sensor locations, different damage locations, different virtual sensor locations and different virtual sensor combinations, all of which were compared to their respective healthy reference baselines. The modal parameters extracted throughout were the first four natural frequencies and four mode shapes.

The previous study found that higher damage equates to higher MD values, even though many observations didn't exceed the established threshold. So, in aiding and measuring damage detectability, ROC curves and their respective AUC values were obtained, where it was also found that higher damage equates to higher AUCs.

Overall, it was observed that adding virtual responses increased the damage detectability over using only real responses.

Of all the real and virtual sensor placement combinations studied, the most prominent scenario – the one in which AUC values were overall highest, representing high damage detectability –, is where real sensors are placed near the free edge of the beam, and both damage occurs and virtual sensors are placed near the fixed edge. This scenario will then be the focus of this work, presented in the Sections ahead, where comparisons between the new methods are presented.

Improving code efficiency

The first task that this study required was an in dept code analysis to allow for familiarization with all the steps taken, code-wise. The numerical application of this study envolves many steps, many concepts and many calculations at the various steps taken, and as such, the code supporting this work is extent and this familiarization with the existing code (developed in [68]) provided the necessary understanding and knowledge to make the code more efficient.

In terms of space, all the outputs from the several analysis (time responses, modal parameter identification, MAC values, MD and AUC values) are stored in dictionaries so that all information regarding one scenario can be stored together in a single array, saving data and space.

The dictionaries are then saved in NPY files, a python binary file type that compacts data, reduces size in over 50% when compared to TXT files, and has very fast reading speed when compared to CSV files.

Most of the remaining code was restructured so as to run solely through functions, as many task envolve being constantly repeated (for each observation and for each scenario considered). Inside those functions, code was synthesized using global and local variables, loops and python internal functions, resulting in smaller sized code files, more compact code inside each file, easier to use and most importantly, more efficient and computationally fast.

4.2 Considerations in the numerical application

Having mentioned the analyses made in the previous study, as well as the programming work that has been performed, the current study focuses on generating time responses, so that modal parameters can be identified, virtual responses can be estimated and damage detectability can be measured and compared between the methods used.

This next Subsection details the properties and characteristics of the beam used, the mode shape slopes and the importance of sensor placement in relation to those slopes, as well as the FEM natural frequencies which the modal frequencies identified from the time responses should be close to, and the damage values applied.

4.2.1 Beam properties and characteristics

Because the second stage of this study is an experimental application, the characteristics of the beam for which simulated results were obtained were changed to match that of the experimental beam used. As such, the properties and dimensions of the new beam are indicated in Table 4.1.

The model simulating the structure and the one from which the model updating verification is established, is an undamped FEM with 40 elements. The time-series responses are obtained from the state-space model described in Subsection 2.1.1, where the model is a

Table 4.1. Dimensions and properties of the experimental beam.

Length	0.82 m
Thickness	6 mm
Width	35 mm
Elasticity Modulus	200 GPa
Density	7870 kg m^{-3}
Melting Temperature point	1370 °C

damped structure with 40 finite elements, subjected to a proportional damping constant of $\alpha = 10^{-6}$, considering damping as only proportional to the stiffness matrix, $\mathbf{D} = \alpha\mathbf{K}$.

The white noise excitation is applied as a force using a python internal function that generates random samples from a Gaussian distribution with a mean and standard deviation of 0.01 N. From this excitation, the (input) state vector of the state-space model (see Equation 2.2) is obtained, and is only applied to the DOFs corresponding to displacements, meaning the finite element nodes are subjected to forces and no moments.

That being said, this study uses four time responses to obtain the first four natural frequencies and first four mode shapes of each daily observation. For the response estimation to virtual sensors, up to four virtual sensors are used as well. From the undamped FEM, the first four natural frequencies f_n can be determined in python and they are as follows:

$$f_n = \begin{Bmatrix} 7.267 \\ 45.54 \\ 127.51 \\ 249.87 \end{Bmatrix} \text{Hz} \tag{4.1}$$

Structural mode shapes describe the way in which a structure vibrates (or deforms) when excited by the corresponding natural frequency; likewise, each mode shape has a corresponding number of nodes (points with null displacements). Analysing the slopes of the first four mode shapes is important in identifying which locations should be avoided when placing sensors (real and virtual) on the structure to measure the time responses, because sensors measure the displacements of each finite element node. In Figure 4.1, the slopes of the first four mode shapes are represented in normalized displacements and by finite element node.

From the slopes and each mode shape node, the closest finite elements nodes can be identified, as presented in Table 4.2. Because the structure modelled is a cantilever beam, this beam is divided into 40 equally spaced elements as to represent the 40 finite elements (meaning there are 41 FE nodes, as seen in Figure 4.1). Considering the fixed edge as the first node of FE
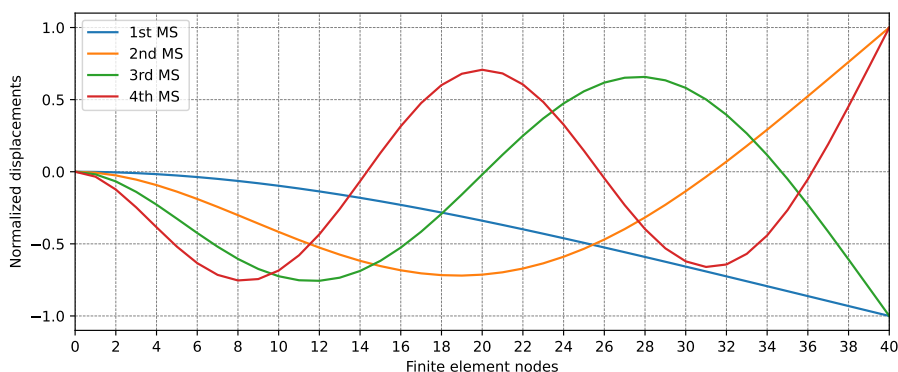
Figure 4.1. First four mode shapes of the Finite Element Model, with normalized displacements and by finite element node.

0 (corresponding to node 0) and the free edge as the last node of FE 39 (corresponding to node 40), the first two DOFs belonging to the first node of FE 0 have null displacement and null rotation respectively, so the first node of FE 0 is also a mode shape node for all mode shapes considered.

Table 4.2. Closest finite element nodes to the mode shape nodes.

Mode shapes	Finite element nodes
1st	0
2nd	0, 31
3rd	0, 20, 35
4th	0, 14, 26, 36

As mentioned in Section 4.1, several scenarios were compared previously, and for the present study the scenario considered is that in which real sensors are placed near the free edge of the beam, virtual sensors are placed near the fixed edge, and damage is introduced in increasing values near the fixed edge as well, as this scenario allowed for the most consistent results among the alternatives. Nevertheless, the focus of this work is studying damage detectability, and in that sense, different scenarios were no further compared. Considering the finite element nodes in Table 4.2, an illustration of the beam, of the real and virtual sensor placements and also of the damage placement is presented in Figure 4.2. The distances from these sensors to the fixed edge of the beam are presented in Table 4.3.

As for damage, in Subsection 1.2.3 it was explained that damage is applied to the structure as a localized percentual reduction of the second moment of area. As such, this study considered the following observations and their respective damage values:

37
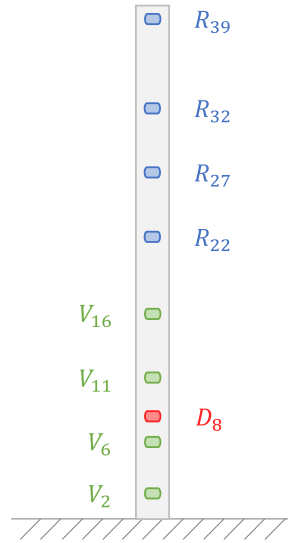
Figure 4.2. Illustration of the beam, of the real and virtual sensor placements (R and V respectively), and also of the damage placement D, where the indexes represent their respective finite element nodes.

Table 4.3. Distances from the real and virtual sensors (R and V, respectively) placed on the experimental structure to its fixed edge, in which the indexes represent their respective finite element nodes.

Sensors	V_2	V_6	V_{11}	V_{16}	R_{22}	R_{27}	R_{32}	R_{39}
Distances [m]	0.065	0.145	0.249	0.353	0.474	0.575	0.678	0.818

- 250 observations of healthy testing, which serve as the baseline reference of the undamaged structure;
- 50 observations of healthy training, to test how the new observations behave when no damage is applied;
- 50 observations with 3% damage applied;
- 50 observations with 5% damage applied;
- 50 observations with 8% damage applied;
- 50 observations with 10% damage applied;

For a total of 500 observations, time responses are generated for all FE nodes and saved for the real sensors of interest. In order to generate those simulated time-series responses from the white noise excitation applied to the beam, with characteristics presented in Table 4.1, time domain characteristics have to be set: the sampling frequency, as presented in Subsection 2.2.4, is 512 Hz, and the sampling time is 5 s.

The numerical application consists of applying increasing damage on FE node 8, distanced 0.186 m from the fixed edge of the beam. The next Subsection presents the results obtained

and details the comparison between modal identification methods SSI-COV and EFDD.

As introduced in Subsection 2.2.2, the python software is used in this study, and like the EFDD implementation, this one also uses an open-source package (accessible in [70]), developed by Kvåle et al. in [49]. Because the structure has new characteristics when compared to the previous study, a new parameter analysis had to be performed. The parameters that produced the best results without increasing the computational effort too much are presented in Table 4.4.

Table 4.4. Parameters considered for the numerical SSI-COV analysis.

Maximum model order	160
Stabilization level	6
Number of blockrows	36
Stabilization criteria (MAC)	0.94

As for the EFDD method, the parameters that most influence results are the frequency intervals for the curve fittings, and the time intervals for the auto-correlation functions. As explained in Subsection 2.2.3, the frequency intervals are defined around the identified peaks of the PSD, allowing for an automated selection of the peaks and thus, an automated identification of the natural frequencies. As such, the parameters considered for this study are presented in Table 4.5, where the frequency intervals are defined in the neighbourhood of the identified peaks.

Table 4.5. Parameters considered for the numerical EFDD analysis.

Natural frequencies	Frequency intervals [Hz]	Time intervals [s]
1st	[± 3]	[0.01, 0.12]
2nd	[± 4]	[0.01, 0.09]
3rd	[± 5]	[0.01, 0.05]
4th	[± 4]	[0.01, 0.05]

These parameters are used throughout the numerical application in identifying the modal parameters using only real time responses and using real and virtual time responses.

39

4.2.2 Comparison between SSI-COV and EFDD

4.2.2.1 Real responses only

In this first case, only real time responses are used in the modal identification process, and damage detectability is verified and measured using the responses measured only by the real sensors placed on the beam. An illustration of this case is presented in Figure 4.3.
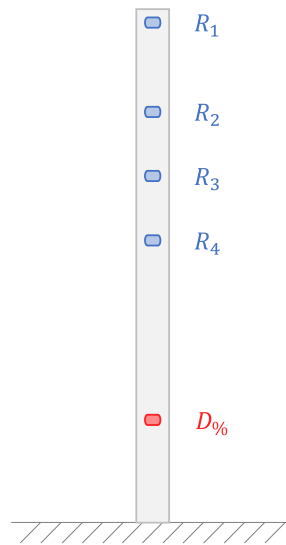
**Figure 4.3.** Illustration of the beam, of the real sensor placements R and of the damage placement D, where the indexes represent the numbering of the sensors, ordered free-fixed edge.

Remembering the natural frequencies from the FEM, presented in Equation 4.1, and observing the first 250 undamaged observations presented in Figure 4.4, the natural frequencies identified from both methods are close to each other, overall. Slight oscillations are expected, given the random nature of the excitation, and still the identified frequencies are close to those from the FEM.

The MAC matrices obtained between each method and the FEM also support the closeness between the methods, as they present very similar results – these matrices are presented in Appendix A, Figure A.1 for the SSI-COV method and Figure A.2 for the EFDD method. This can be observed by calculating the percentual differences between MAC matrices obtained from each method, as presented in Figure 4.5, in which the diagonal values are expected to be lowest (meaning both methods confirm the difference between the simulated model and the FEM is minimal), none exceeding 0.2%.

When adding damage to the structure, as seen in Subsection 1.1.3, it is expected that natural
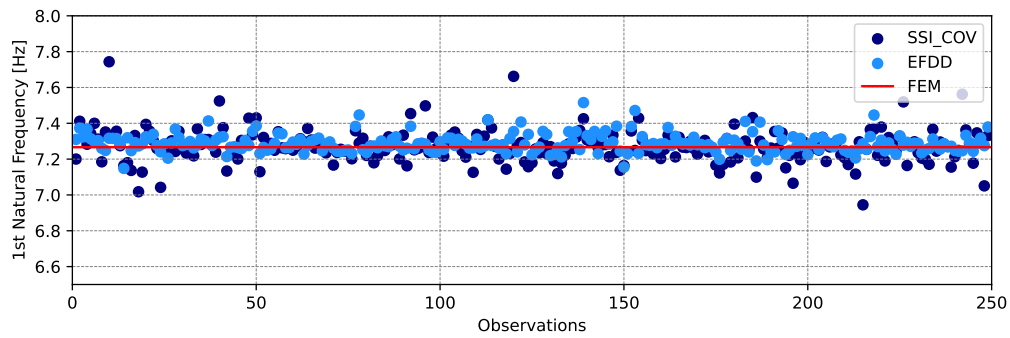
(a) 1st Natural Frequency.
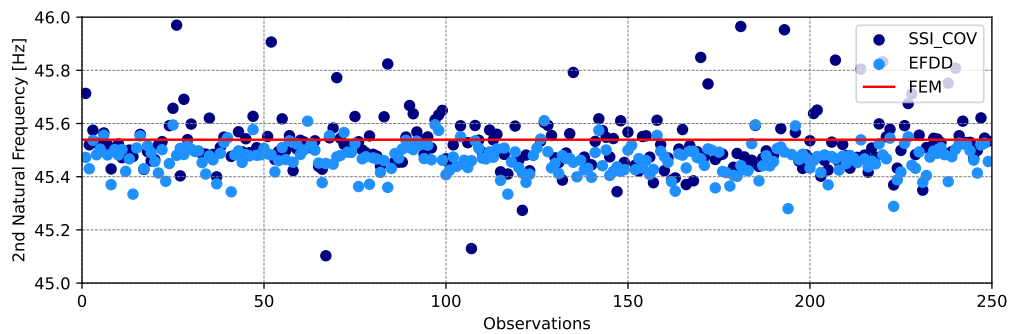
(b) 2nd Natural Frequency.
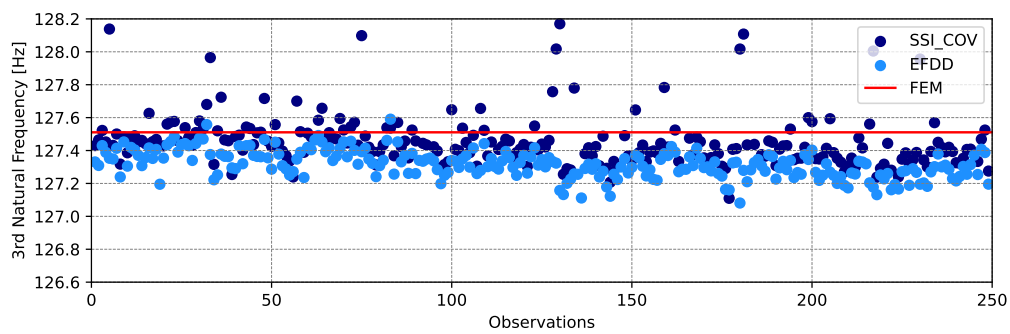
(c) 3rd Natural Frequency.
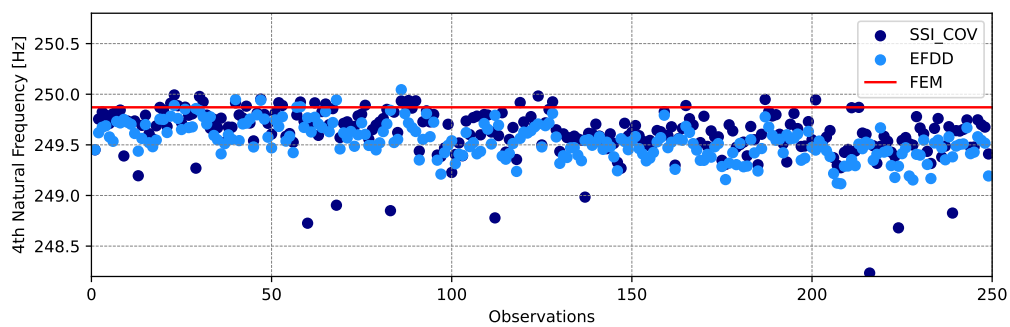
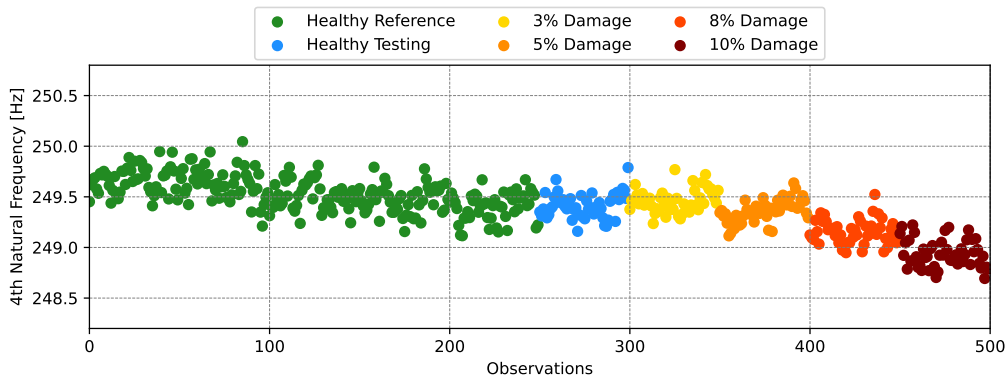**(d)** 4th Natural Frequency.

Figure 4.4. Comparison between each of the four first natural frequencies identified using SSI-COV and EFDD from the first 250 undamaged observations of the numerical application, for the case considering real sensors on top of the beam, and damage on the bottom.
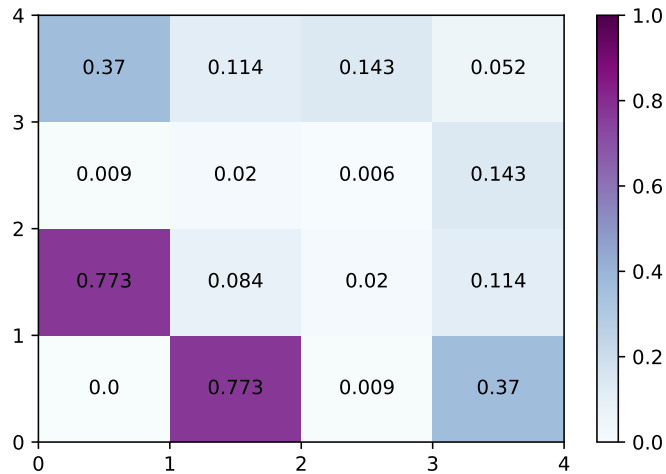
Figure 4.5. Percentual differences between MAC matrices obtained from the SSI-COV and the EFDD modal identification methods for the undamaged observations of the numerical application.

frequencies decrease as a result of a loss of stiffness. The same can be observed in this study with the representation of the 4th natural frequencies identified from the EFDD method for all 500 observations listed in Subsection 4.2.1, as presented in Figure 4.6.

Figure 4.6. 4th Natural frequencies obtained using the EFDD method for all 500 observations (250 undamaged for healthy reference, 50 for healthy testing and 50 for each increasing damage percentage) of the numerical application, considering the real sensor placement on the top of the beam and damage on the bottom.

All the natural frequencies obtained using the SSI-COV method, as well as the remaining natural frequencies obtained using the EFDD method are presented in Appendix A, respectively Figure A.3 and A.4. From these figures, it can be observed that neither the first nor the second natural frequencies display the decrease expected, and that even the third natural frequency displays only a slight decrease, when comparing that of the fourth natural frequencies.

Calculating the MDs gives the distance between (healthy) undamaged and damaged observations, relating all the natural frequencies identified from the time responses. In Figure 4.7, the MDs are plotted for each method. Even though both methods determine similar modal parameters, as seen above, the MDs calculated from the SSI-COV parameters (Figure 4.7a) present less scatter than those from EFDD (Figure 4.7b), enhanced by the different plot scales considered. The values obtained from the SSI-COV method remain mainly below the threshold established, and even though those from the EFDD method present slightly increasing MDs for the highest damage level considered, they still don't exceed the threshold established. From these plots alone, it cannot be concluded with any certainty that there is damage present in the structure.
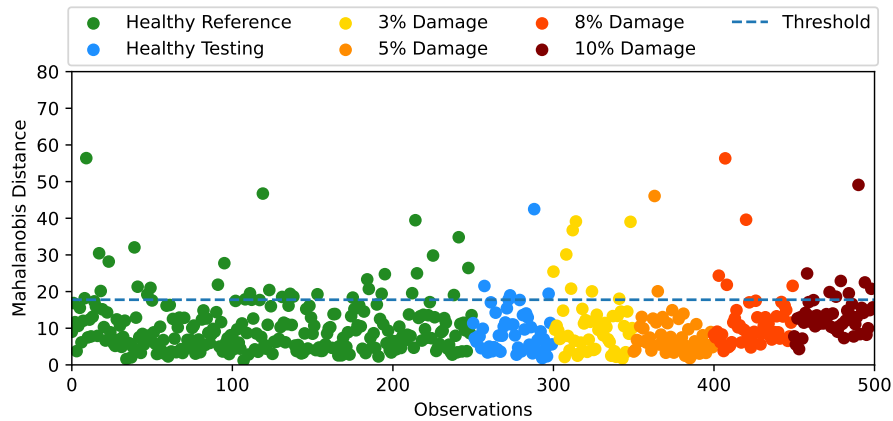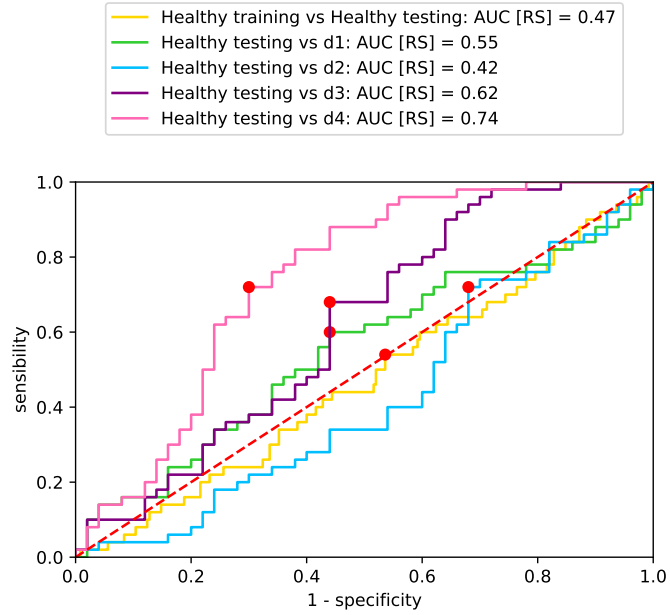
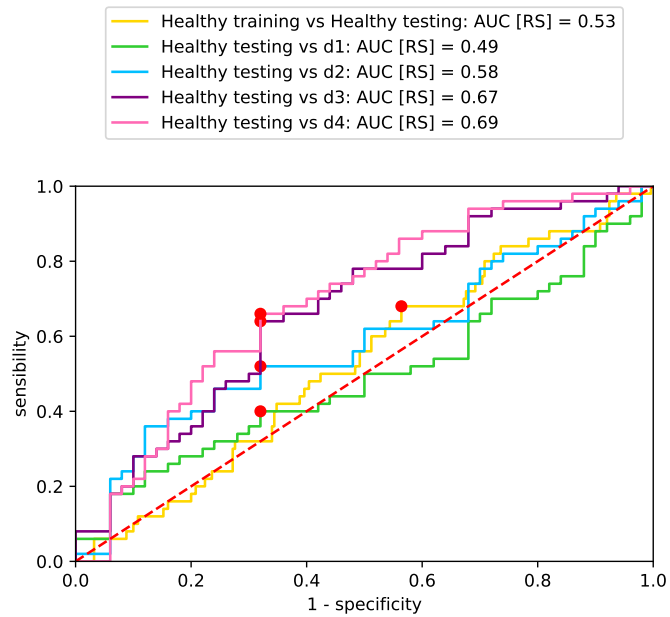**(a)** MD from SSI-COV.
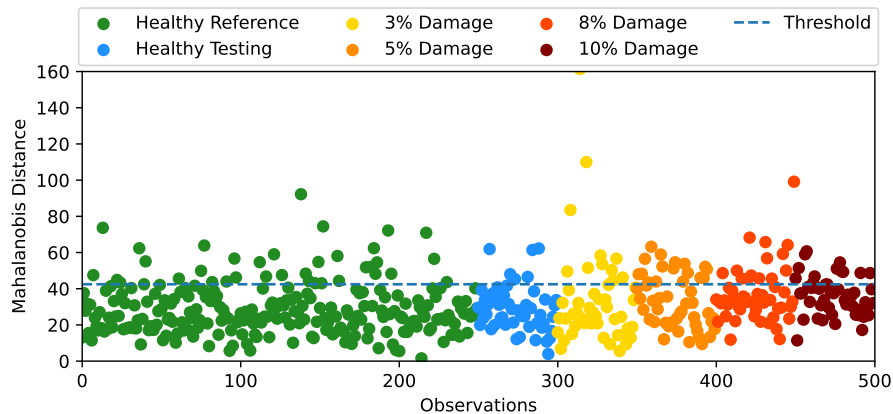
(b) MD from EFDD.

Figure 4.7. Mahalanobis Distances obtained from the SSI-COV and the EFDD methods for all observations of the numerical application, considering the case where real sensors are placed on the top of the beam and damage on the bottom.

Finally, the Areas Under the Receiver Operating Curves are calculated for each method, in which healthy observations are compared to damaged ones. Presented in Figure 4.8, it is observed that the results maintain their similarities between the two modal identification methods, Figure 4.8a for the SSI-COV method and Figure 4.8b for the EFDD method. Also, for both methods, it can be observed that the yellow curves (corresponding to the comparison between healthy training and healthy testing observations, both undamaged) are closest to the red dashed line, as was expected and explained in Subsection 1.2.3. However, neither method presents values as high as expected, where closeness to 1 translates to greatest damage applied and its detectability. Nevertheless, AUC values increase with the increase of damage applied, which is to be expected.

Given the results obtained thus far, the next step is then to obtain the response estimations to virtual sensors, and verify if adding those responses to unmeasured locations will increase damage detectability.

(a) AUC from SSI-COV.

(b) AUC from EFDD.

Figure 4.8. Areas Under the Receiver Operating Curves obtained from the SSI-COV and the EFDD methods for all observations of the numerical application, considering the case where real sensors are placed on the top of the beam and damage on the bottom.

4.2.2.2 Real and virtual responses

When adding response estimations to the real measurements already studied, several virtual sensor combinations can be used in the modal parameter extraction from each method used. Four real sensors and up to four virtual sensors can be used, as illustrated in Figure 4.9, where the both sets of sensors are numbered from closest to farthest from the top of the beam. These sensors follow the same FE placement illustrated on Figure 4.2 and the distances presented in Table 4.3.
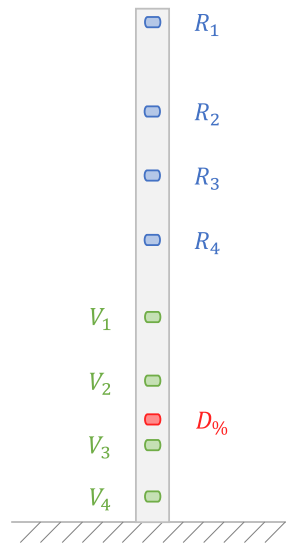
Figure 4.9. Illustration of the beam, of the real and virtual sensor placements (R and V respectively), and also of the damage placement D, where the indexes represent the numbering of the sensors, ordered free–fixed edge.

It is expected that responses closest to the fixed edge of the beam are characterized with the lowest amplitudes of motion, and as to reduce processing times, responses from virtual sensors farthest from the fixed edge were preferred over those closest to it. The virtual sensor combinations used in this study, minding the numbering in Figure 4.9, are as follows:

- V1
- V2
- V3
- V4
- V1V2
- V1V3
- V2V3
- V1V2V3
- V1V2V3V4

For each of these combinations, responses were estimated to the respective virtual sensor locations considered, modal parameters were identified, MDs were calculated and finally, ROCs were obtained and AUCs were determined. In previous studies, it was concluded that response estimation using the MDE method presents a high correlation between responses measured in a location and the virtual responses obtained to that same location. Therefore, the MDE method is the one used in this Subsection, where results are obtained for each method and compared. The comparison between response estimation methods is presented and discussed in the next Subsection.

Considering, for example, the case where virtual responses from sensor V1 are added to the real responses, both methods are still capable of identifying close values for each natural frequency, as presented in Figure 4.10. As seen before, the decrease in natural frequency is slightly noticeable for the third natural frequency (Figure 4.10c) and most noticeable for the fourth natural frequency (Figure 4.10d). For each of the remaining virtual sensors combinations, the plots comparing the four natural frequencies are presented in Appendix A, Section A.2 – from Figure A.5 to A.12.

From the fact that only the third and fourth natural frequencies present some decrease in values, the MDs could have some difficulty in exceeding the threshold established. In Figure 4.11, the MDs for both methods are presented, and it can be observed that, like in Subsubsection 4.2.2.1, the values obtained from SSI-COV (Figure 4.11a) present less scatter than those obtained from EFDD (Figure 4.11b). For each of the remaining virtual sensors combinations, the MDs are presented in Appendix A, Section A.2 – from Figure A.13 to A.20.
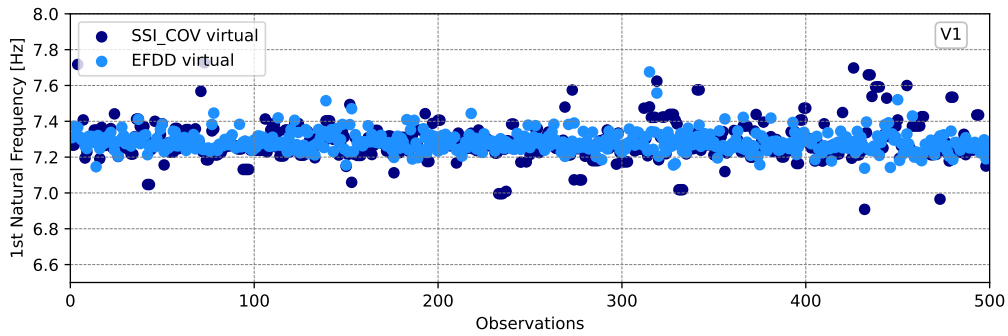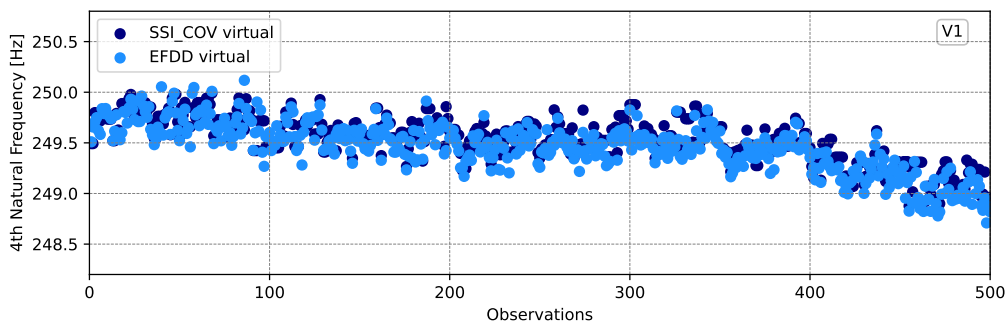
(a) 1st Natural Frequency for V1 – MDE.
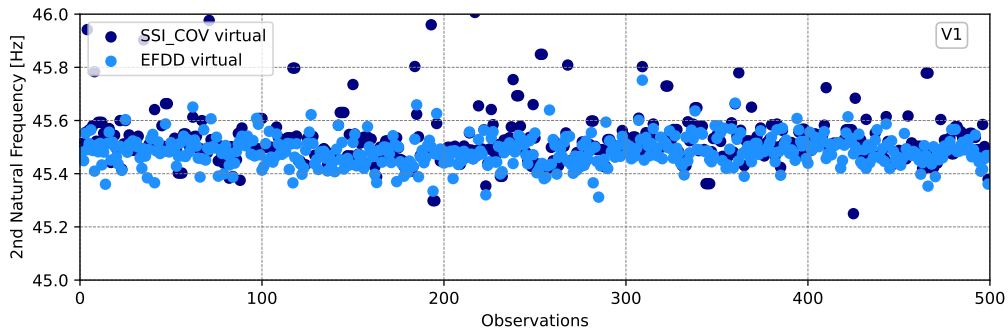
(b) 2nd Natural Frequency for V1 – MDE.
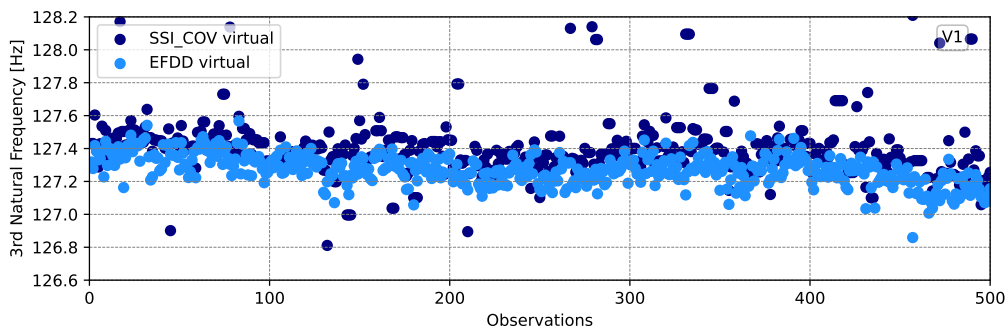

**(c)** 3rd Natural Frequency for V1 – MDE.

(d) 4th Natural Frequency for V1 – MDE.

Figure 4.10. Comparison between each of the four first natural frequencies identi-
fied using SSI-COV and EFDD for all observations of the numerical
application, for the case considering real sensors on top of the beam,
virtual responses from MDE sensor V1 and damage on the bottom.

However, unlike the previous case where only real responses are used, the MDs obtained from the SSI-COV method present a noticeable increase for last two damage values applied, and only about half of those observations exceed the threshold. Given the scatter observed in the MDs obtained from the EFDD method, a more considerable number of observations exceed the threshold, but this alone is not a sufficient indication of the presence of damage, as explained in Subsection 1.2.3. As such, for both of these methods, it can be expected that damage detectability will increase with the use of virtual responses as overall more observations exceed the threshold.
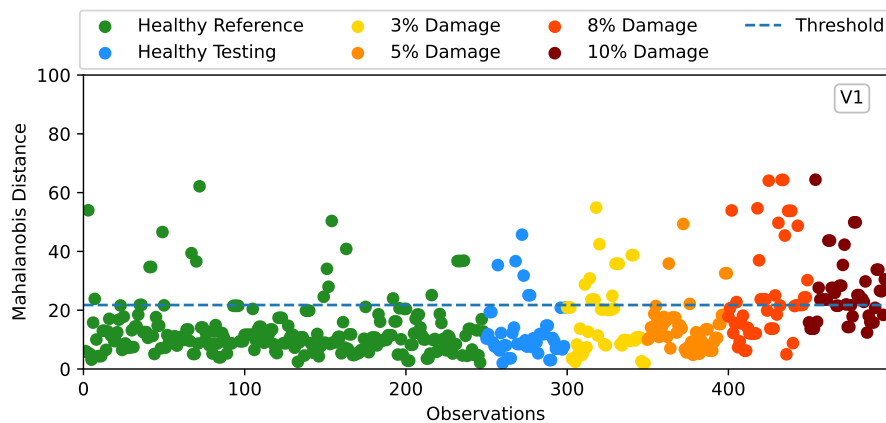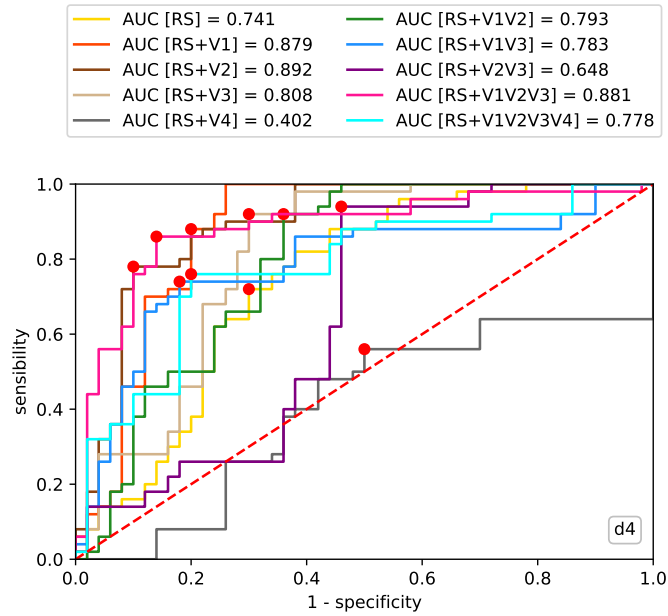

(a) MD for V1 from SSI-COV – MDE.
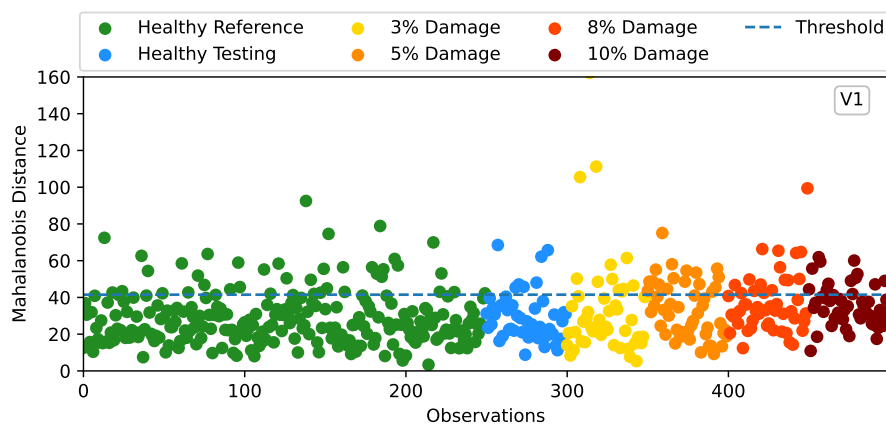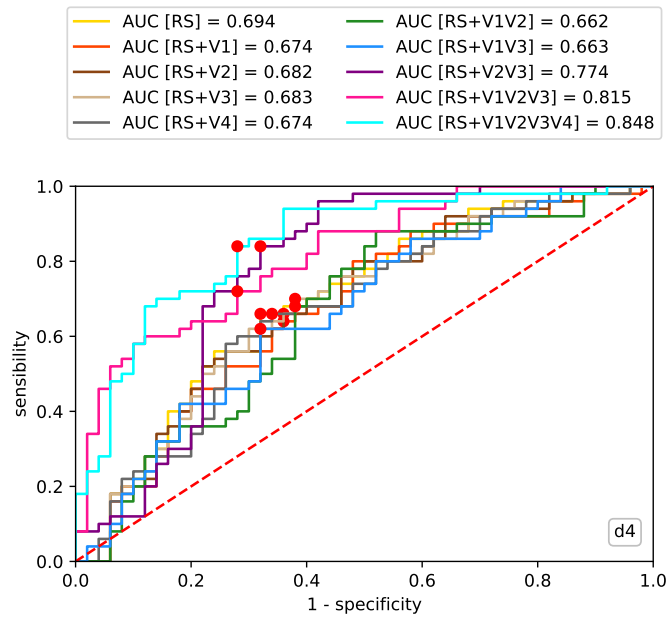

(b) MD for V1 from EFDD – MDE.

Figure 4.11. Mahalanobis Distances obtained from the SSI-COV and the EFDD methods for all observations of the numerical application, considering the case where real sensors are placed on the top of the beam, virtual responses from MDE sensor V1 are added and damage is on the bottom.

Considering the highest damage level applied to the beam, the AUCs from each method are presented in Figure 4.12. Remembering the damage detectability measurements considering only the real responses, presented in Figure 4.8, both methods now present higher AUC values, which mean increased detectability when using virtual responses, for most of the virtual sensor combinations considered. Also, when adding only the responses from the fourth virtual sensor (located closest to the fixed edge of the beam), both methods present a decrease in damage detectability, which sustains the previously mentioned preference of virtual sensors farthest from the fixed edge over the closest ones. For each of the remaining observations, undamaged and the three damage values applied, the AUCs are presented in Appendix A, Section A.2 – Figure A.21 for SSI-COV and A.22 for EFDD.

Even though the maximum AUC values obtained from both methods are rather close – 0.892 for SSI-COV, sensor V2 in Figure 4.12a, and 0.848 for EFDD, sensors V1V2V3V4 in Figure 4.12b –, the overall values are higher for the SSI-COV method, meaning that a parameter adjustment might be necessary for the EFDD method.

(a) AUC for the highest damage level from SSI-COV – MDE.

(b) AUC for the highest damage level from EFDD – MDE.

Figure 4.12. Areas Under the Receiver Operating Curves obtained from the SSI-COV and the EFDD methods for all observations and all virtual sensor combinations for the highest damage level applied, considering the numerical application, the case where real sensors are placed on the top of the beam, virtual sensors from MDE and damage on the bottom.

4.2.3 Comparison between MDE and Transmissibility

Following the comparison between modal identification methods where MDE was the only expansion method used to obtain virtual responses, the goal is to now apply the Transmissibility method and compare their results. As seen in Section 3.3, the Transmissibility method needs to obtain the receptance matrix $\mathbf{H}$ in order to determine the virtual responses at unmeasured locations, but in the frequency domain. For that, Fast Fourier Transform (FFT) is applied to each time response. In the present work, only a simpler, limited version of this method was developed, which considered an undamped system defined by:

$$[-\omega^2\mathbf{M} + \mathbf{K}] \cdot \mathbf{Y}(\omega) = \mathbf{F}(\omega) \tag{4.2}$$

from which $\mathbf{H}$ becomes,

$$\mathbf{H}(\omega) = [-\omega^2\mathbf{M} + \mathbf{K}]^{-1} \tag{4.3}$$

In order to apply Equation 3.9, the full mass and stiffness matrices $\mathbf{M}$ and $\mathbf{K}$ are accessible from the FEM of the structure in study, and the DOFs of the real and virtual sensor placements on the beam are considered when truncating the $\mathbf{H}$ matrices. For this application, a different set of time-series responses was considered, maintaining the excitation properties and remaining characteristics defined in Subsection 4.2.1, namely the beam properties and characteristics, the sensor placements, the number of observations, their distribution and the damage values considered. Also, only one virtual sensor combination was considered – V1V2V3V4 – as this is a first development of this expansion method, and the focus is then to check how the method behaves when compared to MDE. Time responses at measured locations are transformed into responses in the frequency domain, which are then estimated at unmeasured locations and transformed back into the time domain using the IFFT, so that modal identification can be performed.

For this comparison, responses were estimated using both MDE and Transmissibility, and modal parameters were identified using both SSI-COV and EFDD. The comparison between natural frequencies obtained from both expansion methods using SSI-COV is presented in Figure 4.13. Given the random nature of the excitation applied and the different set of responses considered for this application, the SSI-COV method was not capable of identifying all of the 500 observations, as discussed in previous Subsections. Nevertheless, from this comparison between natural frequencies, both methods allowed the identification of close values without too many outliers, even when considering the undamped system. Like in the previous Subsection using only MDE, it can also be observed that a decrease in frequency is only noticeable in

the fourth natural frequency (Figure 4.13d). This observation, along with the fact that it was not possible to obtain the 500 natural frequencies wanted, it would be expected that damage detectability decreases, as with less data points, MDs would decrease and ROCs would be much harder to plot and analyse.
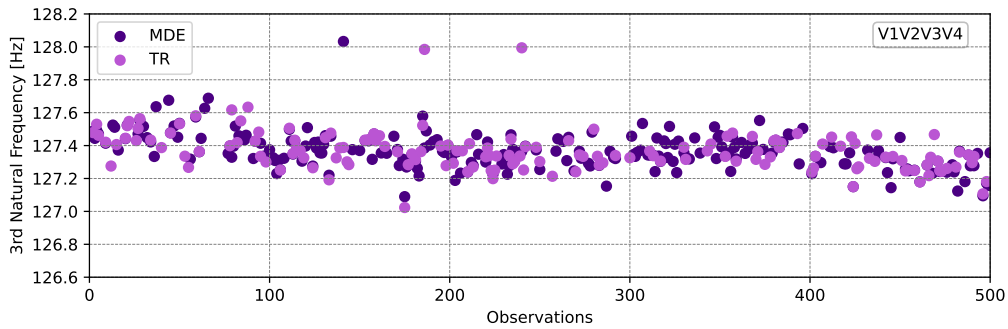
The comparison between natural frequencies obtained from EFDD is presented in Figure 4.14. Unlike SSI-COV, which has more restrictive conditions and is capable of filtering outliers, EFDD is not yet capable of this filtering process and as such, obtains modal parameters that somewhat diverge from the FEM values used as reference for the aforementioned conditions. As a result, natural frequencies obtained from this method present scattered distributions in all frequencies. Nevertheless, a decrease in the fourth natural frequency is noticeable in Figure 4.14d, as observed in the previous method, for both expansion methods. In this case, because this method obtains all 500 natural frequencies (closer or farther from the FEM reference values), there are more data points available to analyse damage detectability, making this process easier. Regardless of the number of observations measured and the difficulty that it implies on damage detectability, when fixating one modal identification method and comparing the natural frequencies obtained from each set of estimated responses proved that both expansion methods yield virtual responses that provide close modal parameters.
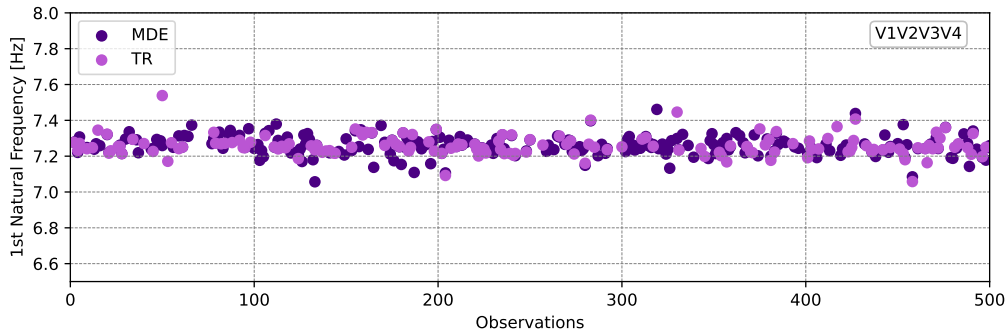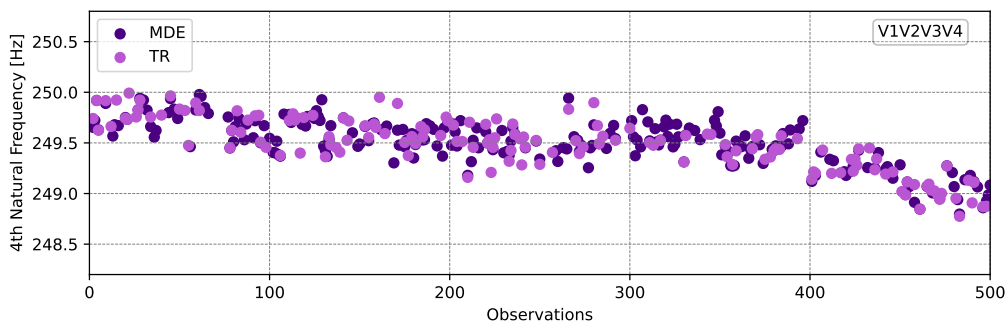
(a) 1st Natural Frequency comparison from SSI-COV for V1V2V3V4 between MDE and TR.
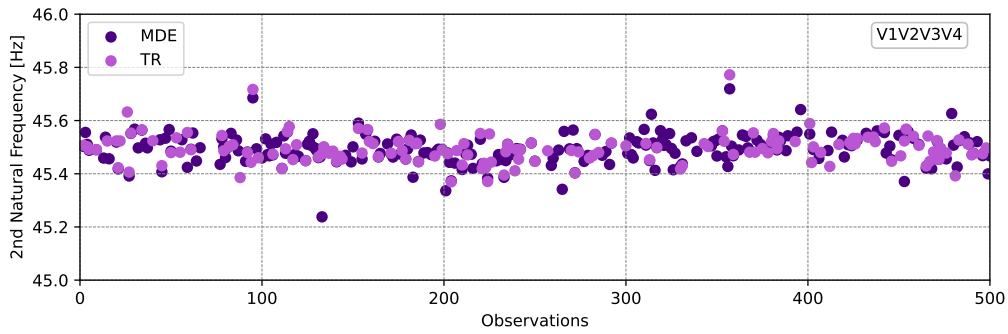
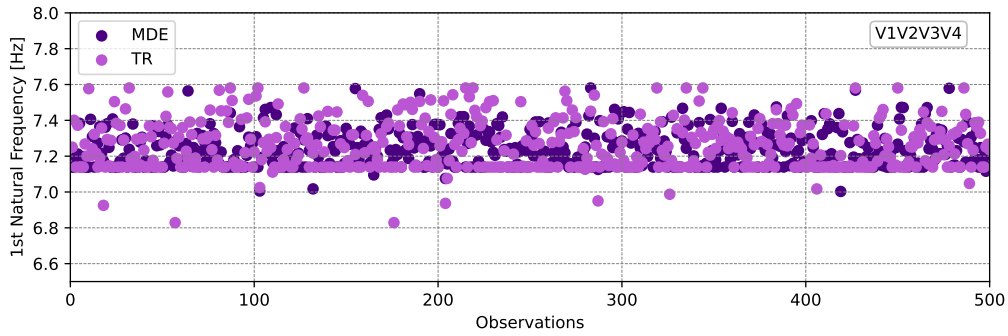**(b)** 2nd Natural Frequency comparison from SSI-COV for V1V2V3V4 between MDE and TR.

(c) 3rd Natural Frequency comparison from SSI-COV for V1V2V3V4 between MDE and TR.
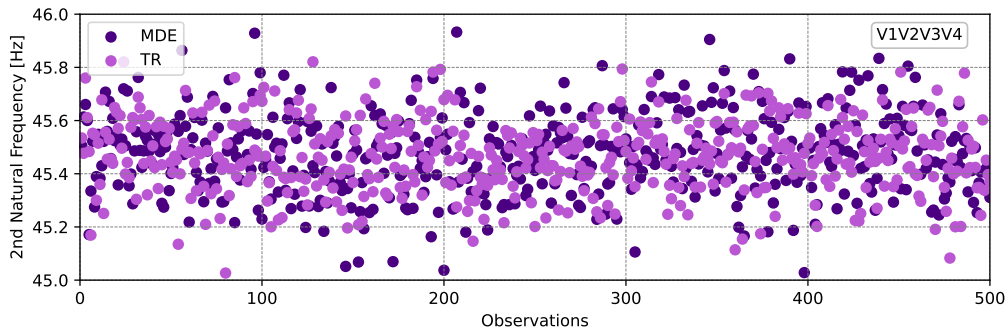

(d) 4th Natural Frequency comparison from SSI-COV for V1V2V3V4 between MDE and TR.
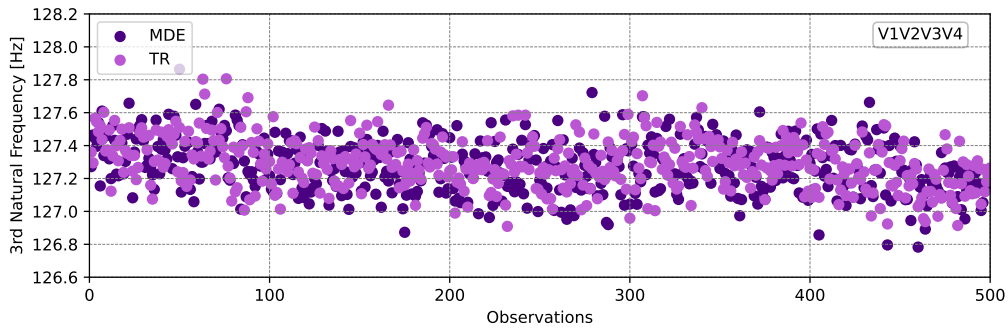
Figure 4.13. Comparison between each of the first four natural frequencies identified using SSI-COV for MDE and Transmissibility (TR) expansions, for all observations of the Transmissibility numerical application, for the case considering real sensors on top of the beam, virtual responses from sensors V1V2V3V4 and damage on the bottom.
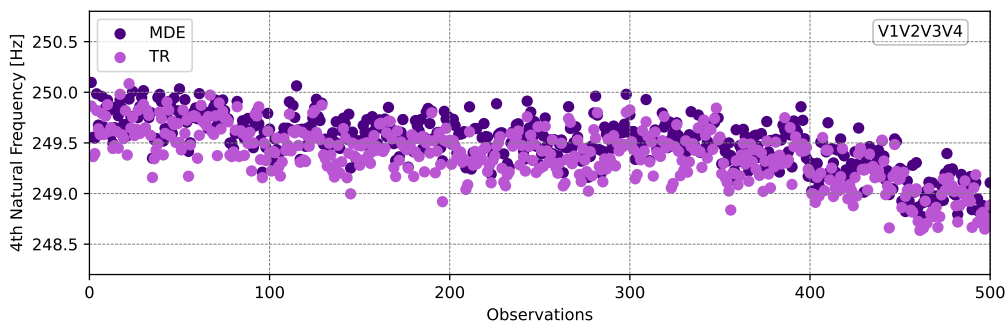
54

(a) 1$^{\text{st}}$ Natural Frequency comparison from EFDD for V1V2V3V4 between MDE and TR.

(b) 2$^{\text{nd}}$ Natural Frequency comparison from EFDD for V1V2V3V4 between MDE and TR.

(c) 3$^{\text{rd}}$ Natural Frequency comparison from EFDD for V1V2V3V4 between MDE and TR.

(d) 4$^{\text{th}}$ Natural Frequency comparison from EFDD for V1V2V3V4 between MDE and TR.

Figure 4.14. Comparison between each of the first four natural frequencies identified using EFDD for MDE and Transmissibility (TR) expansions, for all observations of the Transmissibility numerical application, for the case considering real sensors on top of the beam, virtual responses from sensors V1V2V3V4 and damage on the bottom.

55

4.3 Discussion

Starting with the comparison between modal identification methods presented in Subsection 4.2.2, it was found that adding virtual responses to the real ones increases damage detectability, supporting the conclusions of the previous study.

It was observed that, for the modal parameters of interest in this study, both methods extract close natural frequencies and mode shapes, and even if the final results differ slightly, both support that damage detectability is increased when adding virtual responses to real ones.

Like other modal identification methods, SSI-COV's parameters are dependant on the responses analysed, and several studies must be performed to determine the most adequate set of parameters for the cases studied. For this case, when the model order is low, the method might not be able to capture all four natural frequencies of interest, and when the model order is high, the method can take up to three times longer in identifying the parameters for each observation.

Likewise, the EFDD method too depends on the responses measured and several sets of parameters must be studied, but it is a much faster method overall. For all the virtual sensor combinations mentioned in Subsubsection 4.2.2.2, running computational times were registered, and Table 4.6 presents the average time, measured in seconds per observation, for each method. So, even though the EFDD method produces less certainty in damage detectability, it does provide faster results, in less than a tenth of the time taken by the SSI-COV method.

Table 4.6. Computational times taken by the SSI-COV and the EFDD methods, considering 500 observations for each of all virtual sensor combinations, measured in seconds per observation.

Modal method	Time [s/obs]
SSI-COV	2.4
EFDD	0.2

This fast processing speed also allows for a much more efficient parameter analysis in any practical application, where all the combinations and observations can be studied, modal parameters extracted and parameters adjusted if needed, without the sacrifice of as much time as the SSI-COV method would necessitate.

Many research papers have used these methods in both numerical applications and experimental validations, and also in simply comparing their results and capabilities in their specific applications. Following the numerical application presented in this Chapter, it was seen that

SSI-COV produces higher levels of damage detectability and more consistent results, which is in accordance with [48], [71] and [72], which state SSI-COV's higher complexity and accuracy.

It is seen that the SSI-COV method is capable of extracting modal parameters with high correlation when both the modal order and the number of blockrows are increased. The EFDD method maintains its user friendliness and simplicity to use, as it does not require as much technical and mathematical understanding as the SSI-COV method. However, the higher complexity of the SSI-COV method, both in terms of understanding the method and adjusting its parameters, and also in terms of computational effort, makes it a difficult method to apply without the proper investment. So, for simpler and direct applications, the EFDD method becomes a suitable alternative, obtaining good results with great correlation, even if not as high as those from SSI-COV.

As for the comparison between response estimation methods presented in Subsection 4.2.3, only a limited application was developed and subsequently presented and analysed, but results from the Transmissibility expansion proved close to those obtained from MDE, even when considering an undamped system as the basis of the expansion process. The next step in the development of this method is to obtain the receptance matrices using the modal parameters identified from the measured responses, which inadvertently include the damping that is present of the structure, and compare damage detectability between these methods.

5

Experimental application

Following the numerical application where the results from the two modal identification methods were thoroughly compared, and the response estimation methods were briefly compared, now the objective is to confirm and validate the numerical findings and conclusions with an experimental application. For that, a cantilever beam was placed outside, and with excitation from wind, responses were measured in the same sensor placements as those studied in Chapter 4. The goal is, like in that previous Chapter, to measure the damage detectability using only the responses measured from the four sensors on the top of the beam, and with response estimation, compare it to the damage detectability measured using real and virtual responses.

As such, this Chapter presents the equipments used and the steps of the experimental procedure, followed by the results obtained from each modal identification method, first using only real responses, and then using real and virtual responses. Finally, the comparison between response estimation methods is presented using the experimental data acquired.

5.1   Equipment used and experimental procedure

The beam used in the experimental application has a length of 1 m, in which 0.18 m are inserted in a hydraulic press exerting an average pressure of 200 bar. This way, free length of the clamped-free beam and the remaining properties are the same as those used in the numerical application, presented in Table 4.1.

For this application, the beam was placed outside to be excited only by wind, allowing for a continuous monitoring of the structure. Following the same methodology as the numerical application, responses were measured by four sensors placed on the top of the beam, after the locations of those sensors have been carefully studied in Subsection 4.2.1.

In Figure 5.1, the experimental setup can be observed. Even though eight sensors are placed on the beam at the time of this picture, this study will only use the responses from the aforementioned top four sensors.

Figure 5.1. Beam used in experimental application, with the sensor placements and the hydraulic press to fix one of its edges.

The sensor placement on the beam can be closely observed in Figure 5.2, where a picture of the eight sensors is presented in Figure 5.2a and an illustration of the beam, of the sensor placement and their respective numbering is presented in Figure 5.2b. These sensors have the same locations as the ones presented in Table 4.3. Focusing on the top four sensors used in this study, from which responses will be measured and then estimated to virtual locations, the first three sensors (S_1, S_2 and S_3) are Brüel & Kjær 4507-B-002, and the fourth one (S_4) is a PCB Piezotronics 333B30. Their respective sensitivities and weights are presented in Table 5.1. These sensors, or accelerometers, are characterized by being small, measuring accelerations in a single axis and, when used with their mounting clips, they can withstand harsh operating conditions [73]. Also, their piezoceramic sensing elements allow for strong output signals when low amplitude input vibrations are used [74]. Four of those mounting clips were used in this study, maintaining the sensor placements.

The data acquisition system used is the portable Prosig model P8012, in which all eight sensors are connected [75]. Along with the DATS™ Software, accelerations can be observed
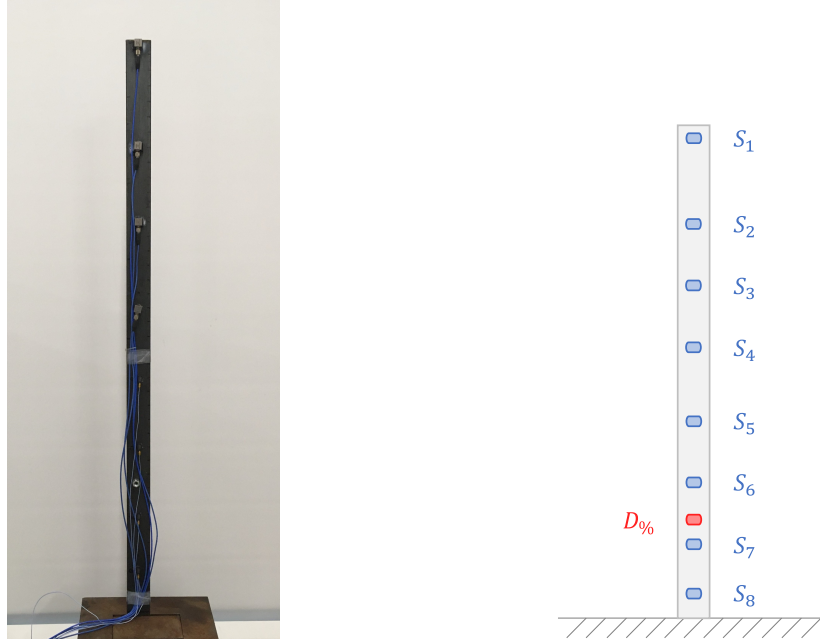
(a) Sensor placement on the experimental beam.

(b) Illustration of the beam and the sensor placement.

Figure 5.2. Sensor placement on the beam used in the experimental application: picture and respective illustration with the eight sensors and their respective numbering, ordered free-fixed edge.

Table 5.1. Sensitivities and weights of the four top sensors placed on the experimental beam.

Sensors	Sensitivity $[\mathrm{m\,V/m\,s^{-2}}]$	Weight [g]
S_1	100.0	4.8
S_2	100.0	4.8
S_3	100.0	4.8
S_4	10.2	4.0

in real time and saved in the specified file types. For this study, the accelerations from each sensor were saved in CSV files and later converted to NPY files in the python code written.

With all the equipment connected, the setup was placed outside to be subjected to wind. For this application, the same frequency sample of 512 Hz is used, and the sampling time is increased to 15 s for each observation. The same number of observations are used as in the numerical application, except now the damage is applied by adding nuts to the structure, as presented in the close-up Figure 5.3.

Each nut weights 2 g, which represent 0.146% of the beam's weight, and up to 4 nuts were used for each set of damaged observations. As such, the observations considered for this application and their respective damage values are as follows:

61

Figure 5.3. Close-up of the damage placed on the beam used in the experimental application.

- 250 observations of healthy testing, which serve as the baseline reference of the un-damaged structure;
- 50 observations of healthy training, to test how the new observations behave when no damage is applied;
- 50 observations with 0.146% damage applied;
- 50 observations with 0.292% damage applied;
- 50 observations with 0.440% damage applied;
- 50 observations with 0.584% damage applied;

5.2   Considerations in the experimental application

The methodology of this experimental application is the same as followed in the numerical application, seen in Chapter 4. Firstly, from the measured responses, modal parameters are identified for each method (SSI-COV and EFDD) and damage detectability is measured. Then, modal parameters are identified for the responses measured and the responses estimated to virtual (unmeasured) locations, and again, damage detectability is measured from the parameters identified by each method.

The SSI-COV parameters considered for this application are the same as those used in the numerical application, presented in Table 4.4. As for EFDD, the frequency intervals had to be slightly adjusted, given the slight differences from the simulated responses to those measured

experimentally, attributed to signal interferences and noise. The EFDD parameters considered for the experimental application are presented in Table 5.2.

Table 5.2. Parameters considered for the experimental EFDD analysis.

Natural frequencies	Frequency intervals [Hz]	Time intervals [s]
1st	[± 2]	[0.01, 0.12]
2nd	[± 4]	[0.01, 0.09]
3rd	[± 5]	[0.01, 0.05]
4th	[± 2]	[0.01, 0.05]

Finally, because there is always a FEM to simulate the structure, whether in a numerical or an experimental application, the existence of sensors alters the mass matrix of the beam. As such, for each sensor and its location, weight is added to its corresponding finite element on the model. Only now can the analysis of the measured responses and results begin.

5.2.1 Comparison between SSI-COV and EFDD

5.2.1.1 Real responses only

Analysing the first four natural frequencies obtained from each method using the experimental measurements, both methods are capable of identifying close values between each other, although presenting a slight overall distance to the natural frequencies from FEM. For each method, the first four natural frequencies are presented in Appendix B, respectively Figure B.3 and B.4. The comparisons between methods for each natural frequency are presented in Figure 5.4. Unlike the numerical case, both the third and fourth natural frequencies (Figure 5.4c and 5.4d, respectively) present very noticeable decreases in values, as expected in the presence of damage.

Considering only the undamaged observations from the real responses measured by the accelerometers placed on the beam, MAC matrices present very similar results, like in the numerical application. The percentual differences between those MAC matrices obtained from each method are presented in Figure 5.5, where diagonal values present a slight increase and non-diagonal values a slight decrease, when compared to the numerical matrix presented in Figure 4.5. Still, there is a high correlation between the FEM and the experimental structure. The experimental MAC matrices for each method are presented in Appendix B, Figure B.1 for the SSI-COV method and Figure B.2 for EFDD.
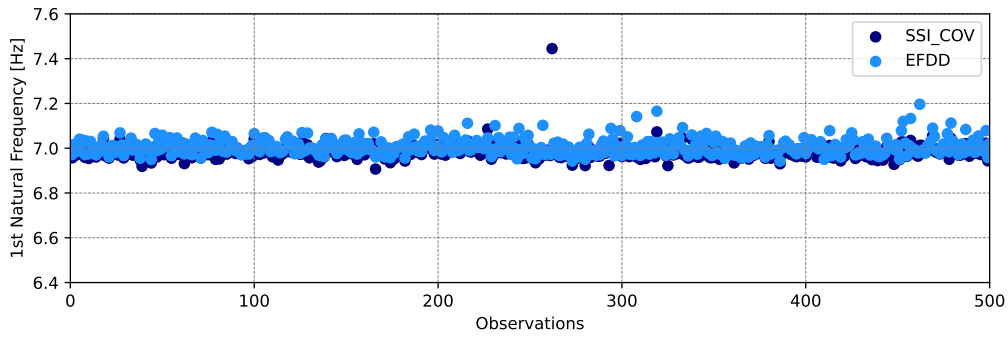
(a) 1st Natural Frequency.
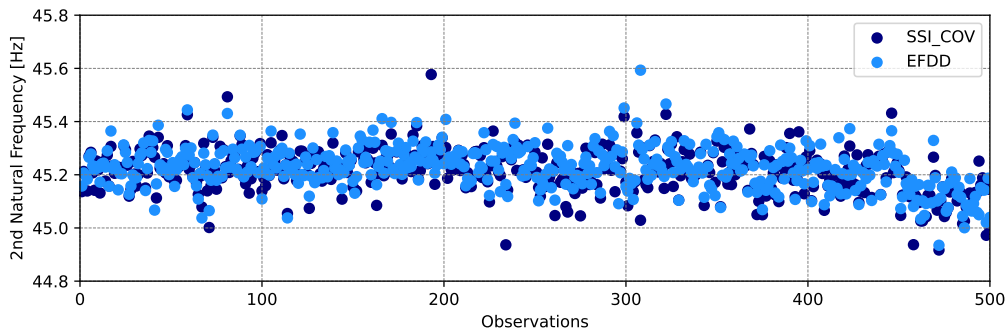
(b) 2nd Natural Frequency.
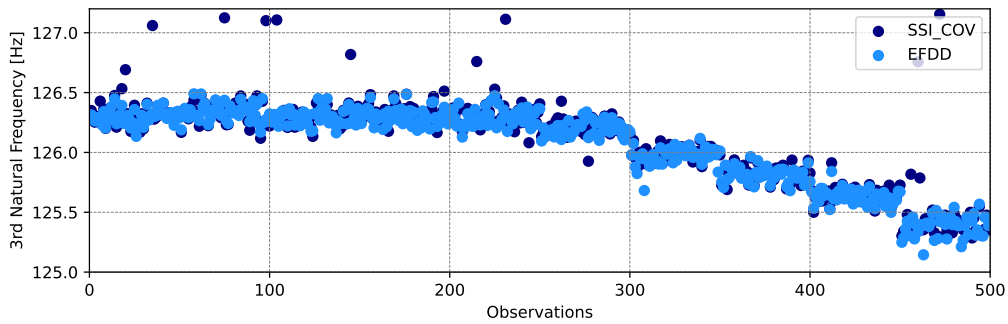
(c) 3rd Natural Frequency.
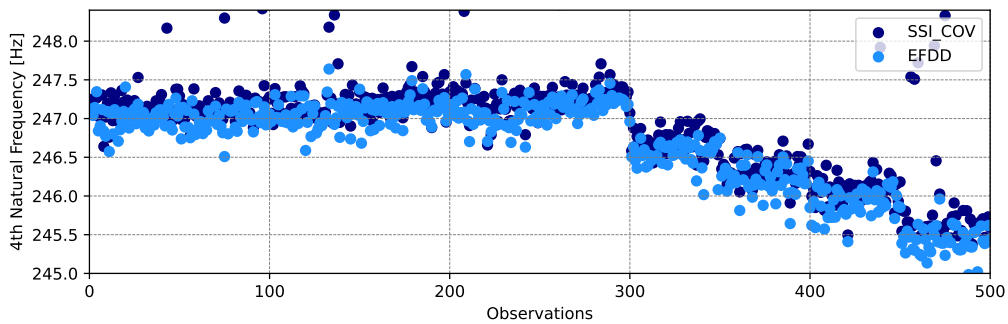
(d) 4th Natural Frequency.

Figure 5.4. Comparison between each of the four first natural frequencies identified using SSI-COV and EFDD for all observations of the experimental application, for the case considering real sensors on top of the beam, and damage on the bottom.
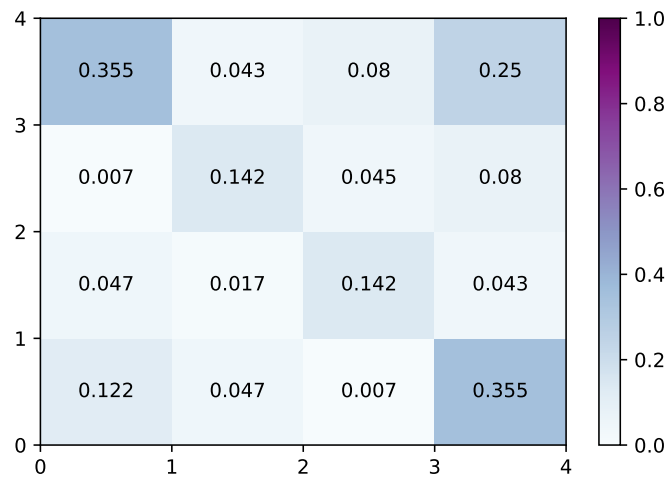
Figure 5.5. Percentual differences between MAC matrices obtained from the SSI-COV and the EFDD modal identification methods for the undamaged observations of the numerical application.

Because the decrease in natural frequencies seen in Figure 5.4c and 5.4d is that much more noticeable than that of the numerical application, where the decrease was only mostly noticeable in the fourth natural frequency, it is then expected that the experimental MDs increase more evidently in the presence of damage, and that can be observed in Figure 5.6, where both methods detect the aforementioned increase. Contrary to the numerical case, and even though the natural frequencies obtained from each method are closer to each other, the MDs obtained from the EFDD method are less scattered and rise above the threshold established for all damage scenarios considered. From these plots, it can be expected that damage detectability is higher for EFDD than for SSI-COV.

The Areas Under the Receiver Operating Curves confirm the expectation set before, in that damage detectability is indeed higher for the EFDD method, where there is practically complete certainty of the presence of damage from the second damage value applied, as presented in Figure 5.7. However, observing the yellow curves from both methods, whereas the AUC value obtained from the SSI-COV method is 0.57, the one obtained from the EFDD method is somewhat higher at 0.71, when the expected value is 0.5 (approximating the red dashed diagonal line). This might mean that EFDD values are inflated, and as such, results might be biased.

Nevertheless, so far the EFDD method has obtained the best results of the two methods compared, and in the next Subsection, virtual responses are added to responses measured from the accelerometers placed on the beam, where it is expected that at least the SSI-COV damage detectability increases.
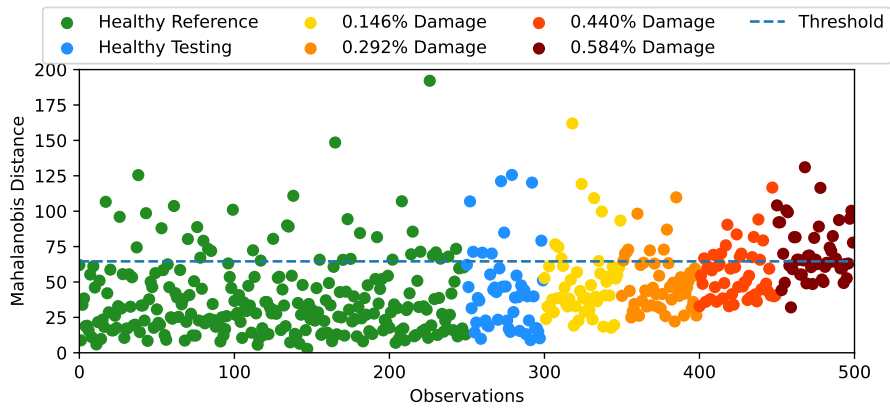
(a) MD from SSI-COV.
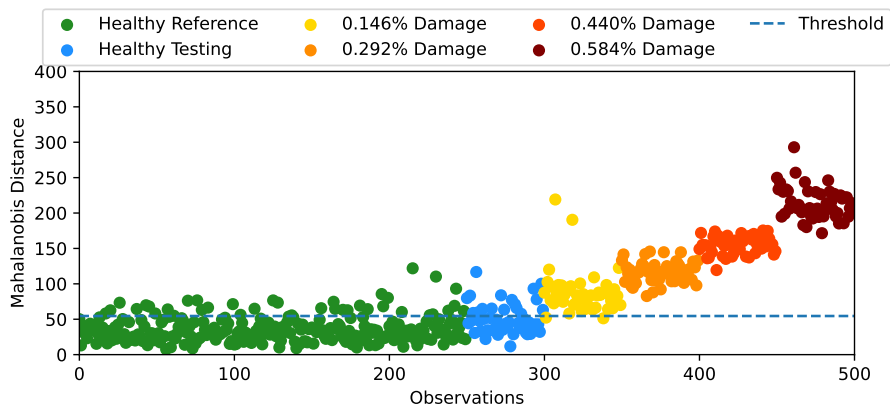
(b) MD from EFDD.

Figure 5.6. Mahalanobis Distances obtained from the SSI-COV and the EFDD methods for all observations of the experimental application, considering the case where real sensors are placed on the top of the beam and damage on the bottom.
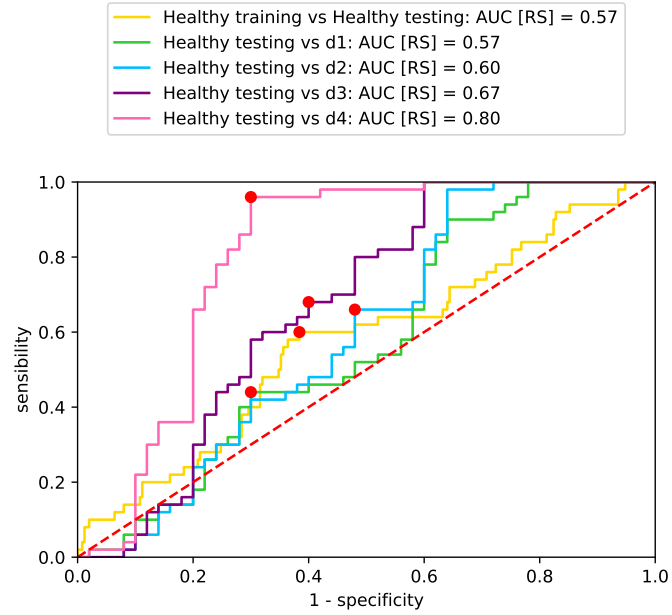
(a) AUC from SSI-COV.
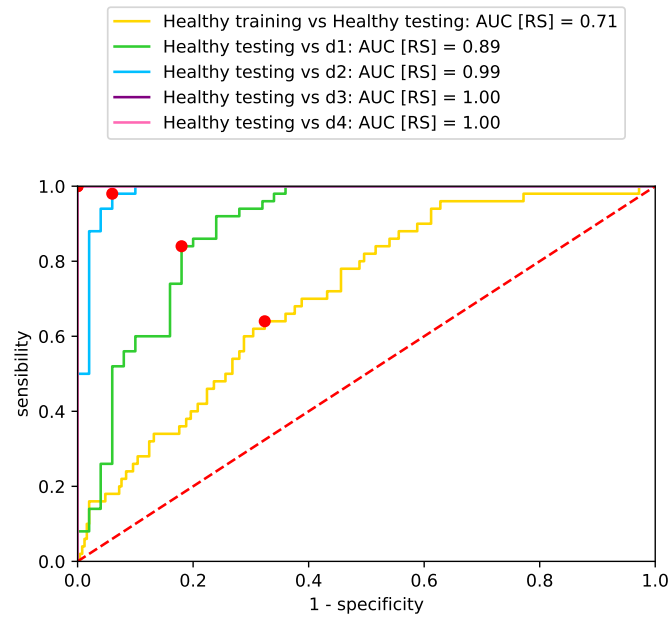
(b) AUC from EFDD.

Figure 5.7. Areas Under the Receiver Operating Curves obtained from the SSI-COV and the EFDD methods for all observations of the experimental application, considering the case where real sensors are placed on the top of the beam and damage on the bottom.

5.2.1.2 Real and virtual responses

The same virtual sensor combinations as those studied in Subsubsection 4.2.2.2 are used in this application. In plotting the natural frequencies for each of those combinations, it can be observed that still the third and fourth natural frequencies present the decrease in value observed in the modal parameters identified from the measured responses only. It can also be observed that, in some combinations, EFDD presents slightly more scatter in the second and fourth natural frequencies, as observed in the natural frequencies for the virtual sensors V1V2, as presented in Figure 5.8. For the remaining combinations, the comparisons between natural frequencies are presented in Appendix B, Section B.2 – from Figure B.5 to B.12.

Presented in Figure 5.9, the MDs calculated for this combination show an improvement on the value distribution of the SSI-COV method, where all damaged observations above the second damage value applied exceed the established threshold, as seen in Figure 5.9a. As for the EFDD method, this combinations doesn't provide results as good as those from only measured responses, but still all damaged observations from the third damage value applied exceed the threshold, seen in Figure 5.9b. Even with these particularities between methods, there is no doubt that there is damage present on the beam. For each of the remaining virtual sensors combinations, the MDs are presented in Appendix B, Section B.2 – from Figure B.13 to B.20.

This is then supported with damage detectability measurements given by the AUCs. For the highest damage level applied, presented in Figure 5.10, the SSI-COV method reaches a maximum value of 1 on three virtual sensor combinations, and all virtual sensor AUCs exceed the AUC from the measured responses only (Figure 5.10a). As for the EFDD method, because there is already a maximum AUC measurement obtained from the measured responses only, only one virtual combination manages to reach that level (Figure 5.10b). Nevertheless, AUCs are still high.

For both methods, six of the nine virtual sensor combinations studied exceed AUCs values of 0.95, which is in itself a great level of certainty in damage detectability. For each of the remaining observations, undamaged and the three damage values applied, the AUCs are presented in Appendix B, Section B.2 – Figure B.21 for SSI-COV and B.22 for EFDD.
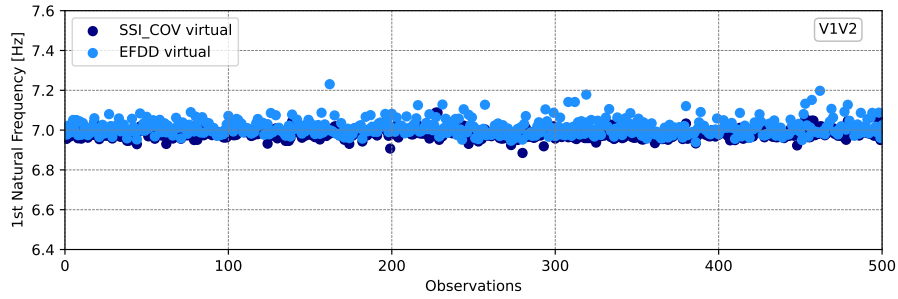
(a) 1st Natural Frequency for V1V2 – MDE.
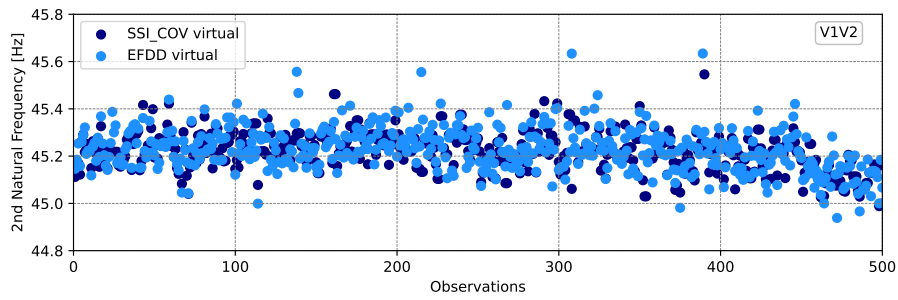
(b) 2nd Natural Frequency for V1V2 – MDE.
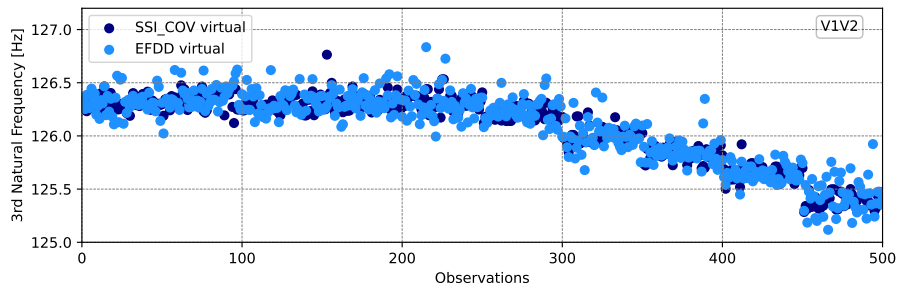
(c) 3rd Natural Frequency for V1V2 – MDE.
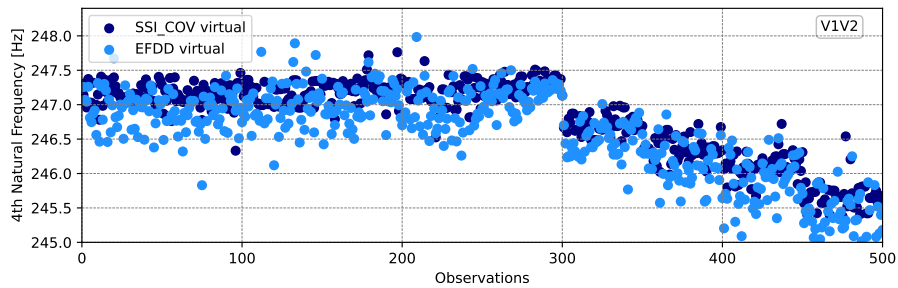
(d) 4th Natural Frequency for V1V2 – MDE.

Figure 5.8. Comparison between each of the four first natural frequencies identified using SSI-COV and EFDD for all observations of the experimental application, for the case considering real sensors on top of the beam, virtual responses from MDE sensors V1V2 and damage on the bottom.
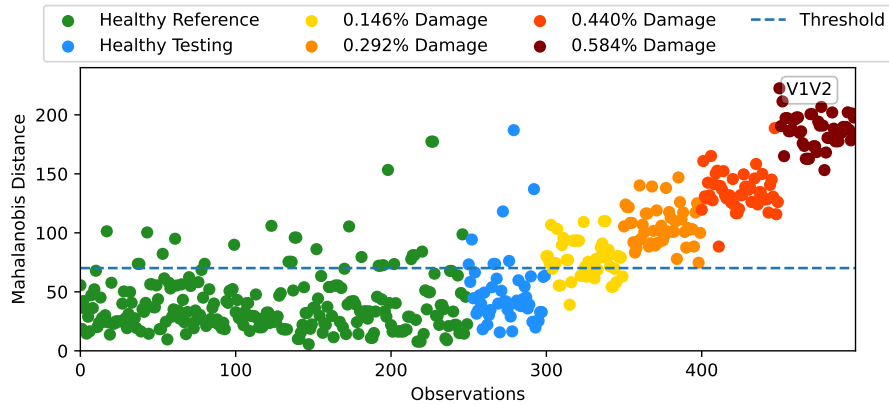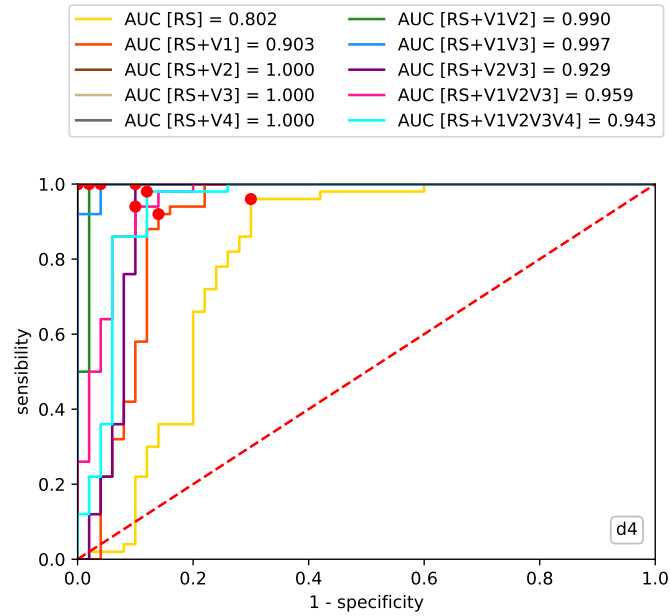
(a) MD for V1V2 from SSI-COV – MDE.
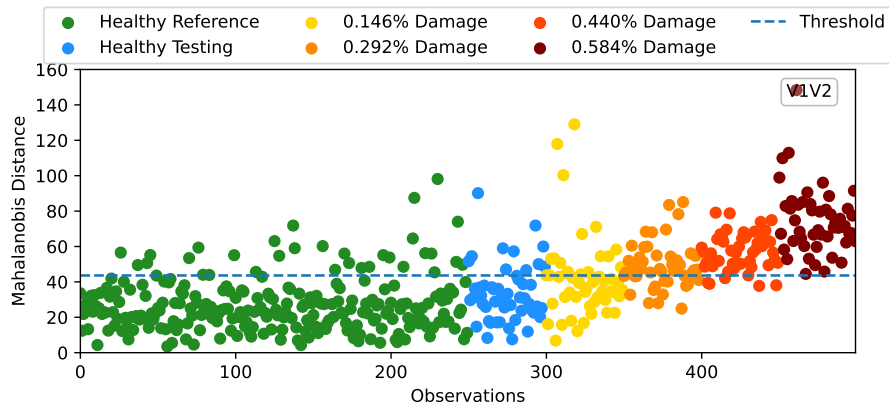
(b) MD for V1V2 from EFDD – MDE.

Figure 5.9. Mahalanobis Distances obtained from the SSI-COV and the EFDD methods for all observations of the experimental application, considering the case where real sensors are placed on the top of the beam, virtual responses from MDE sensors V1V2 are added and damage is on the bottom.

(a) AUC for the highest damage level from SSI-COV – MDE.
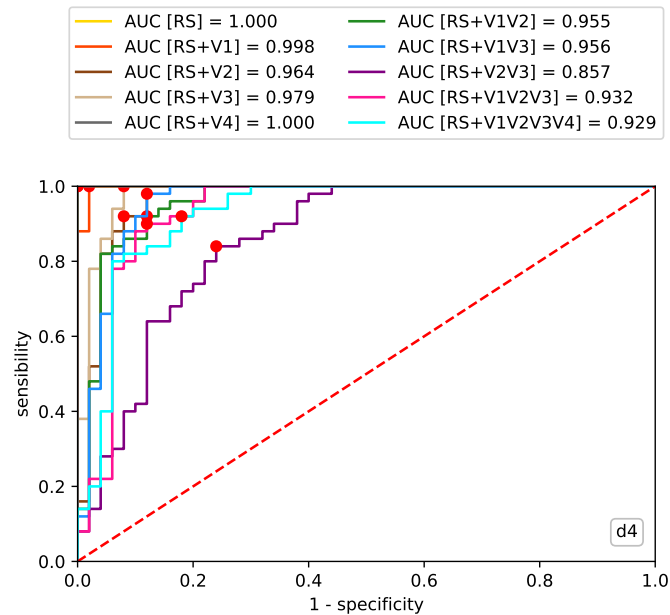
(b) AUC for the highest damage level from EFDD – MDE.

Figure 5.10. Areas Under the Receiver Operating Curves obtained from the SSI-COV and the EFDD methods for all observations and all virtual sensor combinations for the highest damage level applied, considering the experimental application, the case where real sensors are placed on the top of the beam, virtual sensors from MDE and damage on the bottom.

5.2.2 Comparison between MDE and Transmissibility

Like in the numerical application, the experimentally acquired responses were estimated to virtual locations, and fixating each modal identification method, comparisons between expansion methods are obtained. In Figure 5.11, the comparison between the fourth natural frequencies is presented, where it is once again observed that regardless of the modal identification method considered, natural frequencies obtained from responses estimated from either expansion method are close and present the same behaviour – a decrease in natural frequency and a slight scatter in the frequencies obtained from EFDD. The remaining first three natural frequencies are presented in Appendix B, Section B.2 – Figure B.23 for SSI-COV and B.24 for EFDD.
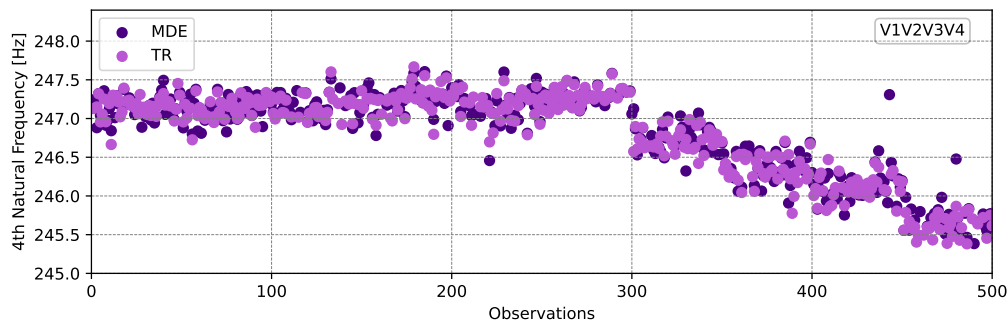
(a) 4th Natural Frequency comparison from SSI-COV for V1V2V3V4 between MDE and TR.
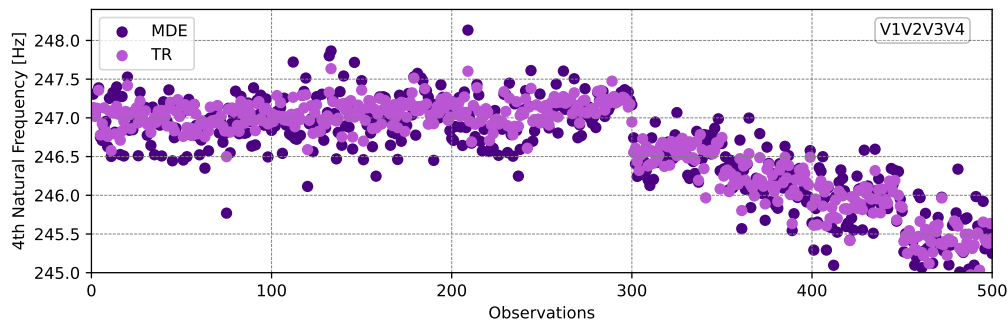
(b) 4th Natural Frequency comparison from EFDD for V1V2V3V4 between MDE and TR.

Figure 5.11. Comparison between the fourth natural frequencies identified using SSI-COV and EFDD for MDE and Transmissibility (TR) expansions, for all observations of the Transmissibility numerical application, for the case considering real sensors on top of the beam, virtual responses from sensors V1V2V3V4 and damage on the bottom.

In this case and unlike the numerical application, the decrease in frequency is much more noticeable in the third (Figure B.23c for SSI-COV and B.24c for EFDD) and fourth natural frequencies (seen above), so it would be expected that MDs and damage detectability increase with the increase of the damage level applied, as seen in the previous Subsection.

5.3 Discussion

As seen in the numerical application on this study, presented in Subsection 5.2.1, adding virtual responses to measured ones increases damage detectability measurements, regardless of the methods used in the modal identification process. Both of those methods are capable of identifying close modal parameters to those obtained from the FEM representing the structure, as seen by the MAC matrices presented in Figure B.2 and B.1, as well as close modal parameters when comparing the results from each method, as seen in Figure 5.5.

The main advantages and disadvantages from each method are still present in this application. With the right set of parameters, the SSI-COV method yields good and consistent results, but not without its high computing times per observation. As for the EFDD method, a slight parameter adjustment was necessary given that now responses are directly inputted to the written code (as they are already accelerations), unlike the numerical case where displacements were measured from the simulated model and then accelerations had to be obtained, before modal identification could begin.

For the simpler structure considered in this study, the experimental results support the findings and conclusions of the numerical application, where natural frequencies were observed to decrease in the presence of damage, and that the higher the damage, the bigger that decrease in value. A more accentuated decrease was observed in the experimental case.

Then, MDs were observed to increase in the presence of damage. Even when considering such low values of damage, the presence of that damage is greatly different than that of the healthy reference baseline, and as a result, step-like behaviour in distribution is observed in both natural frequencies and MDs.

Such noticeable differences in MDs between the sets of observations resulted in clear damage detectability, where for some cases, all damage values applied exceeded the threshold established, as seen by the high AUC levels obtained. With lower levels of damage, some-what high levels of damage detectability were obtained, then confirmed by the higher damage values applied.

As for the comparison between response estimation methods presented in Subsection 5.2.2, this practical example confirmed the close proximity between expansion methods seen in the numerical application.

6 | Conclusion

In studying damage detectability using a virtual sensing technique, this thesis focused firstly in a numerical application, where environmental conditions were simulated using daily temperature variations, and a Gaussian distribution of forces to simulate the wind that excites the structure. Two modal identification methods were applied in extracting the modal parameters, SSI-COV and EFDD. Both methods are capable of obtaining close modal parameters to those from the FEM simulating the structure, and damage detectability measured using numerical results of real and virtual responses were found to be higher than those using only real responses, for both cases.

In that application, SSI-COV was observed to yield less scattered natural frequencies and more consistent results overall, but the parameter selection of this method is highly complex, and several sets of parameters must be studied for the structure in study. Furthermore, in order to extract better modal parameters, the selected SSI-COV parameters must have a wider range, which in turn costs heavily in computational efforts and processing time.

In turn, the EFDD method is known for its user-friendliness and simplicity to use, as well as its fast processing speeds. Because the modal identification is not as automated as that of SSI-COV, parameters must be well defined in order to reduce scatter or poor results, while also having in mind the random nature of the white noise excitation used. As such, a semi automated process was applied in which peaks are selected for each observation's PSD and frequency intervals defined from those peaks, instead of using fixed intervals for all frequencies and observations. This step proved important when modal parameters were found to have great correlation to those from the FEM simulating the structure, much like the SSI-COV method.

However, for the numerical results, SSI-COV still provided greater values of damage detectability than those from EFDD. The former's overall values were slightly higher than the latter's, meaning damage is detected with more certainty.

Then, two response estimation methods were applied and compared, MDE and Transmissibility. Because the Transmissibility expansion method was only briefly developed, this comparison is more limited than the one between modal identification methods. A different set of responses and a single virtual sensor combination were considered, and fixating each modal identification method, modal parameters were obtained. The comparison between natural frequencies showed that, even with the existing limitations, both expansion methods were capable of estimating responses with close modal properties.

The second part of this study was the experimental application, where a cantilever beam with accelerometers was placed outside to acquire the responses needed for modal identification and further analysis. Damage was applied increasingly using small nuts, with percetual values much lower than those used in the numerical application.

Damage detection in the experimental application revealed to be much more enhanced than that in the numerical one. Smaller levels of damage were increasingly applied to the structure, with clearer distinctions between (healthy) undamaged and damaged observations: natural frequencies and MDs present a step-like behaviour in distribution, where each set of observations distanced themselves so much from the previous set, that clear discontinuities can be observed in the respective plots. Consequently, greater values in AUCs were obtained, which meant higher damage detectability and certainty, and both methods support these conclusions.

The SSI-COV method maintained its high computing times per observation, yielding good and consistent results, and the EFDD method maintained its fast processing speeds, even with the slight adjustment of parameters considered.

The same experimentally acquired responses were then considered in the comparison between response estimation methods, where both methods displayed the same close proximity as seen in the numerical application.

It can be concluded that all methods work and provide similar results for this case, where a simpler structure was considered as the representation of a wind turbine blade. The SSI-COV method needs more investment in understanding the complex mathematical concepts and in studying how the adjustment of parameters affects the results obtained, whereas the EFDD method is much simpler and faster to use, but parameters must be set adequately to maintain the high detectability achieved by SSI-COV. As for the expansion methods, MDE demonstrated the high correlation between responses measured and virtual responses obtained to those same locations it is known for, and even with the limited development of the Transmissibility expansion method, it proved thus far capable of estimating responses that yield close modal parameters to those from MDE.

6.1 Future work recommendations

The main focus of this study was the comparison between modal identification methods SSI-COV and EFDD, and so the next step is to further develop the Transmissibility method for response estimation, reducing the present limitations and proceeding to the comparison of damage detectability between expansion methods.

Also, an experimental beam made of steal was used, and the simulated model of both the numerical and the experimental applications had the same properties as that beam. Because wind turbine blades are made of composite materials, a future study could be performed with the experimentation of a cantilever beam made of composite materials, as to better analyse the behaviour of the real structures and materials.

Using a low number of real sensors on the structure has a high industrial and economical value, and with the growth in size of wind turbines, monitoring systems will also have to adapt. This work focused on using data from four sensors placed on the free edge on the beam, and with a virtual sensing technique, responses were estimated at unmeasured locations. If less sensors need be used, a comparative study could be done, applying a virtual sensing technique which allows the expansion to more responses than those measured (like SEREP) and analysing if less sensors provide the same information as using four sensors, as the present study uses, while also checking if damage detectability is influenced by the number of sensors used.

Finally, in order to detect damage and assess its detectability, MDs and AUC-ROCs are obtained for each combination of sensors considered, and it was seen that comparing the latter is much more direct than comparing the former. As such, to aid the comparisons between MD plots, a new metric could be considered which obtains the total number of observations that exceed the threshold established, with the goal of determining whether this number could be, in itself, an indication of the presence of damage.

77

References

[1] A. Rytter. "Vibrational Based Inspection of Civil Engineering Structures". PhD Thesis. Dept. of Building Technology and Structural Engineering, Aalborg University, 1993 (cit. on pp. 1, 4, 5).

[2] K. Kalkanis, S. D. Kaminaris, C. Psomopoulos, and G. C. Ioannidis. "Structural Health Monitoring for the Advanced Maintenance of Wind Turbines: A review". In: 12 (2018), pp. 69–79. ISSN: 2308-1007. URL: https://www.naun.org/main/NAUN/energyenvironment/2018/a202011-010.pdf (cit. on pp. 1–3).

[3] M. Shoaib, I. Siddiqui, S. Rehman, S. Khan, and L. M. Alhems. "Assessment of wind energy potential using wind energy conversion system". In: *Journal of Cleaner Production* 216 (2019), pp. 346–360. ISSN: 0959-6526. DOI: 10.1016/j.jclepro.2019.01.128. URL: https://www.sciencedirect.com/science/article/pii/S0959652619301453 (cit. on p. 1).

[4] European Commission, Directorate-General for Climate Action. *2030 Climate Target Plan*. 2020. URL: https://ec.europa.eu/clima/eu-action/european-green-deal/2030-climate-target-plan_en (cit. on p. 1).

[5] H. F. Zhou, H. Y. Dou, L. Z. Qin, Y. Chen, Y. Q. Ni, and J. M. Ko. "A review of full-scale structural testing of wind turbine blades". In: *Renewable and Sustainable Energy Reviews* 33 (2014), pp. 177–187. ISSN: 1364-0321. DOI: 10.1016/j.rser.2014.01.087. URL: https://www.sciencedirect.com/science/article/pii/S1364032114001105 (cit. on pp. 2, 3).

[6] P. Sadorsky. "Wind energy for sustainable development: Driving factors and future outlook". In: *Journal of Cleaner Production* 289 (2021), p. 125779. ISSN: 0959-6526. DOI: 10.1016/j.jclepro.2020.125779. URL: https://www.sciencedirect.com/science/article/pii/S095965262035825X (cit. on p. 2).

[7] G. Joselin Herbert, S. Iniyan, E. Sreevalsan, and S. Rajapandian. "A review of wind energy technologies". In: *Renewable and Sustainable Energy Reviews* 11.6 (2007), pp. 1117–1145. ISSN: 1364-0321. DOI: 10.1016/j.rser.2005.08.004. URL: https://www.sciencedirect.com/science/article/pii/S136403210500095X (cit. on p. 2).

[8] IEA. *Technology Roadmap – Wind Energy 2013*. IEA, Paris, 2013. URL: https://www.iea.org/reports/technology-roadmap-wind-energy-2013 (cit. on p. 2).

[9]   P. Tchakoua, R. Wamkeue, M. Ouhrouche, F. Slaoui-Hasnaoui, T. Tameghe, and G. Ekemb. "Wind Turbine Condition Monitoring: State-of-the-Art Review, New Trends, and Future Challenges". In: *Energies* 7.4 (2014), pp. 2595–2630. ISSN: 1996-1073. DOI: 10.3390/en7042595. URL: https://www.mdpi.com/1996-1073/7/4/2595 (cit. on p. 2).

[10] B. Yang and D. Sun. "Testing, inspecting and monitoring technologies for wind turbine blades: A survey". In: *Renewable and Sustainable Energy Reviews* 22 (2013), pp. 515–526. ISSN: 1364-0321. DOI: 10.1016/j.rser.2012.12.056. URL: https://www.science direct.com/science/article/pii/S1364032113000129 (cit. on p. 3).

[11] Z. Hameed, Y. S. Hong, Y. M. Cho, S. H. Ahn, and C. K. Song. "Condition monitoring and fault detection of wind turbines and related algorithms: A review". In: *Renewable and Sustainable Energy Reviews* 13.1 (2009), pp. 1–39. ISSN: 1364-0321. DOI: 10.1016 /j.rser.2007.05.008. URL: https://www.sciencedirect.com/science/article /pii/S1364032107001098 (cit. on p. 3).

[12] L. Ziegler, E. Gonzalez, T. Rubert, U. Smolka, and J. J. Melero. "Lifetime extension of onshore wind turbines: A review covering Germany, Spain, Denmark, and the UK". In: *Renewable and Sustainable Energy Reviews* 82 (2018), pp. 1261–1271. ISSN: 1364-0321. DOI: 10.1016/j.rser.2017.09.100. URL: https://www.sciencedirect.com/sci ence/article/pii/S1364032117313503 (cit. on p. 3).

[13] T. Rubert, G. Zorzi, G. Fusiek, P. Niewczas, D. McMillan, J. McAlorum, and M. Perry. "Wind turbine lifetime extension decision-making based on structural health monitor-ing". In: *Renewable Energy* 143 (2019), pp. 611–621. ISSN: 0960-1481. DOI: 10.1016/j .renene.2019.05.034. URL: https://www.sciencedirect.com/science/article /pii/S0960148119306937 (cit. on p. 3).

[14] P. Liu and C. Y. Barlow. "Wind turbine blade waste in 2050". In: *Waste Management* 62 (2017), pp. 229–240. ISSN: 0956-053X. DOI: 10.1016/j.wasman.2017.02.007. URL: https://www.sciencedirect.com/science/article/pii/S0956053X17300491 (cit. on pp. 3, 5).

[15] H. Sohn and C. R. Farrar. "A statistical pattern recognition paradigm for vibration-based structural health monitoring". In: *Smart Engineering System Design, Neural Networks, Fuzzy Logic, Evolutionary Programming, Complex Systems, and Data Mining, St. Louis, MO, USA* (2000). URL: https://digital.library.unt.edu/ark:/67531/metadc72 4463/ (cit. on pp. 3, 4).

[16] C. R. Farrar and S. W. Doebling. "An Overview of Modal-Based Damage Identifica-tion Methods". In: *EUROMECH 365 International Workshop: DAMAS 97, Structural Damage Assessment Using Advanced Signal Processing Procedures*. Los Alamos National Lab.(LANL), Los Alamos, NM (United States), 1997. URL: https://www.osti.gov/b iblio/541870 (cit. on pp. 3, 4).

[17] H. Friedmann and P. Kraemer. "Vibration-based condition monitoring, structural health monitoring, population monitoring – Approach to a definition of the different concepts by means of practical examples from the field of wind energy". In: *Proceedings of the 8th European Workshop on Structural Health Monitoring (EWSHM 2016), Bilbao, Spain*. 2016, pp. 5–8 (cit. on p. 3).

[18] C. C. Ciang, J.-R. Lee, and H.-J. Bang. "Structural health monitoring for a wind turbine system: a review of damage detection methods". In: *Measurement Science and Tech-nology* 19.12 (2008), p. 122001. DOI: 10.1088/0957-0233/19/12/122001 (cit. on p. 4).

[19] S. Doebling, C. Farrar, and M. Prime. "A Summary Review of Vibration-Based Damage Identification Methods". In: *The Shock and Vibration Digest* 30 (1998), pp. 91–105. DOI: 10.1177/058310249803000201 (cit. on p. 4).

[20] E. Gross, M. Rumsey, T. Simmermacher, and R. Zadoks. "Application of Damage Detection Techniques Using Wind Turbine Modal Data". In: *37th Aerospace Sciences Meeting and Exhibit*. 1999, p. 47. DOI: 10.2514/6.1999-47. URL: https://arc.aiaa.org/doi/abs/10.2514/6.1999-47 (cit. on p. 4).

[21] S. W. Doebling, C. R. Farrar, M. B. Prime, and D. W. Shevitz. "Damage Identification and Health Monitoring of Structural and Mechanical Systems From Changes in their Vibration Characteristics: A Literature Review". In: *Technical Report No. LA-13070-MS* 30 (1996). DOI: 10.2172/249299. URL: https://www.osti.gov/biblio/249299 (cit. on p. 4).

[22] S. S. Kessler, S. M. Spearing, M. J. Atalla, C. E. S. Cesnik, and C. Soutis. "Damage detection in composite materials using frequency response methods". In: *Composites Part B: Engineering* 33.1 (2002), pp. 87–95. ISSN: 1359-8368. DOI: 10.1016/S1359-8368(01)00050-6. URL: https://www.sciencedirect.com/science/article/pii/S1359836801000506 (cit. on p. 5).

[23] J. Kang, J. Sobral, and C. G. Soares. "Review of Condition-Based Maintenance Strategies for Offshore Wind Energy". In: *Journal of Marine Science and Application* 18.1 (2019), pp. 1–16. DOI: 10.1007/s11804-019-00080-y (cit. on p. 5).

[24] E. Reynders and G. D. Roeck. "Reference-based combined deterministic–stochastic subspace identification for experimental and operational modal analysis". In: *Mechanical Systems and Signal Processing* 22.3 (2008), pp. 617–637. ISSN: 0888-3270. DOI: 10.1016/j.ymssp.2007.09.004. URL: https://www.sciencedirect.com/science/article/pii/S0888327007001823 (cit. on pp. 5, 7).

[25] B. Peeters. "System Identification and Damage Detection in Civil Engineering". PhD Thesis. Katholieke Universiteit te Leuven (1970-), 2000 (cit. on pp. 5, 18).

[26] N. Dervilis, M. Choi, S. G. Taylor, R. J. Barthorpe, G. Park, C. R. Farrar, and K. Worden. "On damage diagnosis for a wind turbine blade using pattern recognition". In: *Journal of Sound and Vibration* 333.6 (2014), pp. 1833–1850. ISSN: 0022-460X. DOI: 10.1016/j.jsv.2013.11.015. URL: https://www.sciencedirect.com/science/article/pii/S0022460X13009528 (cit. on p. 5).

[27] L. Liu, S. M. Kuo, and M. Zhou. "Virtual sensing techniques and their applications". In: *2009 International Conference on Networking, Sensing and Control*. 2009, pp. 31–36. DOI: 10.1109/ICNSC.2009.4919241 (cit. on p. 6).

[28] E. Balmès. "Sensors, Degrees of Freedom, and Generalized Modeshape Expansion Methods". In: *Proc SPIE* (1999) (cit. on p. 6).

[29] C. Roberts, S. Isbister, C. Murphy, C. Nisbet, P. Sweeney, D. García Cava, and D. Tcherniak. "Strain estimation using modal expansion approach via virtual sensing for structural asset management". In: *1st International Conference on Structural Integrity for offshore energy industry*. 2018. URL: https://asranet.co.uk/Content/Files/SI.pdf (cit. on p. 6).

[30] B. Peeters and G. De Roeck. "Reference-based stochastic subspace identification for output-only modal analysis". In: *Mechanical Systems and Signal Processing* 13.6 (1999), pp. 855–878. ISSN: 0888-3270. DOI: 10.1006/mssp.1999.1249. URL: https://www.sciencedirect.com/science/article/pii/S0888327099912499 (cit. on pp. 7, 15).

[31] J. E. Mottershead and M. I. Friswell. "Model Updating In Structural Dynamics: A Survey". In: *Journal of Sound and Vibration - J SOUND VIB* 167 (1993), pp. 347–375. DOI: 10.1006/jsvi.1993.1340 (cit. on p. 8).

[32] R. J. Allemang and D. L. Brown. "A correlation coefficient for modal vector analysis". In: *Proc. 1st Int. Modal Analysis Conference.* 1982, pp. 110–116 (cit. on p. 8).

[33] C Lein and M Beitelschmidt. "Comparative study of model correlation methods with application to model order reduction". In: *Proceedings 26th ISMA (International Conference on Noise and Vibration Engineering).* Belgium Leuven. 2014, pp. 2683–2700 (cit. on p. 8).

[34] P. C. Mahalanobis. "On the generalized distance in statistics". In: National Institute of Science of India. 1936 (cit. on p. 8).

[35] K. Krishnan Nair and A. S. Kiremidjian. "Time Series Based Structural Damage Detection Algorithm Using Gaussian Mixtures Modeling". In: *Journal of Dynamic Systems, Measurement, and Control* 129.3 (2007), pp. 285–293. ISSN: 0022-0434. DOI: 10.1115/1.2718241. URL: https://asmedigitalcollection.asme.org/dynamicsystems/article-pdf/129/3/285/5650626/285_1.pdf (cit. on p. 8).

[36] S. H. Park, J. M. Goo, and C.-H. Jo. "Receiver Operating Characteristic (ROC) Curve: Practical Review for Radiologists". In: *Korean Journal of Radiology* 5.1 (2004), pp. 11–18. ISSN: 1229-6929. DOI: 10.3348/kjr.2004.5.1.11. URL: http://www.e-sciencecentral.org/articles/?scid=1027596 (cit. on p. 9).

[37] R. Brincker and C. Ventura. *Introduction to Operational Modal Analysis.* John Wiley & Sons, 2015. ISBN: 9781119963158. DOI: 10.1002/9781118535141. URL: https://onlinelibrary.wiley.com/doi/abs/10.1002/9781118535141 (cit. on pp. 13, 14).

[38] G. H. James, T. G. Carne, J. P. Lauffer, and A. R. Nord. "Modal testing using natural excitation". In: *Proceedings of the 10th International Modal Analysis Conference* 2 (1992) (cit. on p. 14).

[39] L. Zhang, R. Brincker, and P. Andersen. "An Overview of Operational Modal Analysis: Major Development and Issues". In: Aalborg Universitet. 2005, pp. 179–190 (cit. on p. 14).

[40] D. Goyal and B. S. Pabla. "The Vibration Monitoring Methods and Signal Processing Techniques for Structural Health Monitoring: A Review". In: *Archives of Computational Methods in Engineering* 23.4 (2016), pp. 585–594. DOI: 10.1007/s11831-015-9145-0 (cit. on pp. 14, 22).

[41] P. Van Overschee and B. De Moor. *Subspace Identification for Linear Systems: Theory – Implementation – Applications.* Springer New York, NY, 1996. ISBN: 978-1-4613-0465-4. DOI: 10.1007/978-1-4613-0465-4 (cit. on p. 14).

[42] B. Peeters and G. De Roeck. "Reference based stochastic subspace identification in civil engineering". In: *Inverse Problems in Engineering* 8 (2000), pp. 47–74. DOI: 10.1080/174159700088027718 (cit. on p. 14).

[43] S. S. Rao. *Mechanical Vibrations.* 5th Edition. Upper Saddle River, NJ: Prentice-Hall, 2011. ISBN: 978-0-13-212819-3 (cit. on pp. 15, 29, 31).

[44] R. R. Craig and A. J. Kurdila. *Fundamentals of Structural Dynamics.* John Wiley & Sons, 2006 (cit. on p. 15).

[45]   R. Brincker and P. Andersen. "Understanding Stochastic Subspace Identification". In: *Conference Proceedings: IMAC-XXIV: A Conference & Exposition on Structural Dynamics*. Society for Experimental Mechanics, 2006 (cit. on pp. 15, 16).

[46]   B. Peeters and G. De Roeck. "Stochastic System Identification for Operational Modal Analysis: A Review". In: *Journal of Dynamic Systems, Measurement, and Control* 123.4 (2001), pp. 659–667. ISSN: 0022-0434. DOI: 10.1115/1.1410370 (cit. on p. 15).

[47]   S. Qin, J. Kang, and Q. Wang. "Operational Modal Analysis Based on Subspace Algorithm with an Improved Stabilization Diagram Method". In: *Shock and Vibration* 2016 (2016), pp. 1–10. DOI: 10.1155/2016/7598965 (cit. on pp. 16, 17).

[48]   F. B. Zahid, Z. C. Ong, and S. Y. Khoo. "A review of operational modal analysis techniques for in-service modal identification". In: *Journal of the Brazilian Society of Mechanical Sciences and Engineering* 42 (2020). DOI: 10.1007/s40430-020-02470-8 (cit. on pp. 16, 57).

[49]   K. A. Kvåle, O. Øiseth, and A. Rønnquist. "Operational modal analysis of an end-supported pontoon bridge". In: *Engineering Structures* 148 (2017), pp. 410–423. ISSN: 0141-0296. DOI: https://doi.org/10.1016/j.engstruct.2017.06.069. URL: https://www.sciencedirect.com/science/article/pii/S0141029616307805 (cit. on pp. 17, 18, 39).

[50]   J. S. Bendat and A. G. Piersol. *Engineering Applications of Correlation and Spectral Analysis*. 2nd Edition. New York: John Wiley & Sons, 1993. ISBN: 978-0-471-57055-4 (cit. on p. 18).

[51]   R. Brincker, L. Zhang, and P. Andersen. "Modal Identification from Ambient Responses using Frequency Domain Decomposition". In: vol. 1. San Antonio, TX, USA. 2000, pp. 625–630 (cit. on p. 19).

[52]   R. Brincker and L. Zhang. "Frequency Domain Decomposition Revisited". In: 2009, pp. 615–626 (cit. on p. 19).

[53]   R. Brincker, C. E. Ventura, and P. Andersen. "Damping Estimation by Frequency Domain Decomposition". In: Society for Experimental Mechanics. 2001, pp. 698–703 (cit. on p. 19).

[54]   J. S. Bendat and A. G. Piersol. *Random Data: Analysis and Measurement Procedures - Revised and Expanded*. Wiley, 1986. ISBN: 978-0-471-04000-2 (cit. on p. 19).

[55]   C. Rainieri and G. Fabbrocino. "Operational modal analysis: overview and applications". In: *Strategies for reduction of the seismic risk* (2008), pp. 29–44 (cit. on p. 20).

[56]   M. R. Carini and M. M. Rocha. "CESSIPy: A Python open-source module for stochastic system identification in civil engineering". Version 1.1. In: *SoftwareX* 18 (2022), p. 101091. ISSN: 2352-7110. DOI: 10.1016/j.softx.2022.101091. URL: https://www.sciencedirect.com/science/article/pii/S2352711022000632 (cit. on p. 20).

[57]   J. O'Callahan, P. Avitabile, and R. Riemer. "System Equivalent reduction Expansion Process". In: *Proceedings of the 7th international modal analysis conference; 1989*. 1989 (cit. on p. 27).

[58]   N. M. M. Maia and T. A. N. Silva. "An expansion technique for the estimation of unmeasured rotational frequency response functions". In: *Mechanical Systems and Signal Processing* 156 (2021), p. 107634. ISSN: 0888-3270. DOI: 10.1016/j.ymssp.2021.107634. URL: https://www.sciencedirect.com/science/article/pii/S0888327021000297 (cit. on p. 27).

[59] M. Tarpø, B. Nabuco, C. Georgakis, and R. Brincker. "Expansion of experimental mode shape from operational modal analysis and virtual sensing for fatigue analysis using the modal expansion method". In: *International Journal of Fatigue* 130 (2020), p. 105280. ISSN: 0142-1123. DOI: 10.1016/j.ijfatigue.2019.105280. URL: https://www.sciencedirect.com/science/article/pii/S0142112319303846 (cit. on p. 28).

[60] K. Maes, A. Iliopoulos, W. Weijtjens, C. Devriendt, and G. Lombaert. "Dynamic strain estimation for fatigue assessment of an offshore monopile wind turbine using filtering and modal expansion algorithms". In: *Mechanical Systems and Signal Processing* 76-77 (2016), pp. 592–611. ISSN: 0888-3270. DOI: 10.1016/j.ymssp.2016.01.004. URL: https://www.sciencedirect.com/science/article/pii/S0888327016000066 (cit. on p. 28).

[61] N. M. M. Maia and J. M. M. e Silva. *Theoretical and Experimental Modal Analysis*. Baldock, England: Research Studies Press, 1997. ISBN: 978-0-863-80208-9 (cit. on p. 28).

[62] A. N. Iliopoulos, W. Weijtjens, D. V. Hemelrijck, and C. Devriendt. "Prediction of dynamic strains on a monopile offshore wind turbine using virtual sensors". In: *Journal of Physics: Conference Series* 628 (2015), p. 012108. DOI: 10.1088/1742-6596/628/1/012108 (cit. on p. 28).

[63] A. Iliopoulos, R. Shirzadeh, W. Weijtjens, P. Guillaume, D. V. Hemelrijck, and C. Devriendt. "A modal decomposition and expansion approach for prediction of dynamic responses on a monopile offshore wind turbine using a limited number of vibration sensors". In: *Mechanical Systems and Signal Processing* 68-69 (2016), pp. 84–104. ISSN: 0888-3270. DOI: 10.1016/j.ymssp.2015.07.016. URL: https://www.sciencedirect.com/science/article/pii/S0888327015003350 (cit. on p. 28).

[64] A. Urgueira, R. Almeida, and N. M. M. Maia. "Experimental estimation of FRFs using the transmissibility concept". In: *23rd International Conference on Noise and Vibration Engineering 2008, ISMA 2008* 3 (2008), pp. 1807–1814 (cit. on p. 29).

[65] N. M. M. Maia, A. Urgueira, and R. Almeida. "Whys and Wherefores of Transmissibility". In: 2011. ISBN: 978-953-307-433-7. DOI: 10.5772/24869 (cit. on p. 29).

[66] A. M. R. Ribeiro, J. M. M. Silva, and N. M. M. Maia. "On the generalisation of the transmissibility concept". In: *Mechanical Systems and Signal Processing* 14.1 (2000), pp. 29–35. DOI: 10.1006/mssp.1999.1268 (cit. on p. 29).

[67] Y. E. Lage, M. M. Neves, N. M. M. Maia, and D. Tcherniak. "Force transmissibility versus displacement transmissibility". In: *Journal of Sound and Vibration* 333.22 (2014), pp. 5708–5722. ISSN: 0022-460X. DOI: 10.1016/j.jsv.2014.05.038. URL: https://www.sciencedirect.com/science/article/pii/S0022460X14004477 (cit. on p. 31).

[68] A. S. A. Pereira. "Understanding and exploring virtual sensing and its capabilities for structural health monitoring". Master's Thesis. NOVA University of Lisbon, School of Science and Technology, 2021. URL: http://hdl.handle.net/10362/141378 (cit. on pp. 33, 34).

[69] J. N. Reddy. *Introduction to the Finite Element Method*. 4th Edition. McGraw-Hill Education, 2019. ISBN: 9781259861901 (cit. on p. 33).

[70] K. A. Kvåle. *knutankv/koma: Minor fixes*. Version v.1.0.7. 2022. DOI: 10.5281/zenodo.5881841. URL: https://github.com/knutankv/koma (cit. on p. 39).

[71] M. J. Whelan, M. V. Gangone, K. D. Janoyan, and R. Jha. "Real-time wireless vibration monitoring for operational modal analysis of an integral abutment highway bridge". In: *Engineering Structures* 31.10 (2009), pp. 2224–2235. ISSN: 0141-0296. DOI: 10.1016/j.engstruct.2009.03.022. URL: https://www.sciencedirect.com/science/article/pii/S0141029609001291 (cit. on p. 57).

[72] J. Li, T. Bao, and C. E. Ventura. "An automated operational modal analysis algorithm and its application to concrete dams". In: *Mechanical Systems and Signal Processing* 168 (2022), p. 108707. ISSN: 0888-3270. DOI: 10.1016/j.ymssp.2021.108707. URL: https://www.sciencedirect.com/science/article/pii/S088832702101027X (cit. on p. 57).

[73] Brüel & Kjær Sound & Vibration Measurement. *Product data: Piezoelectric accelerometer types 4507 and 4508*. Denmark, 2020. URL: https://www.bksv.com/-/media/literature/Product-Data/bp1841.ashx (cit. on p. 60).

[74] PCB Piezotronics. *Series 333: Accelerometers for modal testing*. NY, United States, 2021. URL: https://www.pcb.com/ContentStore/mktg/Downloads/TM-VIB-333_lowres.pdf (cit. on p. 60).

[75] Prosig. *Noise & Vibration Handbook*. United Kingdom, 2021. URL: https://prosig.com/download/noise-vibration-handbook/ (cit. on p. 60).

Numerical plots

A.1   Plots from real responses
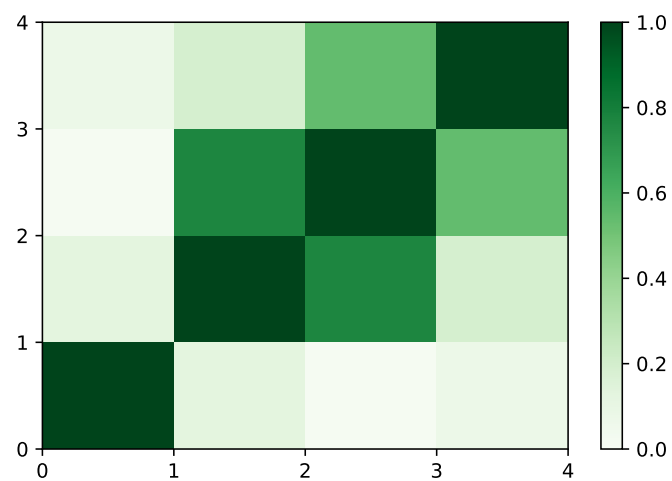
Figure A.1. MAC matrix obtained from the SSI-COV method for the undamaged observations of the numerical application, where real sensors are placed on the top of the beam and the damage is on the bottom.
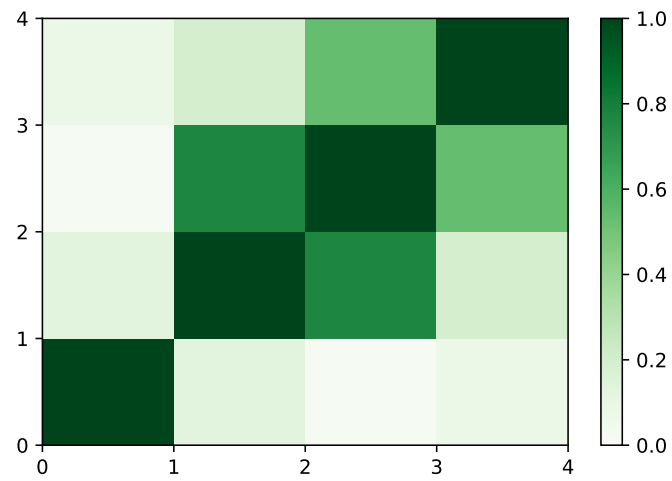
Figure A.2. MAC matrix obtained from the EFDD method for the undamaged observations of the numerical application, where real sensors are placed on the top of the beam and the damage is on the bottom.

(a) 1$^{\text{st}}$ Natural Frequency.

(b) 2$^{\text{nd}}$ Natural Frequency.

(c) 3$^{\text{rd}}$ Natural Frequency.
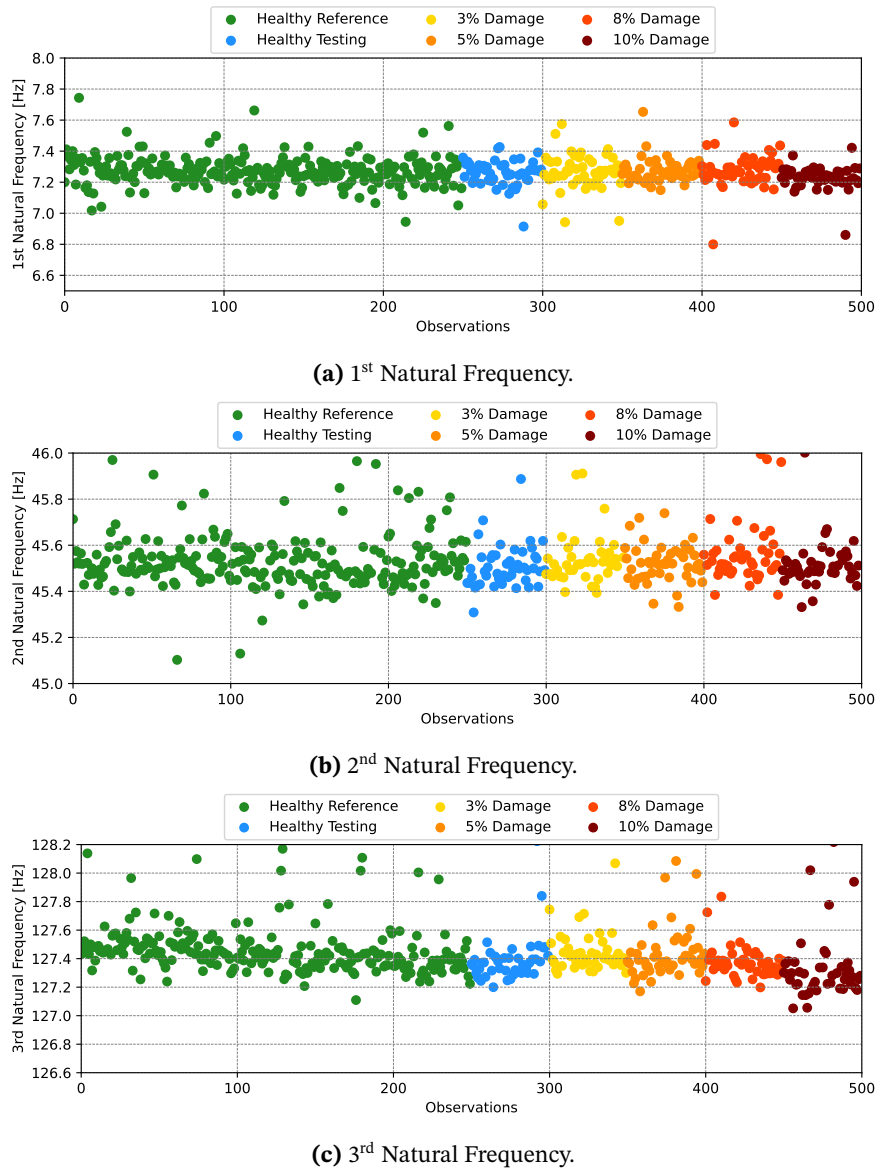
Figure A.3. First three Natural frequencies obtained using the SSI-COV method for all 500 observations (250 undamaged for healthy reference, 50 for healthy testing and 50 for each increasing damage percentage) of the numerical application, considering the real sensor placement on the top of the beam and damage on the bottom.
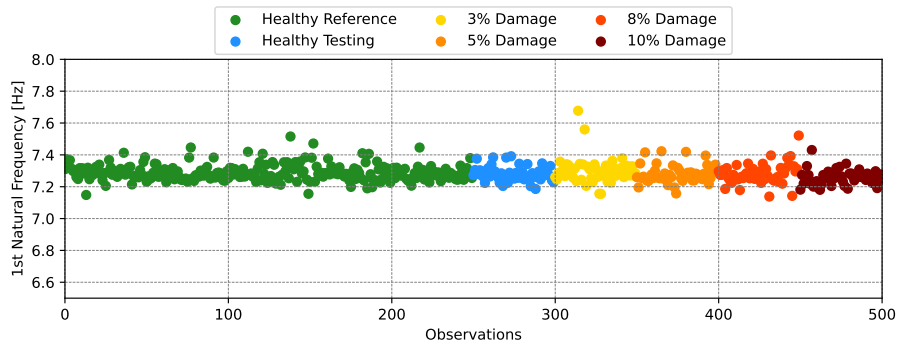
(a) 1st Natural Frequency.
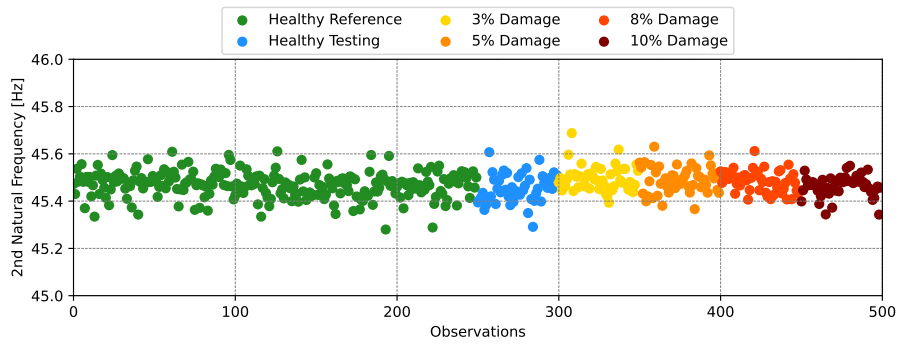
(b) 2nd Natural Frequency.
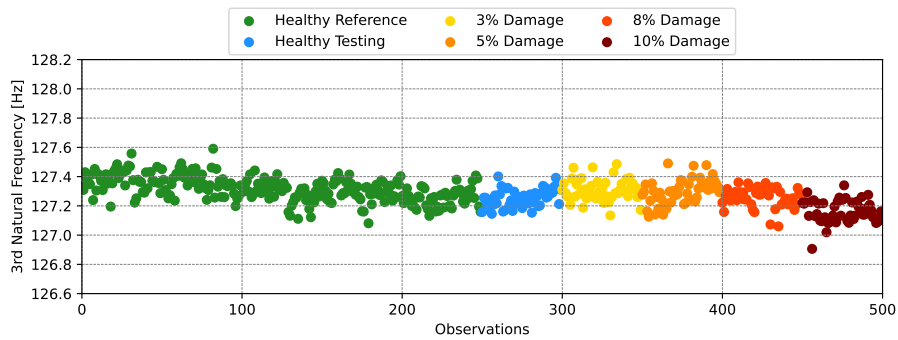
(c) 3rd Natural Frequency.

Figure A.4. First three Natural frequencies obtained using the EFDD method for all 500 observations (250 undamaged for healthy reference, 50 for healthy testing and 50 for each increasing damage percentage) of the numerical application, considering the real sensor placement on the top of the beam and damage on the bottom.

A.2 Plots from real and virtual responses
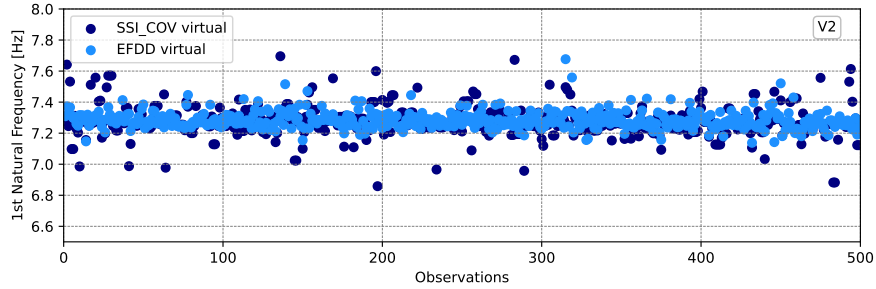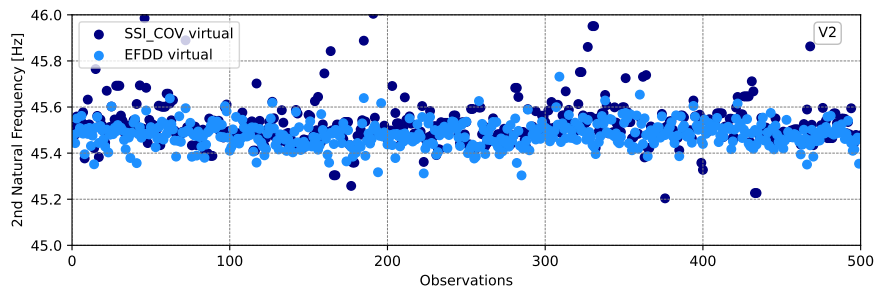
(a) 1st Natural Frequency for V2 – MDE.

(b) 2nd Natural Frequency for V2 – MDE.
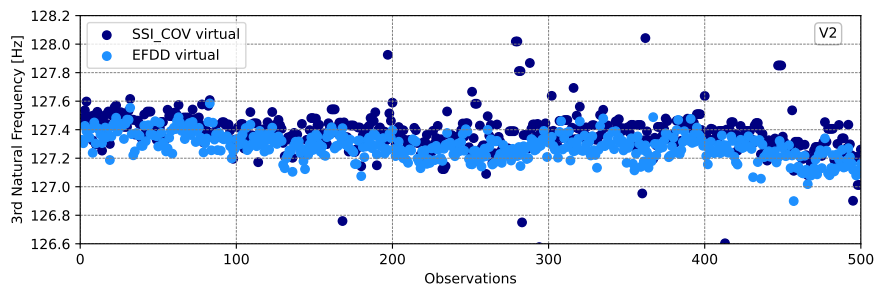
(c) 3rd Natural Frequency for V2 – MDE.
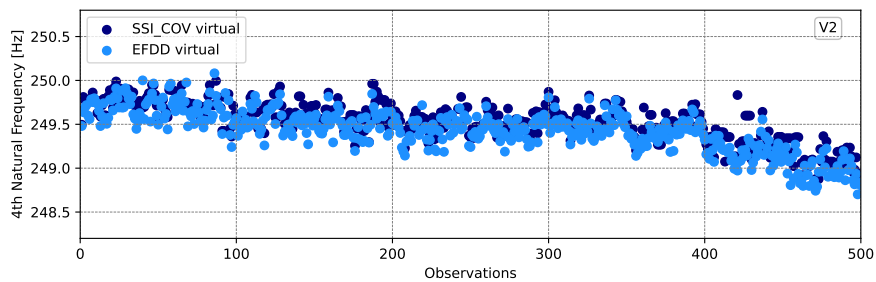
(d) 4th Natural Frequency for V2 – MDE.

Figure A.5. Comparison between each of the four first natural frequencies identified using SSI-COV and EFDD for all observations of the numerical application, for the case considering real sensors on top of the beam, virtual responses from MDE sensor V2 and damage on the bottom.
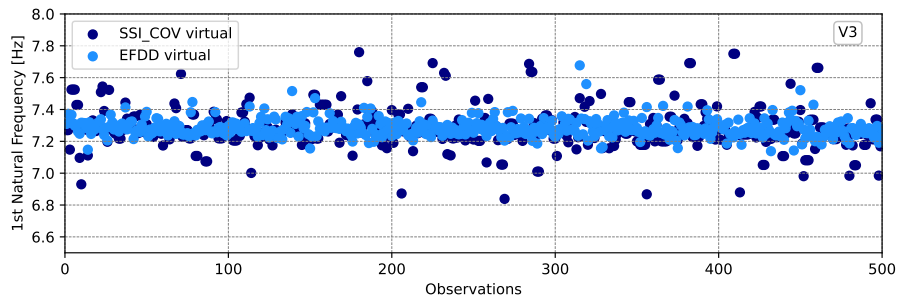
(a) 1st Natural Frequency for V3 – MDE.
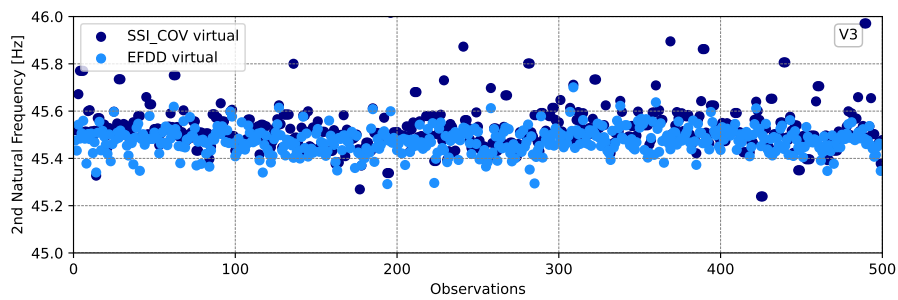
(b) 2nd Natural Frequency for V3 – MDE.
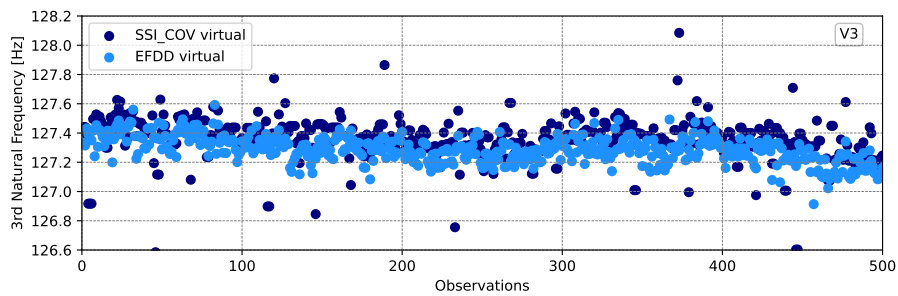
(c) 3rd Natural Frequency for V3 – MDE.
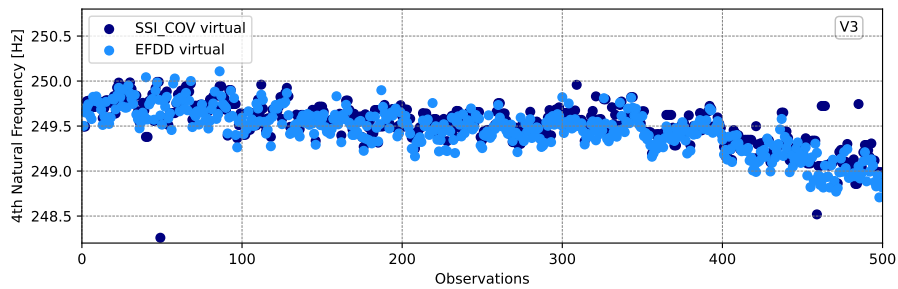
(d) 4th Natural Frequency for V3 – MDE.

Figure A.6. Comparison between each of the four first natural frequencies identified using SSI-COV and EFDD for all observations of the numerical application, for the case considering real sensors on top of the beam, virtual responses from MDE sensor V3 and damage on the bottom.
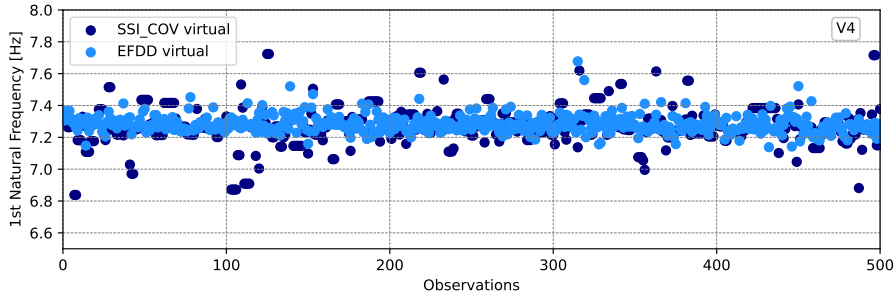
(a) 1st Natural Frequency for V4 – MDE.
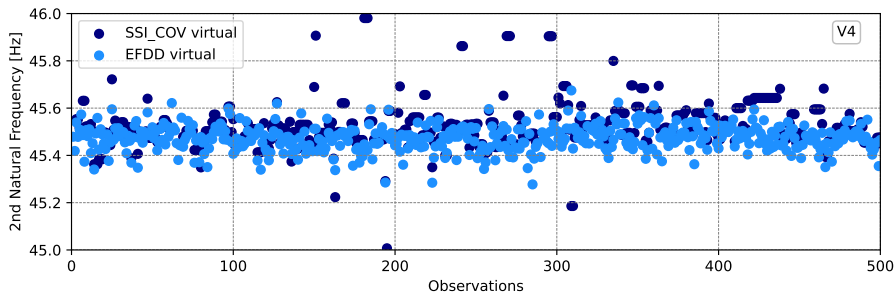
(b) 2nd Natural Frequency for V4 – MDE.
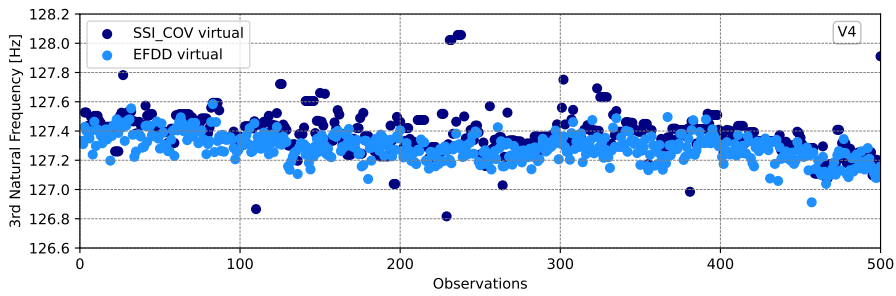
(c) 3rd Natural Frequency for V4 – MDE.
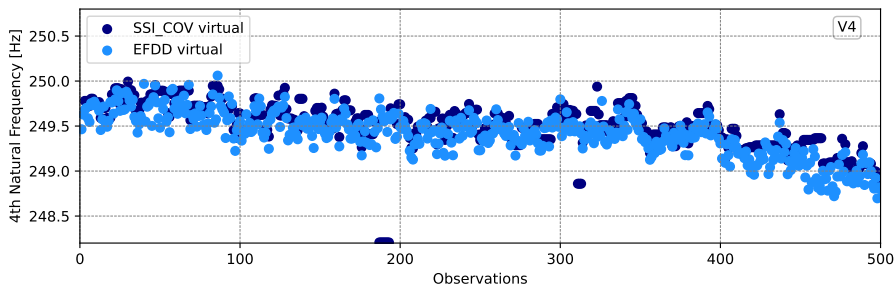
(d) 4th Natural Frequency for V4 – MDE.

Figure A.7. Comparison between each of the four first natural frequencies identified using SSI-COV and EFDD for all observations of the numerical application, for the case considering real sensors on top of the beam, virtual responses from MDE sensor V4 and damage on the bottom.
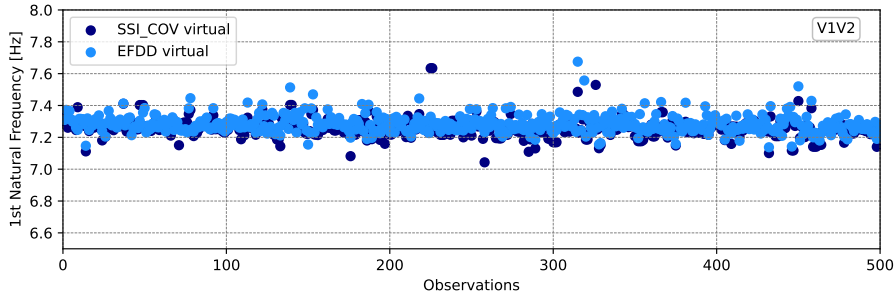
(a) 1st Natural Frequency for V1V2 – MDE.
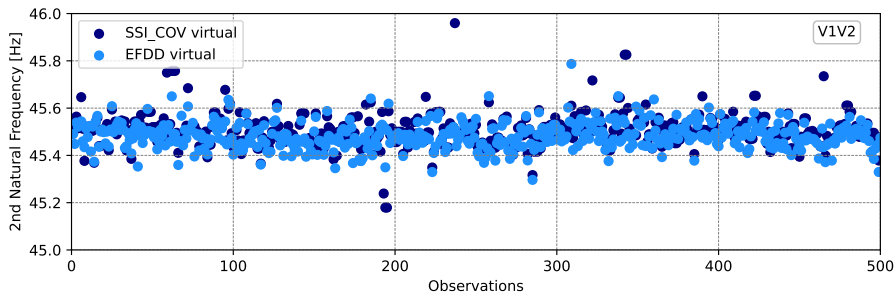
(b) 2nd Natural Frequency for V1V2 – MDE.
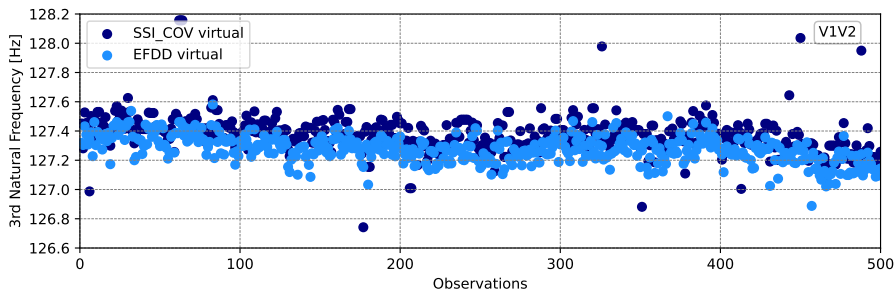
(c) 3rd Natural Frequency for V1V2 – MDE.
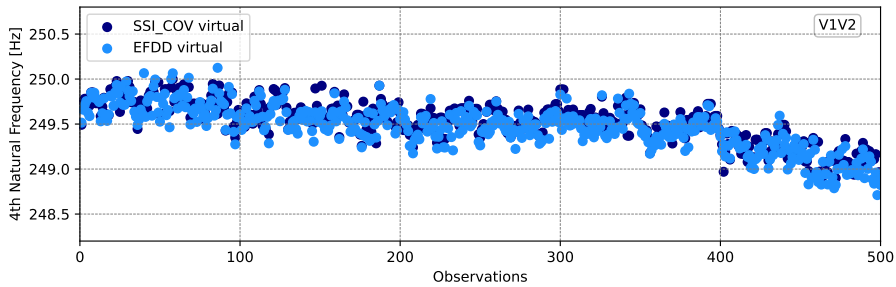
(d) 4th Natural Frequency for V1V2 – MDE.

Figure A.8. Comparison between each of the four first natural frequencies identified using SSI-COV and EFDD for all observations of the numerical application, for the case considering real sensors on top of the beam, virtual responses from MDE sensors V1V2 and damage on the bottom.
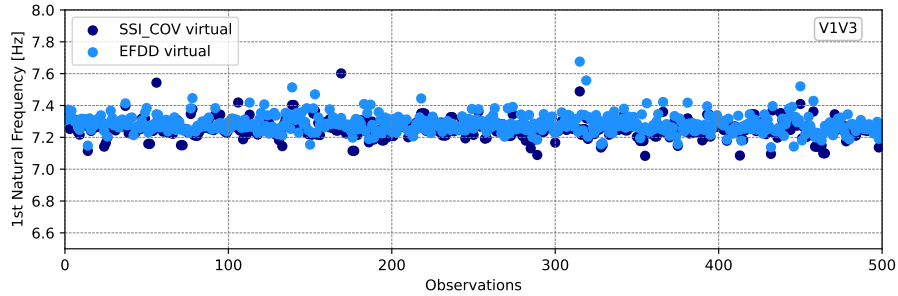
(a) 1st Natural Frequency for V1V3 – MDE.
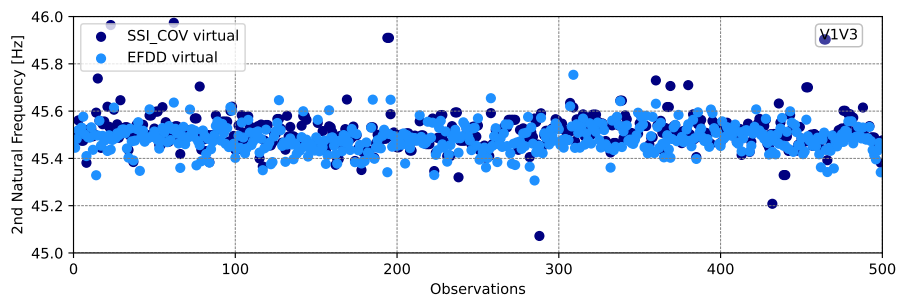
(b) 2nd Natural Frequency for V1V3 – MDE.
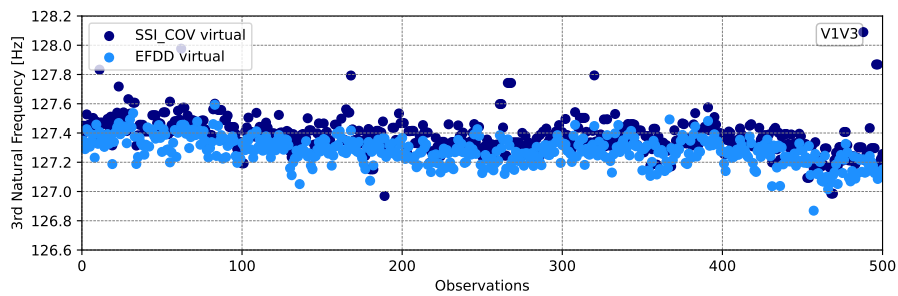
(c) 3rd Natural Frequency for V1V3 – MDE.
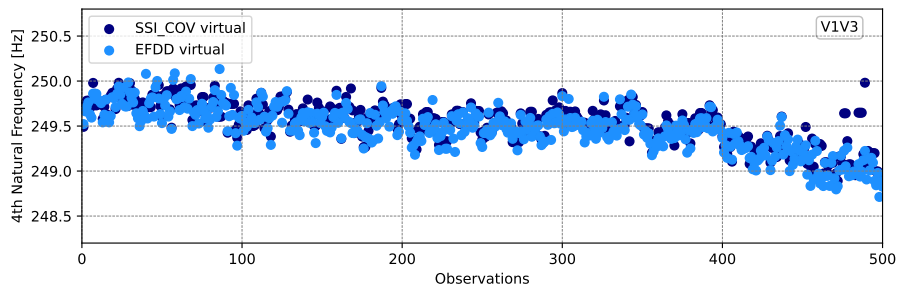
(d) 4th Natural Frequency for V1V3 – MDE.

Figure A.9. Comparison between each of the four first natural frequencies identified using SSI-COV and EFDD for all observations of the numerical application, for the case considering real sensors on top of the beam, virtual responses from MDE sensors V1V3 and damage on the bottom.
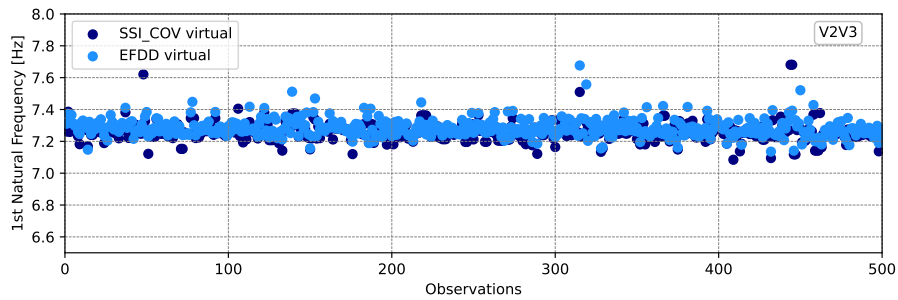
(a) 1st Natural Frequency for V2V3 – MDE.
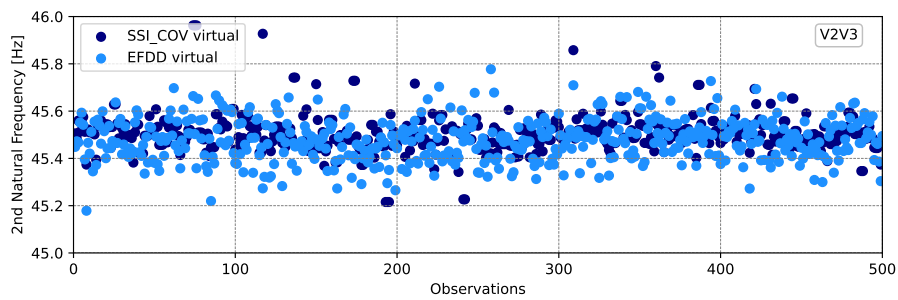
(b) 2nd Natural Frequency for V2V3 – MDE.
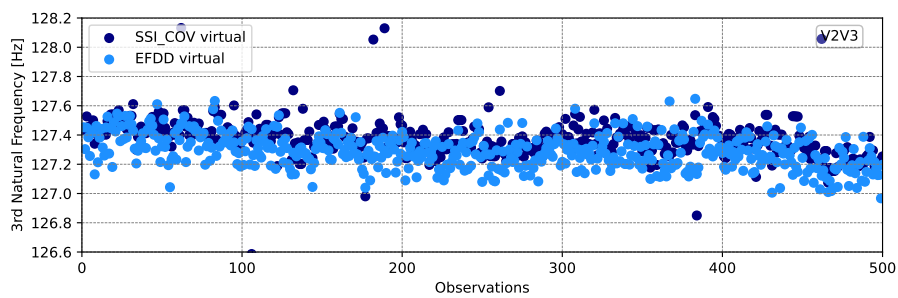
(c) 3rd Natural Frequency for V2V3 – MDE.
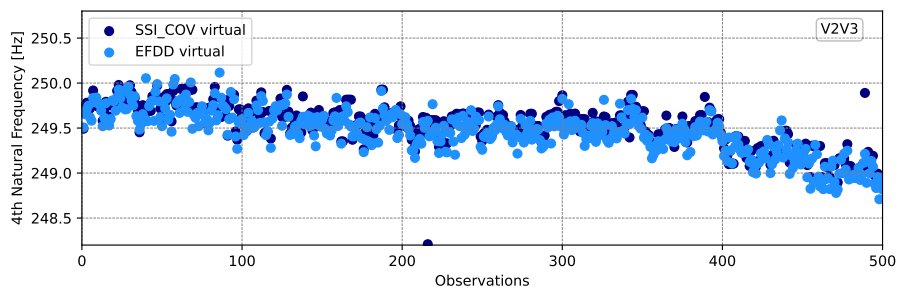
(d) 4th Natural Frequency for V2V3 – MDE.

Figure A.10. Comparison between each of the four first natural frequencies identified using SSI-COV and EFDD for all observations of the numerical application, for the case considering real sensors on top of the beam, virtual responses from MDE sensors V2V3 and damage on the bottom.
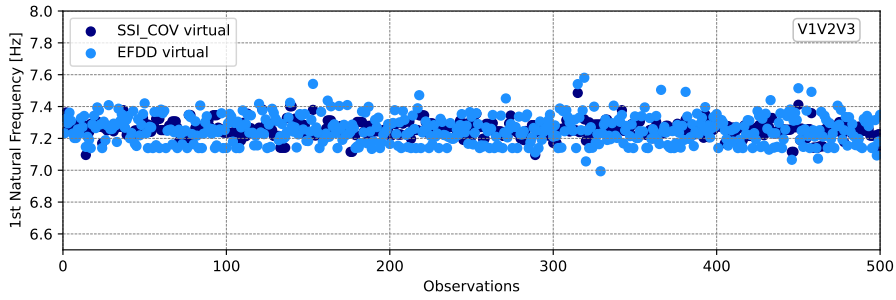
(a) 1st Natural Frequency for V1V2V3 – MDE.
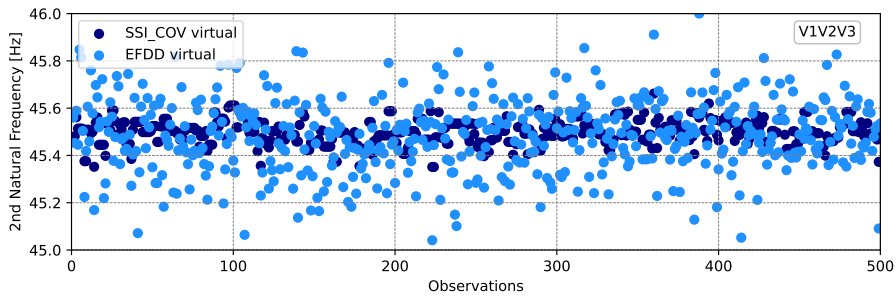
(b) 2nd Natural Frequency for V1V2V3 – MDE.
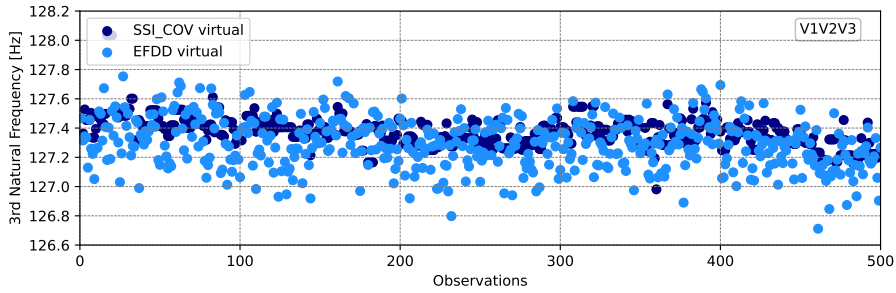
(c) 3rd Natural Frequency for V1V2V3 – MDE.
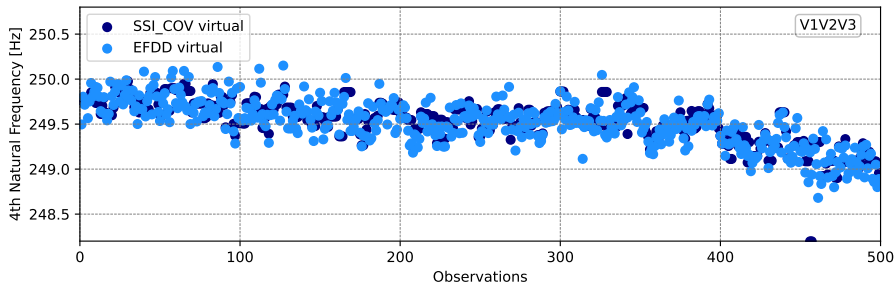
(d) 4th Natural Frequency for V1V2V3 – MDE.

Figure A.11. Comparison between each of the four first natural frequencies identified using SSI-COV and EFDD for all observations of the numerical application, for the case considering real sensors on top of the beam, virtual responses from MDE sensors V1V2V3 and damage on the bottom.
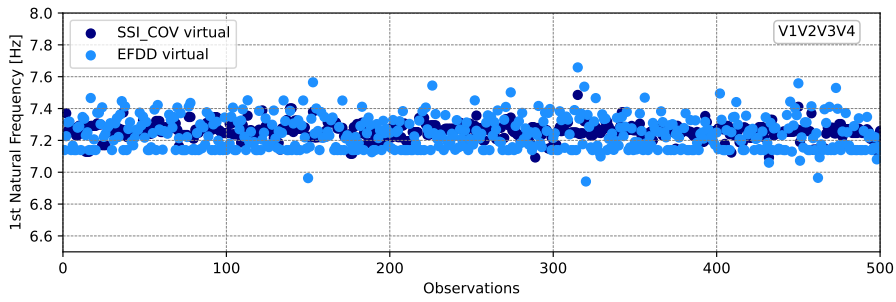
(a) 1st Natural Frequency for V1V2V3V4 – MDE.
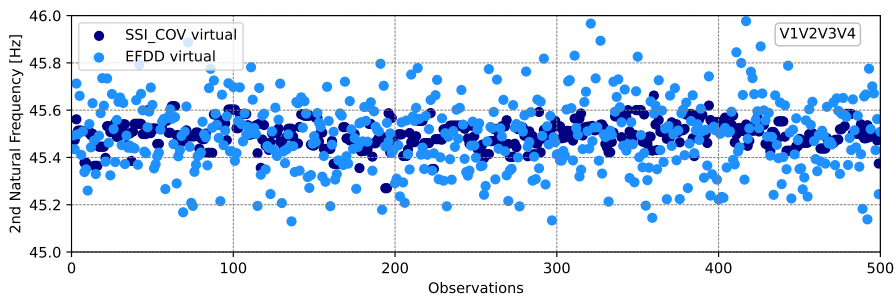
(b) 2nd Natural Frequency for V1V2V3V4 – MDE.
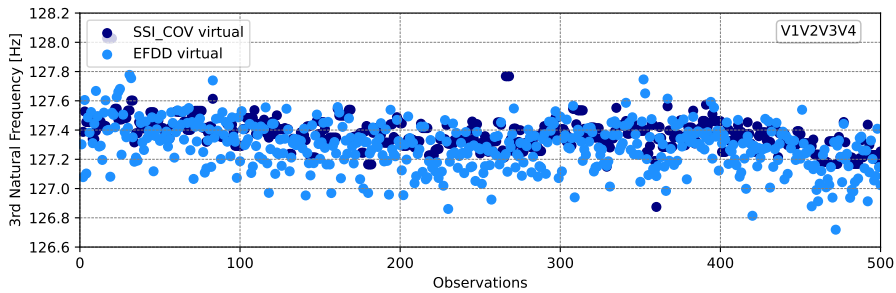
(c) 3rd Natural Frequency for V1V2V3V4 – MDE.
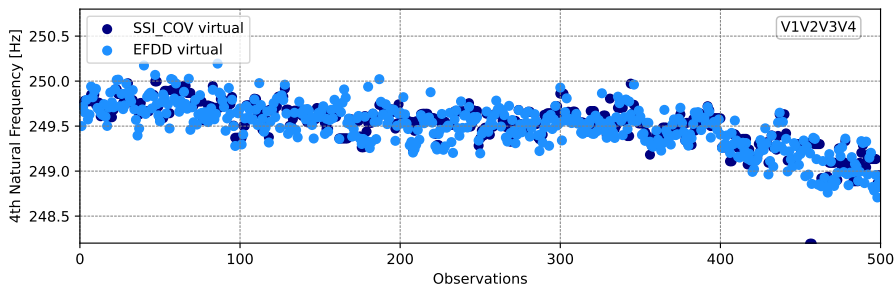
(d) 4th Natural Frequency for V1V2V3V4 – MDE.

Figure A.12. Comparison between each of the four first natural frequencies identified using SSI-COV and EFDD for all observations of the numerical application, for the case considering real sensors on top of the beam, virtual responses from MDE sensors V1V2V3V4 and damage on the bottom.

(a) MD for V2 from SSI-COV – MDE.

(b) MD for V2 from EFDD – MDE.
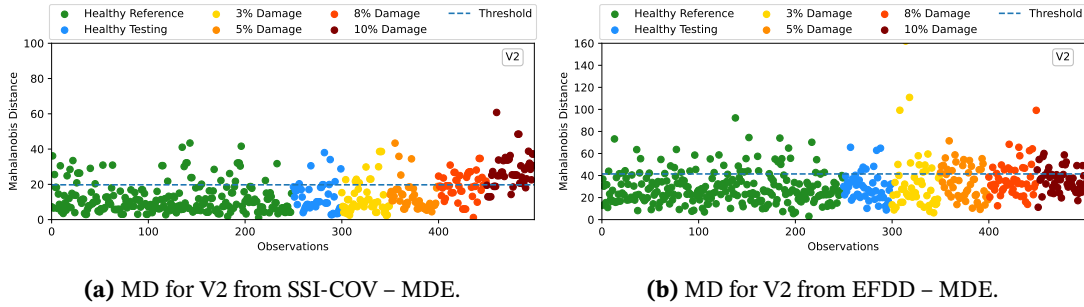
Figure A.13. Mahalanobis Distances obtained from the SSI-COV and the EFDD methods for all observations of the numerical application, considering the case where real sensors are placed on the top of the beam, virtual responses from MDE sensor V2 are added and damage is on the bottom.

(a) MD for V3 from SSI-COV – MDE.

(b) MD for V3 from EFDD – MDE.
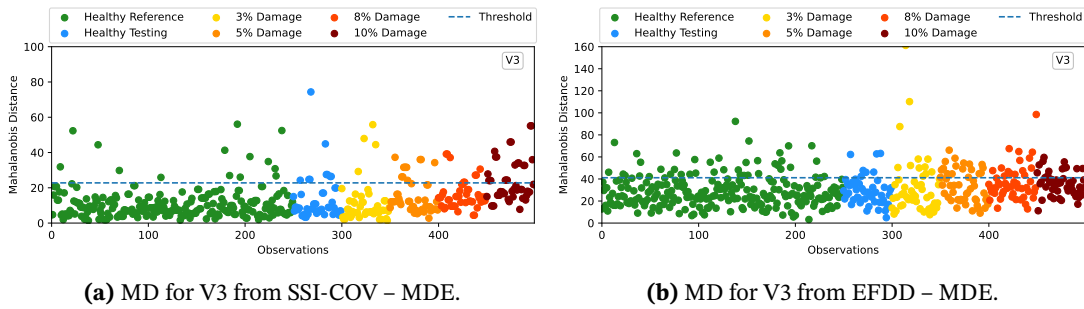
Figure A.14. Mahalanobis Distances obtained from the SSI-COV and the EFDD methods for all observations of the numerical application, considering the case where real sensors are placed on the top of the beam, virtual responses from MDE sensor V3 are added and damage is on the bottom.

(a) MD for V4 from SSI-COV – MDE.

(b) MD for V4 from EFDD – MDE.
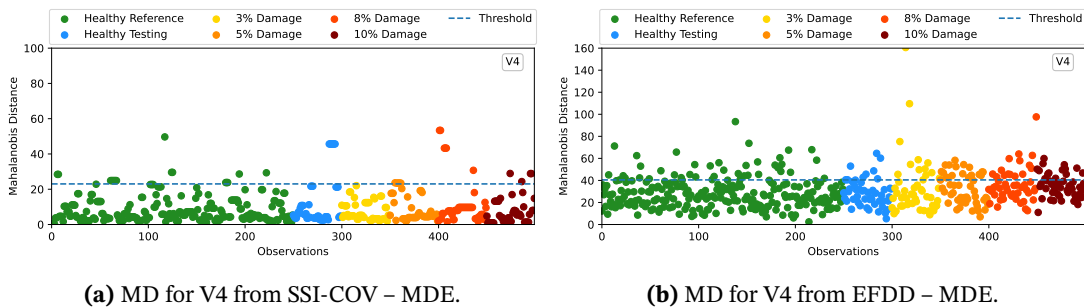
Figure A.15. Mahalanobis Distances obtained from the SSI-COV and the EFDD methods for all observations of the numerical application, considering the case where real sensors are placed on the top of the beam, virtual responses from MDE sensor V4 are added and damage is on the bottom.
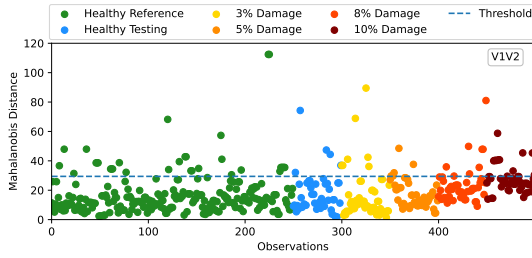
(a) MD for V1V2 from SSI-COV – MDE.
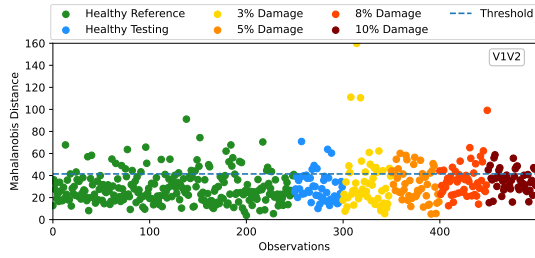
(b) MD for V1V2 from EFDD – MDE.

Figure A.16. Mahalanobis Distances obtained from the SSI-COV and the EFDD methods for all observations of the numerical application, considering the case where real sensors are placed on the top of the beam, virtual responses from MDE sensors V1V2 are added and damage is on the bottom.
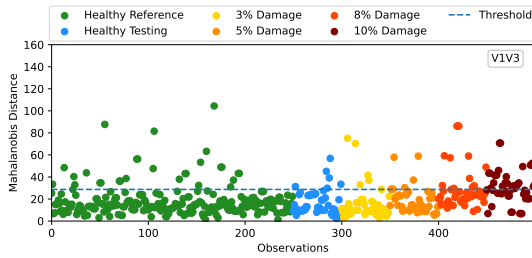
(a) MD for V1V3 from SSI-COV – MDE.
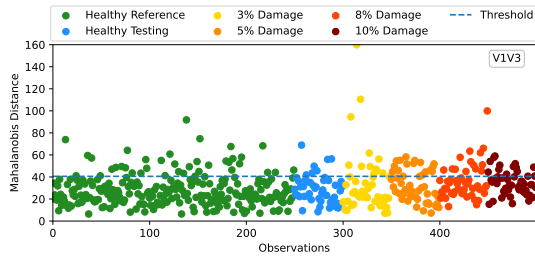
(b) MD for V1V3 from EFDD – MDE.

Figure A.17. Mahalanobis Distances obtained from the SSI-COV and the EFDD methods for all observations of the numerical application, considering the case where real sensors are placed on the top of the beam, virtual responses from MDE sensors V1V3 are added and damage is on the bottom.
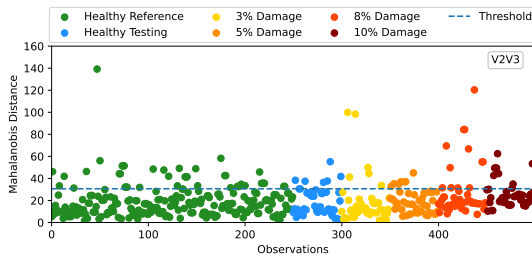
(a) MD for V2V3 from SSI-COV – MDE.
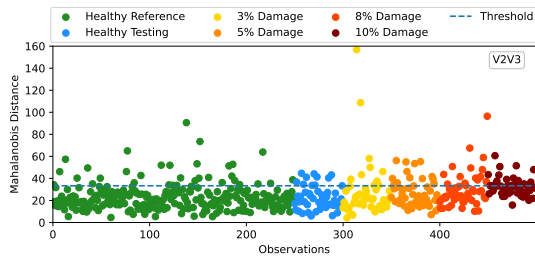
(b) MD for V2V3 from EFDD – MDE.

Figure A.18. Mahalanobis Distances obtained from the SSI-COV and the EFDD methods for all observations of the numerical application, considering the case where real sensors are placed on the top of the beam, virtual responses from MDE sensors V2V3 are added and damage is on the bottom.

(a) MD for V1V2V3 from SSI-COV – MDE.

(b) MD for V1V2V3 from EFDD – MDE.
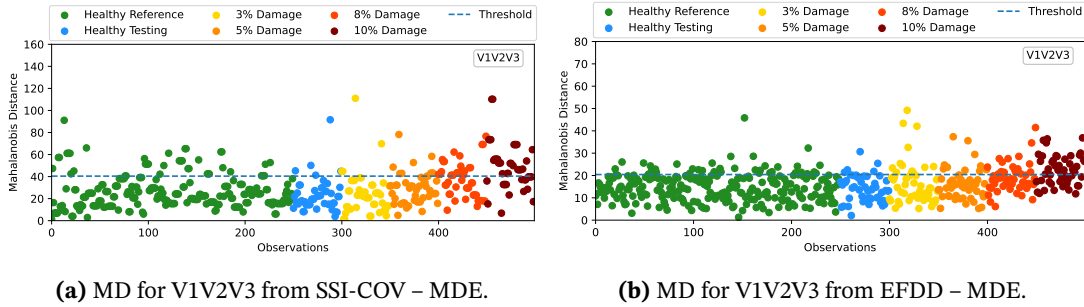
Figure A.19. Mahalanobis Distances obtained from the SSI-COV and the EFDD methods for all observations of the numerical application, considering the case where real sensors are placed on the top of the beam, virtual responses from MDE sensors V1V2V3 are added and damage is on the bottom.

(a) MD for V1V2V3V4 from SSI-COV – MDE.

(b) MD for V1V2V3V4 from EFDD – MDE.
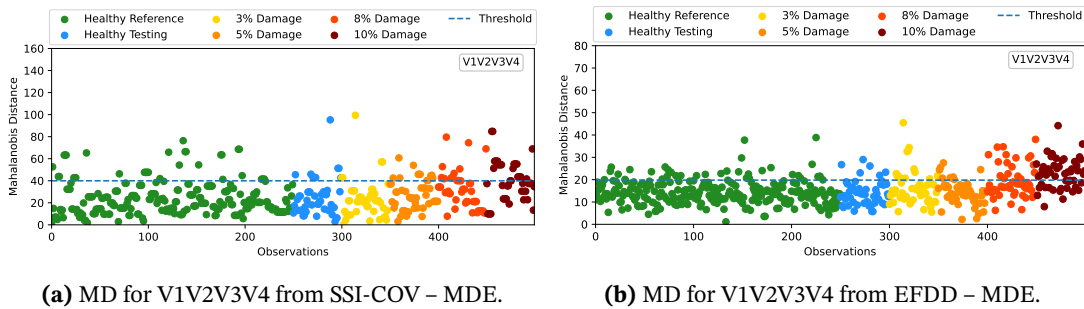
Figure A.20. Mahalanobis Distances obtained from the SSI-COV and the EFDD methods for all observations of the numerical application, considering the case where real sensors are placed on the top of the beam, virtual responses from MDE sensors V1V2V3V4 are added and damage is on the bottom.
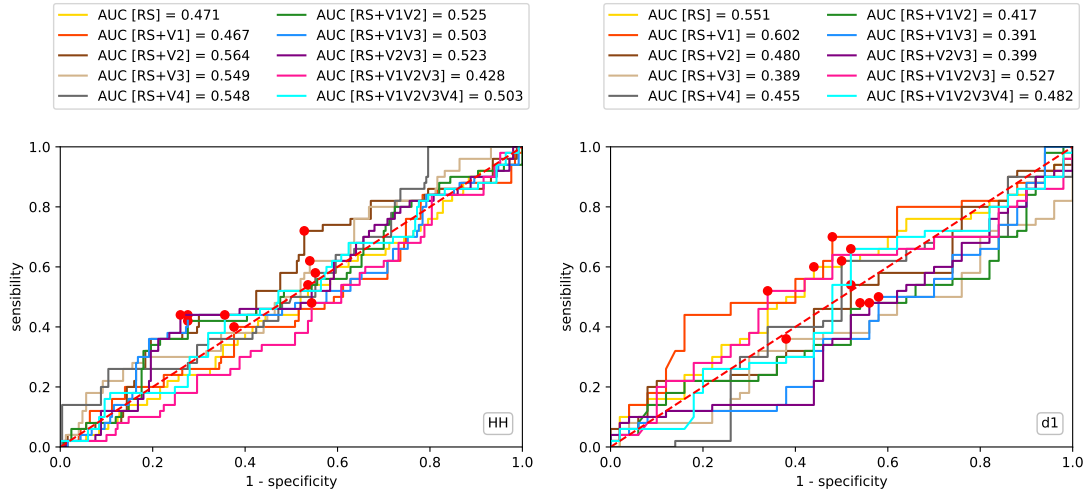
(a) AUC for undamaged observations from SSI-COV – MDE.

(b) AUC for the first damage level from SSI-COV – MDE.
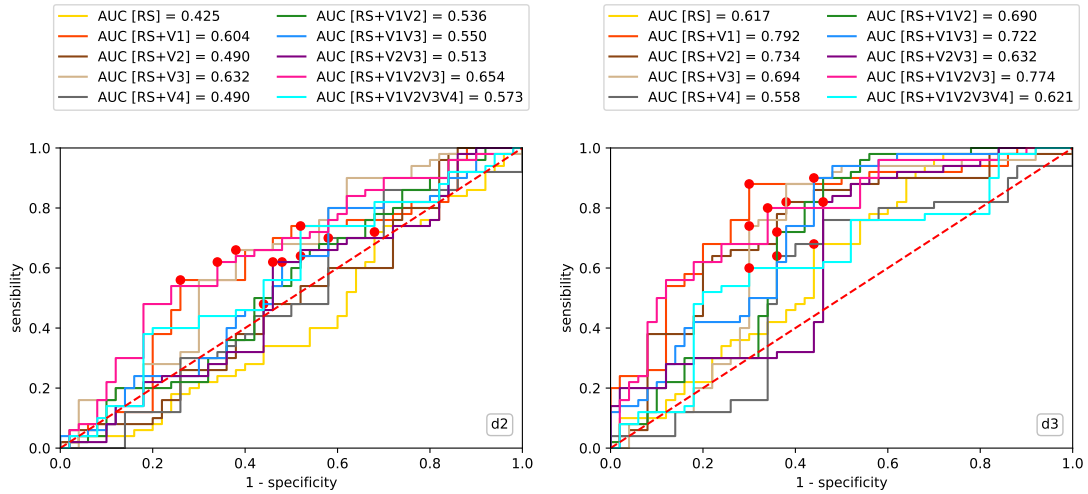
(c) AUC for the second damage level from SSI-COV – MDE.

(d) AUC for the third damage level from SSI-COV – MDE.

Figure A.21. Areas Under the Receiver Operating Curves obtained from the SSI-COV method for all observations and all virtual sensor combinations (undamaged and the three first damage levels applied), considering the numerical application, the case where real sensors are placed on the top of the beam, virtual sensors from MDE and damage on the bottom.

102

(a) AUC for undamaged observations from EFDD – MDE.

(b) AUC for the first damage level from EFDD – MDE.

(c) AUC for the second damage level from EFDD – MDE.

(d) AUC for the third damage level from EFDD – MDE.
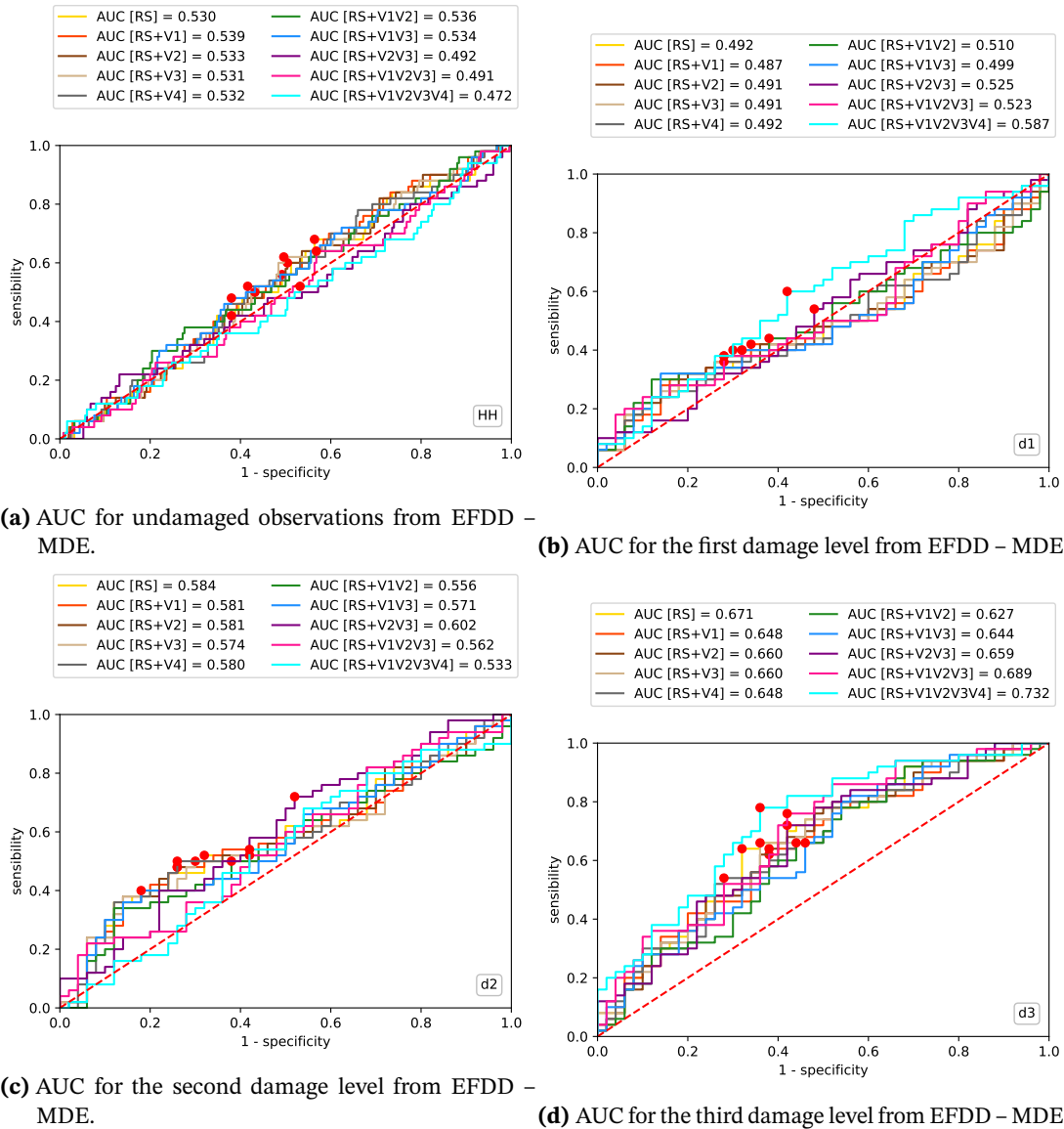
Figure A.22. Areas Under the Receiver Operating Curves obtained from the EFDD method for all observations and all virtual sensor combinations (undamaged and the three first damage levels applied), considering the numerical application, the case where real sensors are placed on the top of the beam, virtual sensors from MDE and damage on the bottom.

103

Experimental plots

B.1 Plots from real responses
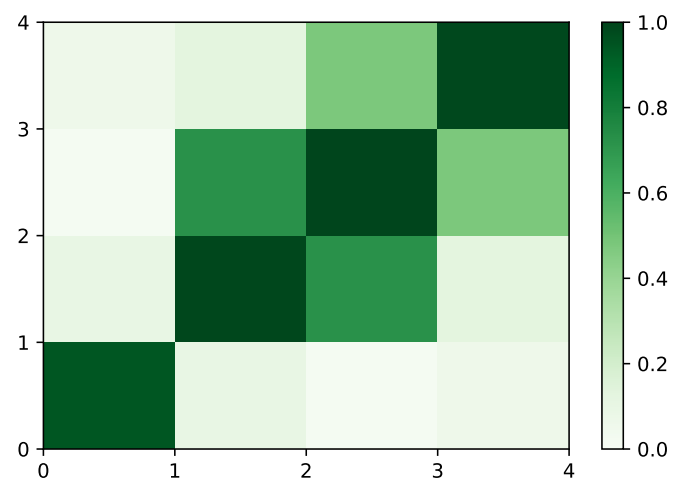
Figure B.1. MAC matrix obtained from the SSI-COV method for the undamaged observations of the experimental application, where real sensors are placed on the top of the beam and the damage is on the bottom.
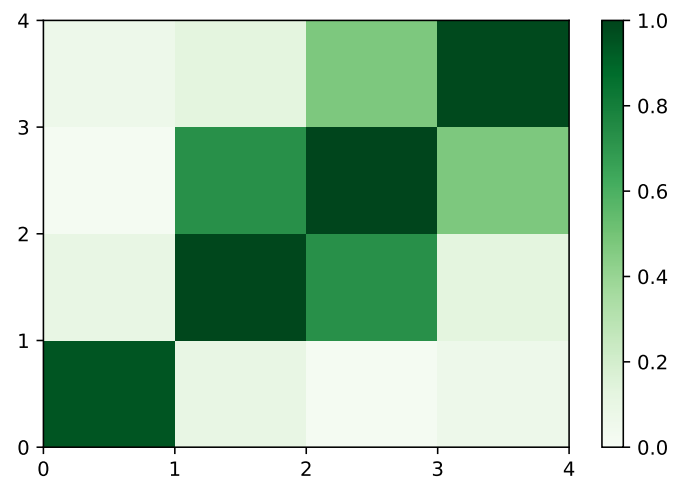
Figure B.2. MAC matrix obtained from the EFDD method for the undamaged obser-
vations of the experimental application, where real sensors are placed
on the top of the beam and the damage is on the bottom.
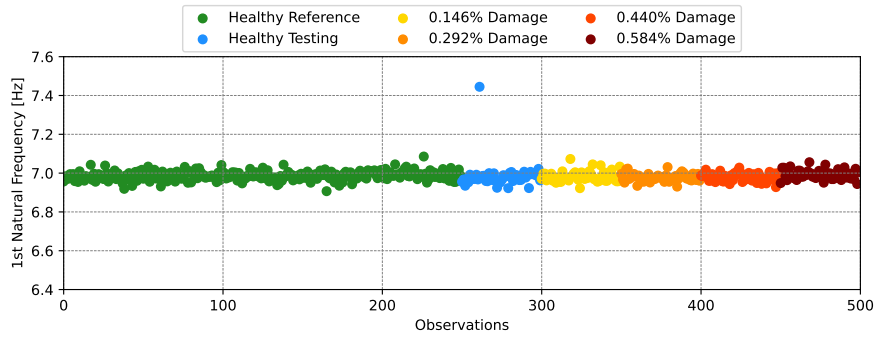
(a) 1st Natural Frequency.
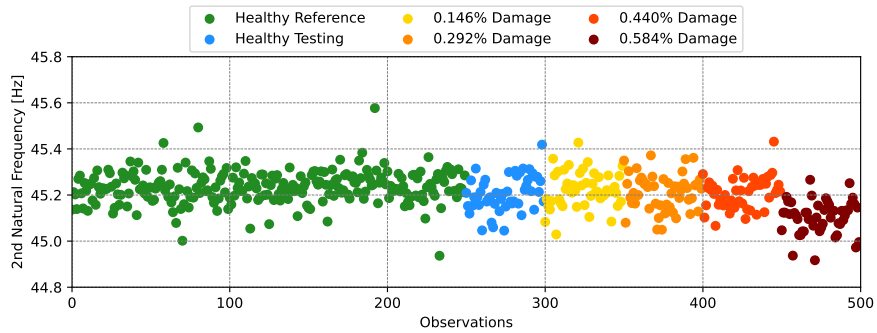
(b) 2nd Natural Frequency.
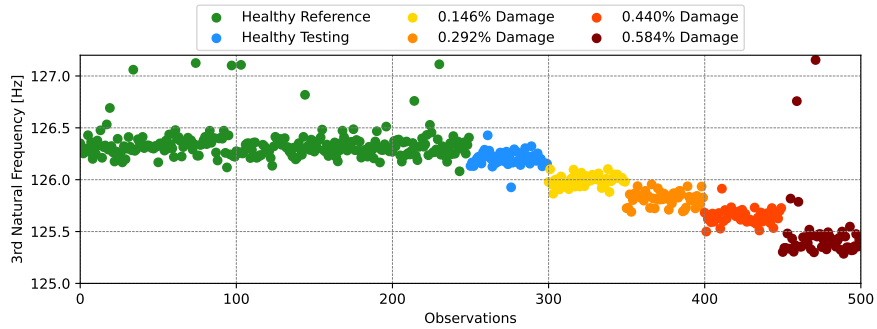
(c) 3rd Natural Frequency.
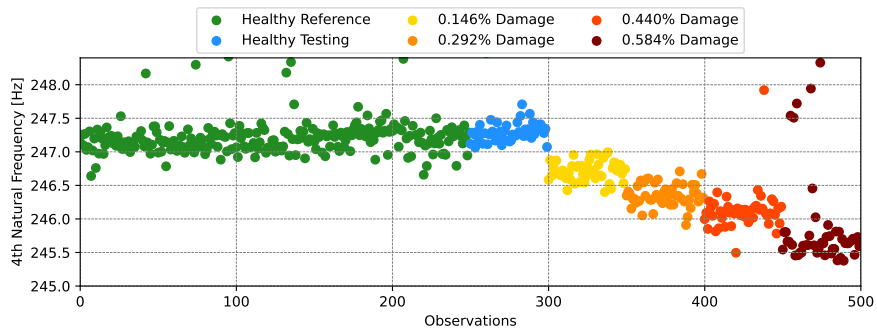
(d) 4th Natural Frequency.

Figure B.3. Natural frequencies obtained using the SSI-COV method for all 500 observations (250 undamaged for healthy reference, 50 for healthy testing and 50 for each increasing damage percentage) of the experimental application, considering the real sensor placement on the top of the beam and damage on the bottom.
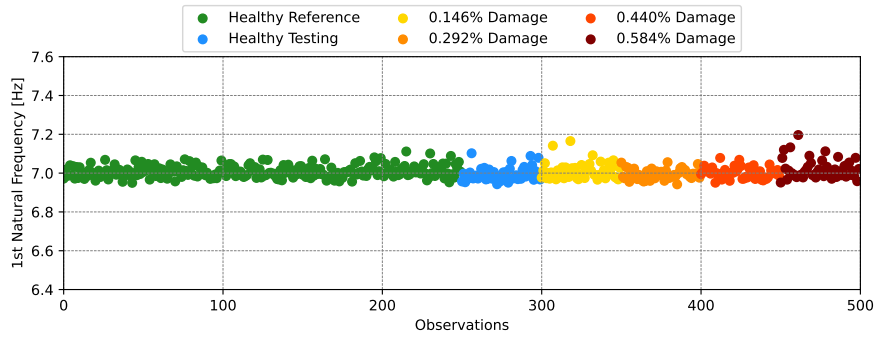
(a) 1ˢᵗ Natural Frequency.
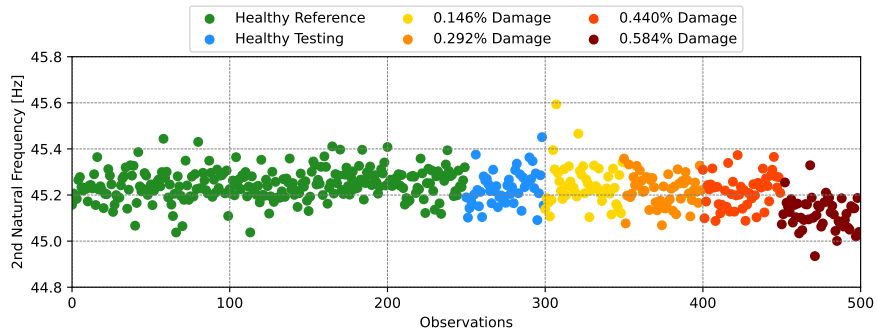
(b) 2ⁿᵈ Natural Frequency.
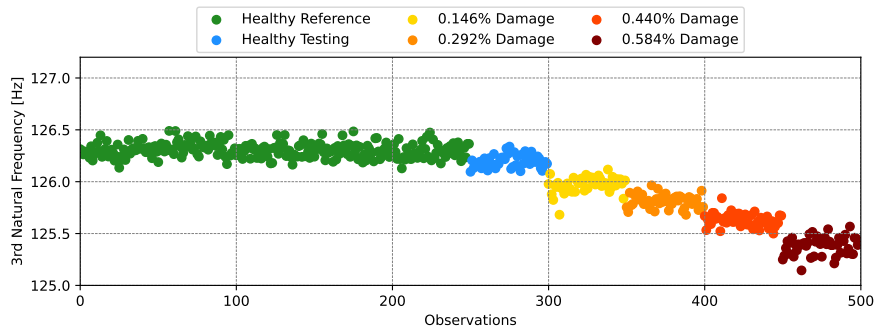
(c) 3ʳᵈ Natural Frequency.
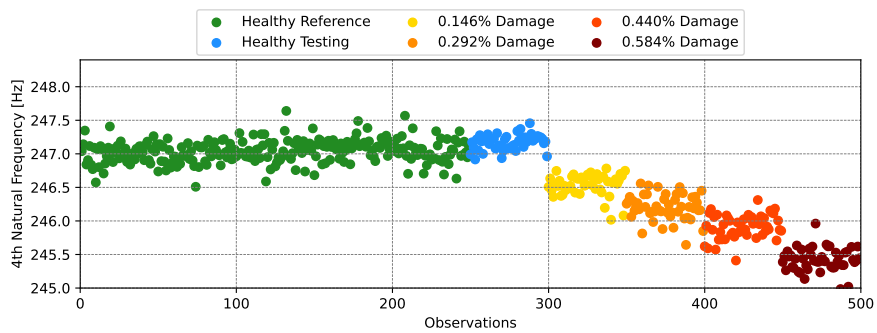
(d) 4ᵗʰ Natural Frequency.

Figure B.4. Natural frequencies obtained using the EFDD method for all 500 observations (250 undamaged for healthy reference, 50 for healthy testing and 50 for each increasing damage percentage) of the numerical application, considering the real sensor placement on the top of the beam and damage on the bottom.

B.2 Plots from real and virtual responses
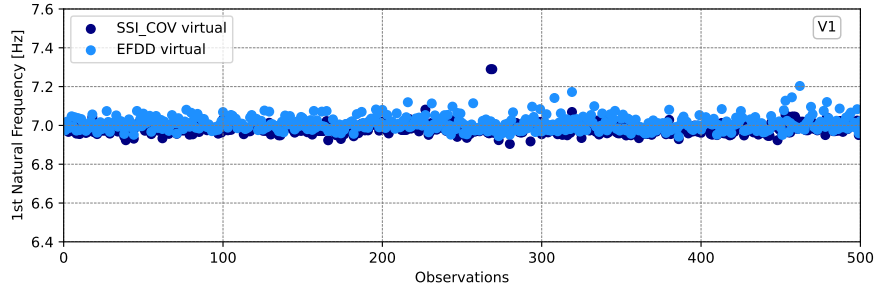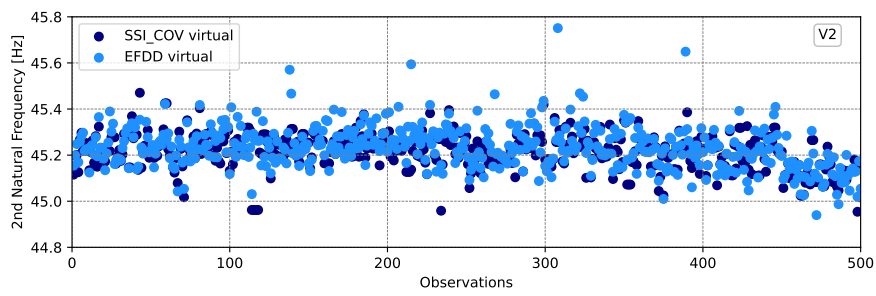
(a) 1st Natural Frequency for V1 – MDE.

(b) 2nd Natural Frequency for V1 – MDE.
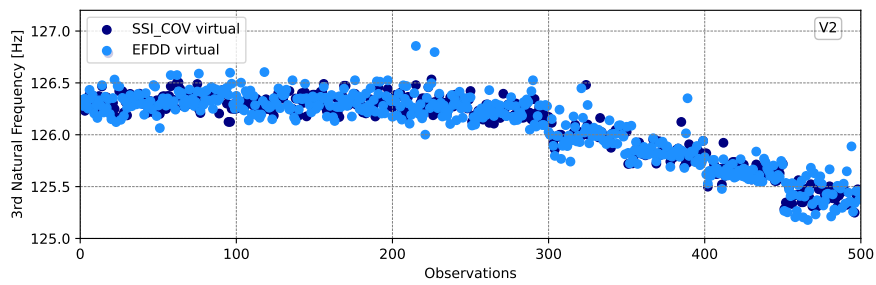
(c) 3rd Natural Frequency for V1 – MDE.
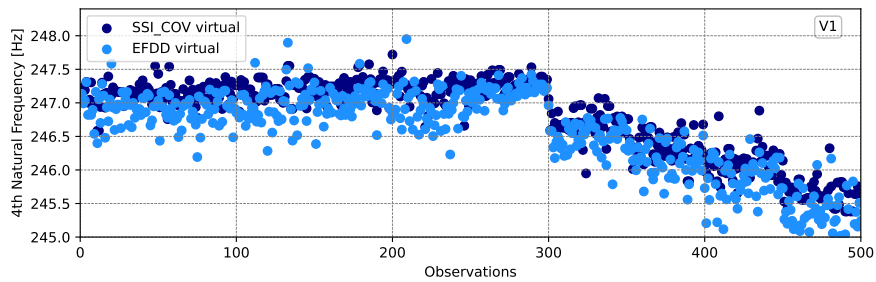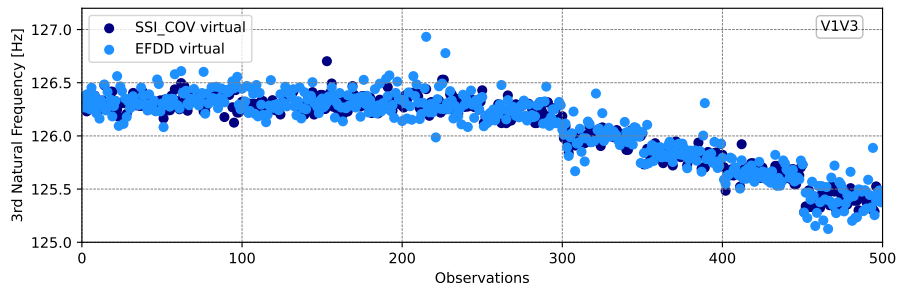

(d) 4th Natural Frequency for V1 – MDE.

Figure B.5. Comparison between each of the four first natural frequencies identified using SSI-COV and EFDD for all observations of the experimental application, for the case considering real sensors on top of the beam, virtual responses from MDE sensor V1 and damage on the bottom.
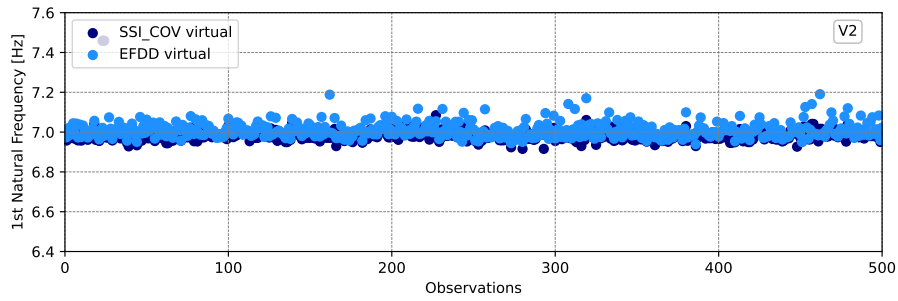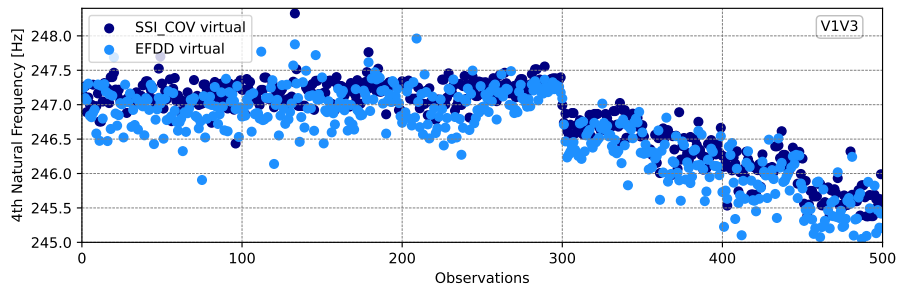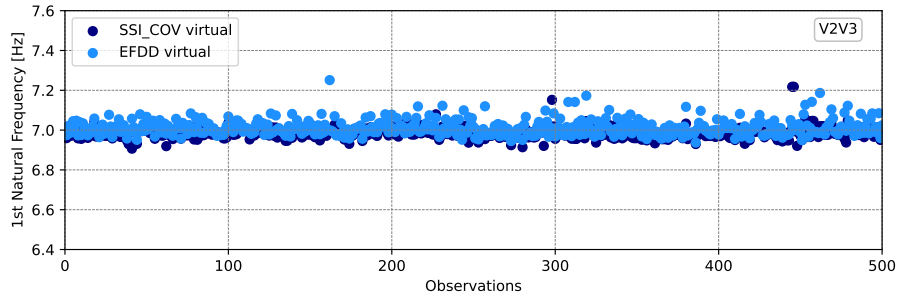
(a) 1st Natural Frequency for V2 – MDE.
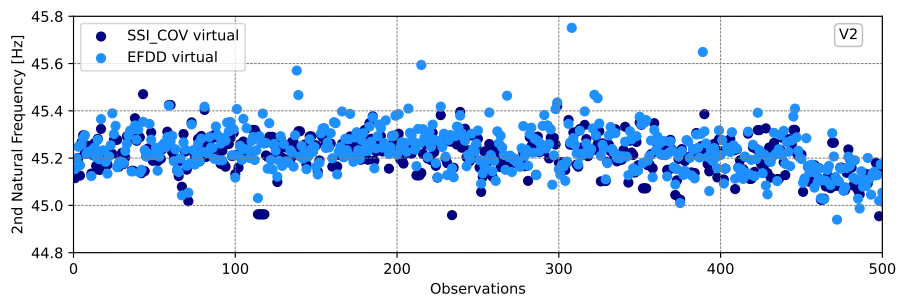
(b) 2nd Natural Frequency for V2 – MDE.
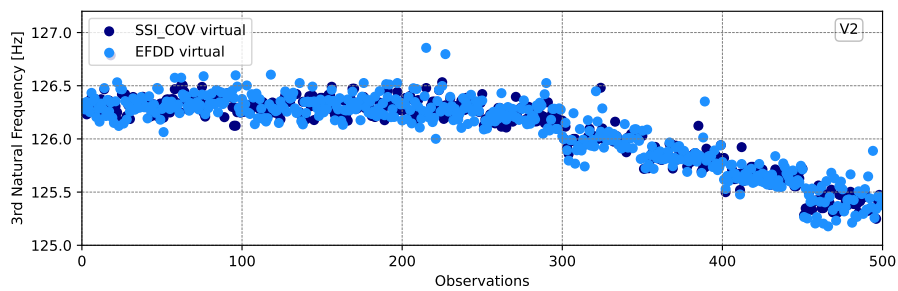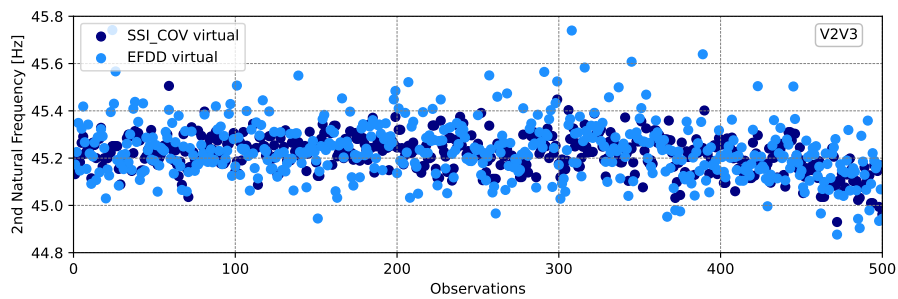

(c) 3rd Natural Frequency for V2 – MDE.
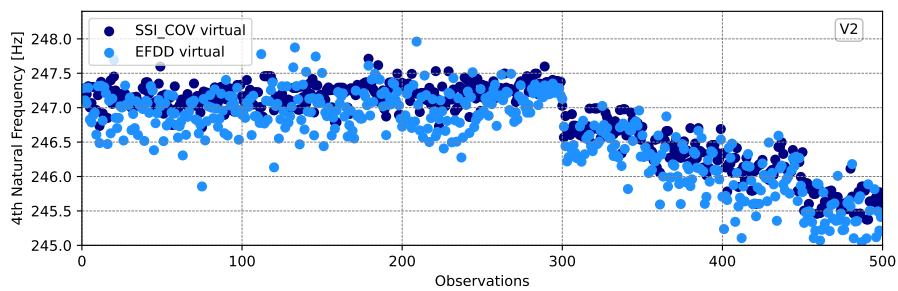
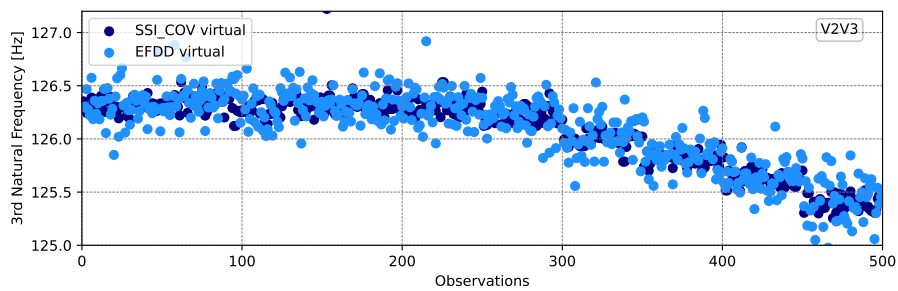**(d)** 4th Natural Frequency for V2 – MDE.

Figure B.6. Comparison between each of the four first natural frequencies identified using SSI-COV and EFDD for all observations of the experimental application, for the case considering real sensors on top of the beam, virtual responses from MDE sensor V2 and damage on the bottom.
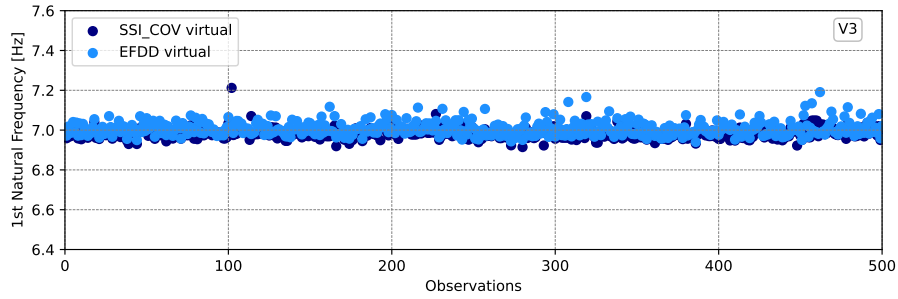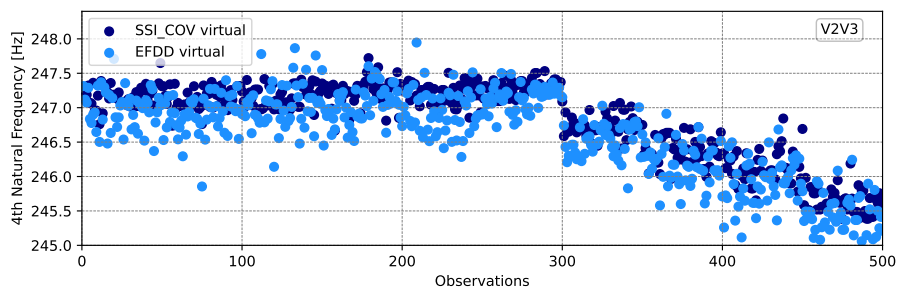
(a) 1st Natural Frequency for V3 – MDE.
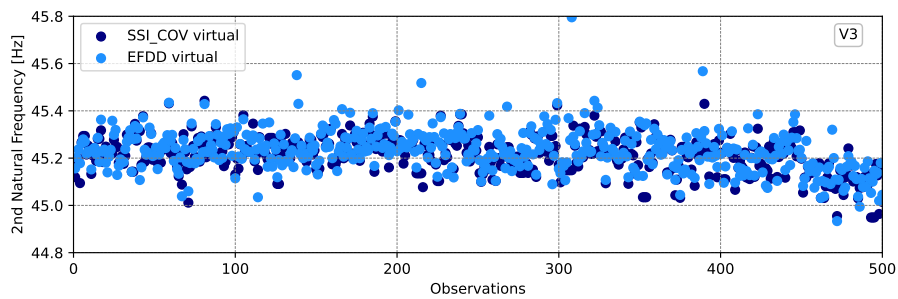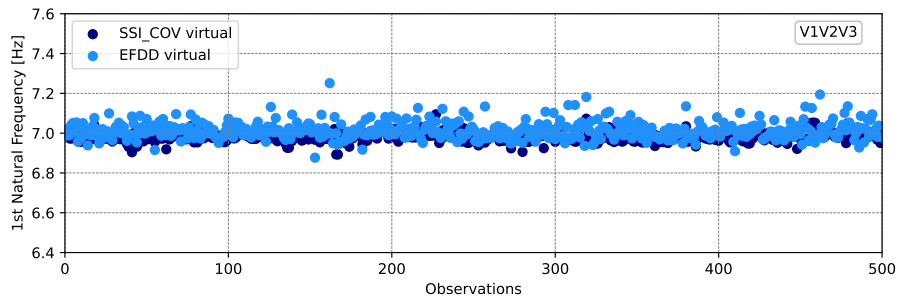

(b) 2nd Natural Frequency for V3 – MDE.
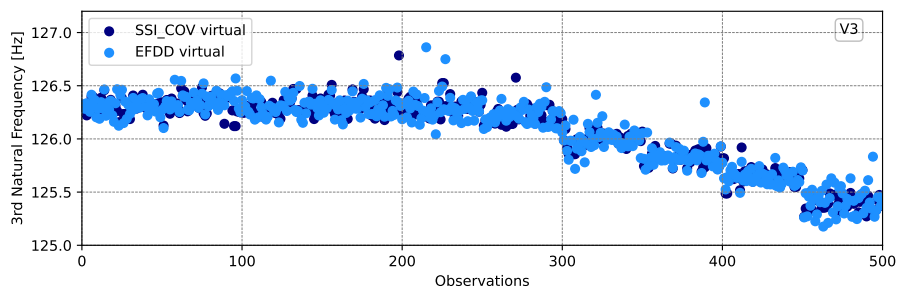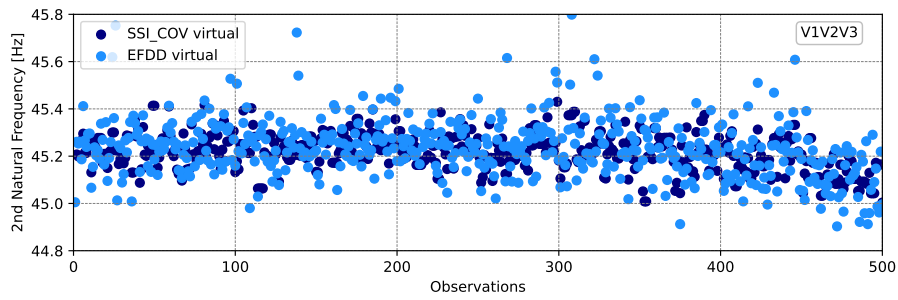

(c) 3rd Natural Frequency for V3 – MDE.
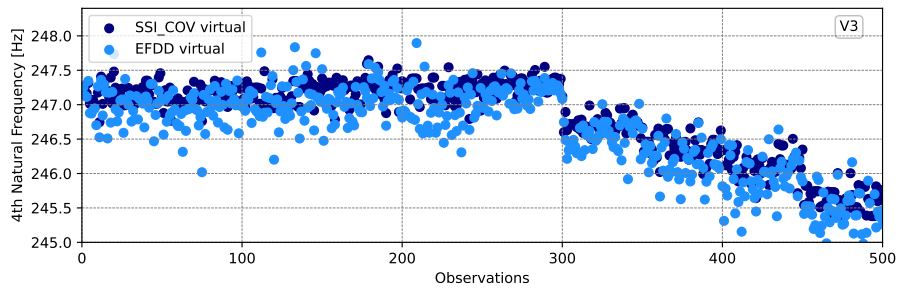
(d) 4th Natural Frequency for V3 – MDE.

Figure B.7. Comparison between each of the four first natural frequencies identified using SSI-COV and EFDD for all observations of the experimental application, for the case considering real sensors on top of the beam, virtual responses from MDE sensor V3 and damage on the bottom.

111
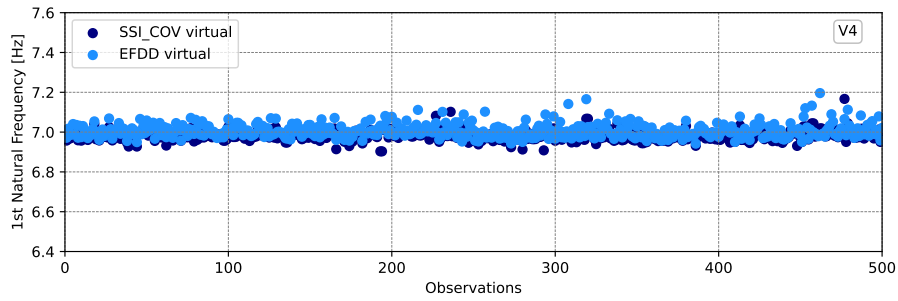
(a) 1st Natural Frequency for V4 – MDE.
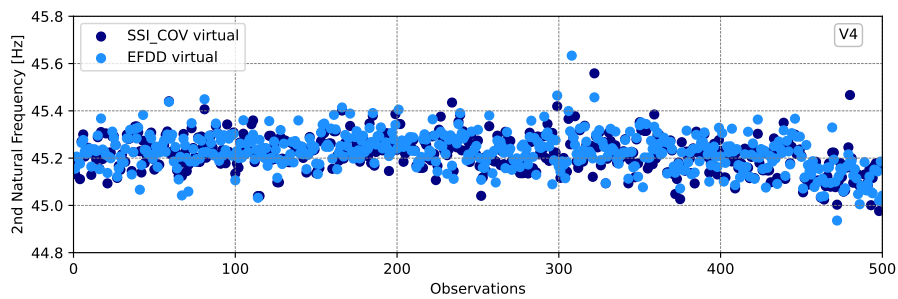
(b) 2nd Natural Frequency for V4 – MDE.
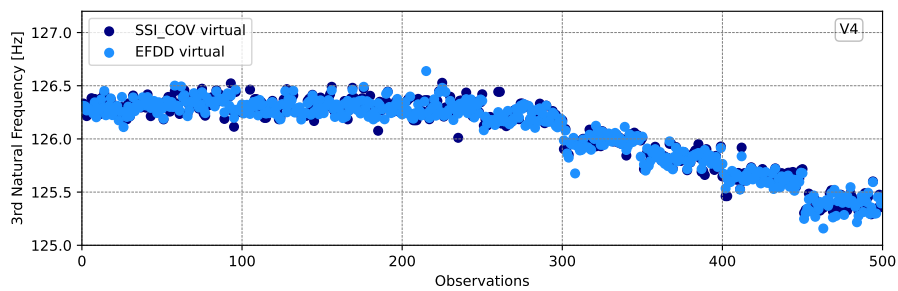
(c) 3rd Natural Frequency for V4 – MDE.
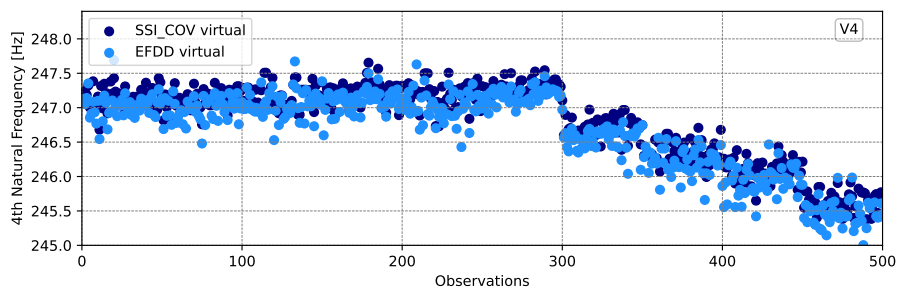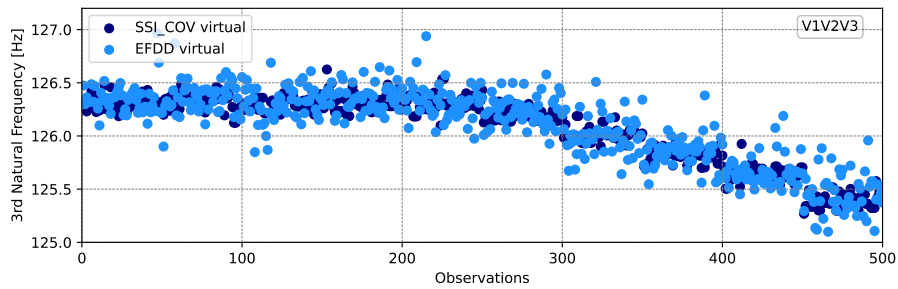

(d) 4th Natural Frequency for V4 – MDE.

Figure B.8. Comparison between each of the four first natural frequencies identified using SSI-COV and EFDD for all observations of the experimental application, for the case considering real sensors on top of the beam, virtual responses from MDE sensor V4 and damage on the bottom.
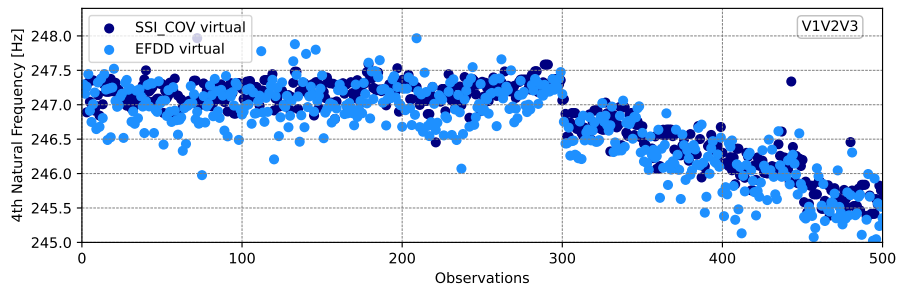
112
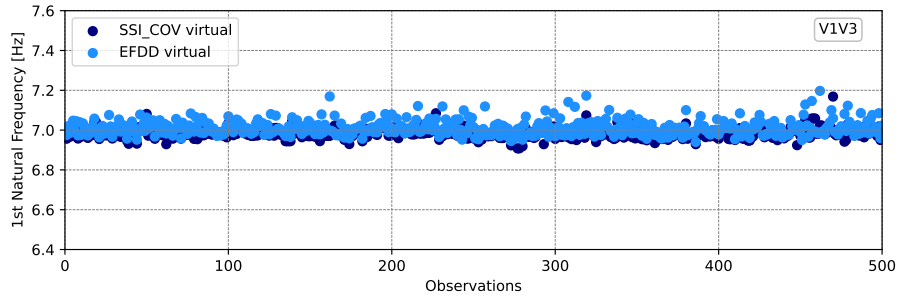
(a) 1st Natural Frequency for V1V3 – MDE.
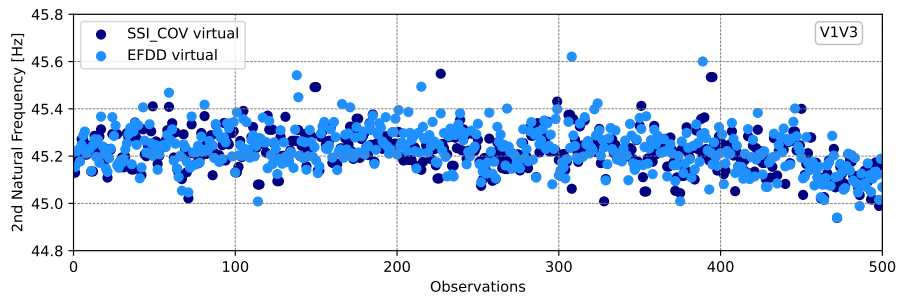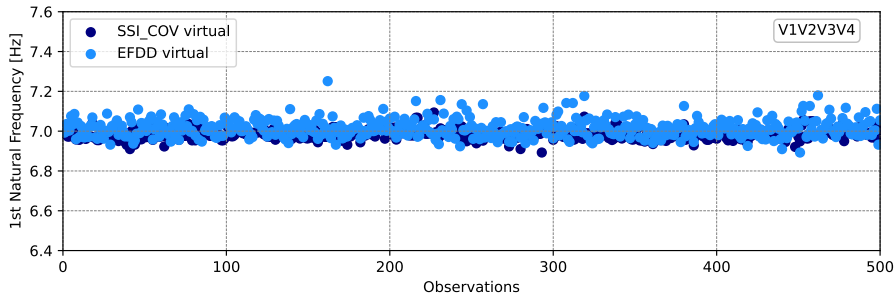

(b) 2nd Natural Frequency for V1V3 – MDE.
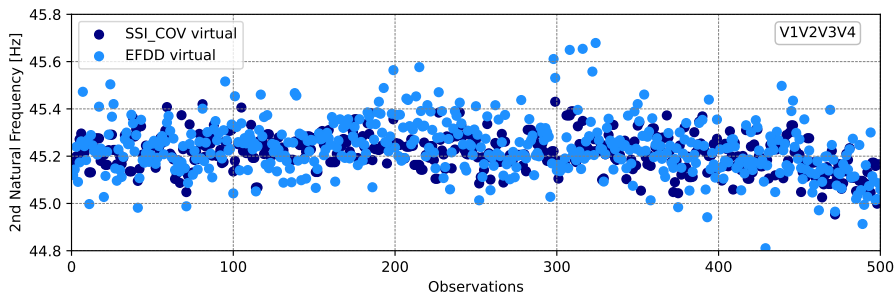

(c) 3rd Natural Frequency for V1V3 – MDE.
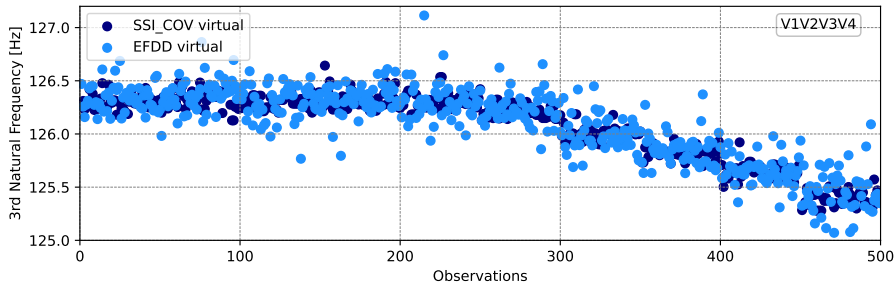

(d) 4th Natural Frequency for V1V3 – MDE.

Figure B.9. Comparison between each of the four first natural frequencies identified using SSI-COV and EFDD for all observations of the experimental application, for the case considering real sensors on top of the beam, virtual responses from MDE sensors V1V3 and damage on the bottom.

113

(a) 1st Natural Frequency for V2V3 – MDE.

(b) 2nd Natural Frequency for V2V3 – MDE.

(c) 3rd Natural Frequency for V2V3 – MDE.

(d) 4th Natural Frequency for V2V3 – MDE.

Figure B.10. Comparison between each of the four first natural frequencies identified using SSI-COV and EFDD for all observations of the experimental application, for the case considering real sensors on top of the beam, virtual responses from MDE sensors V2V3 and damage on the bottom.
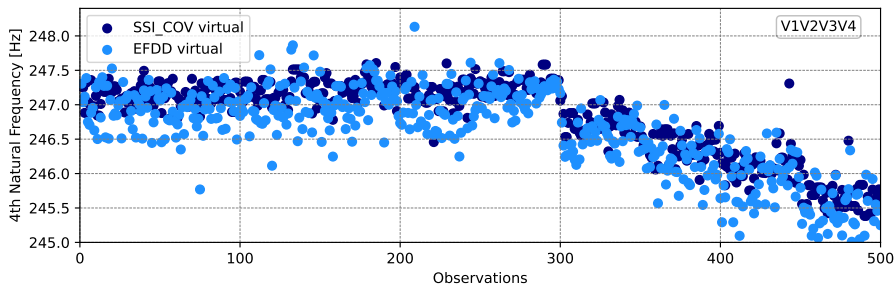
(a) 1st Natural Frequency for V1V2V3 – MDE.

(b) 2nd Natural Frequency for V1V2V3 – MDE.


(c) 3rd Natural Frequency for V1V2V3 – MDE.

(d) 4th Natural Frequency for V1V2V3 – MDE.

Figure B.11. Comparison between each of the four first natural frequencies identified using SSI-COV and EFDD for all observations of the experimental application, for the case considering real sensors on top of the beam, virtual responses from MDE sensors V1V2V3 and damage on the bottom.
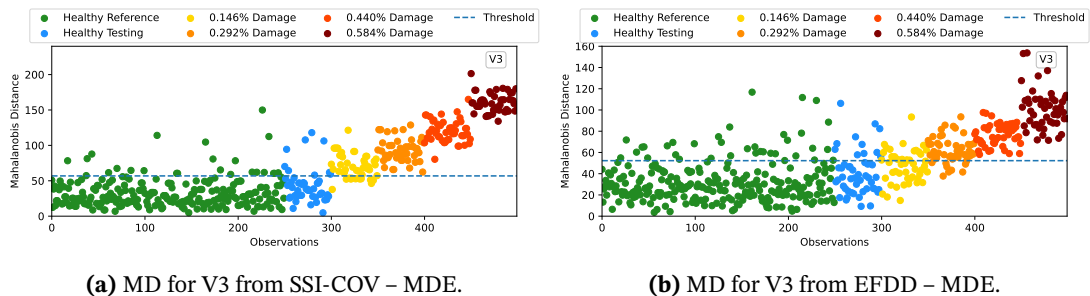
115

(a) 1st Natural Frequency for V1V2V3V4 – MDE.

(b) 2nd Natural Frequency for V1V2V3V4 – MDE.

(c) 3rd Natural Frequency for V1V2V3V4 – MDE.

(d) 4th Natural Frequency for V1V2V3V4 – MDE.

Figure B.12. Comparison between each of the four first natural frequencies identified using SSI-COV and EFDD for all observations of the experimental application, for the case considering real sensors on top of the beam, virtual responses from MDE sensors V1V2V3V4 and damage on the bottom.

(a) MD for V1 from SSI-COV – MDE.

(b) MD for V1 from EFDD – MDE.
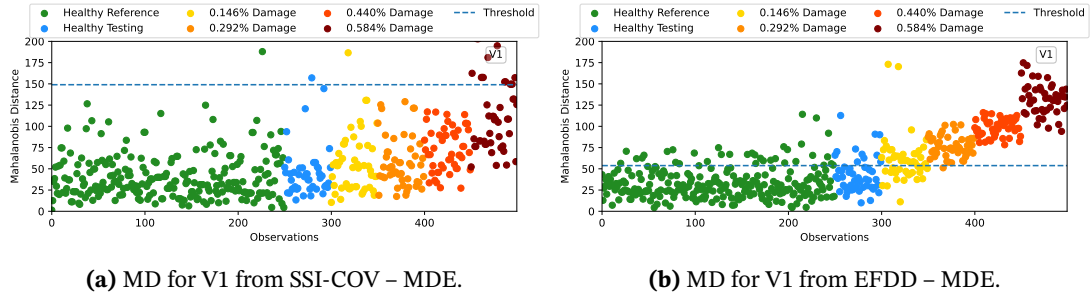
Figure B.13. Mahalanobis Distances obtained from the SSI-COV and the EFDD methods for all observations of the experimental application, considering the case where real sensors are placed on the top of the beam, virtual responses from MDE sensor V1 are added and damage is on the bottom.
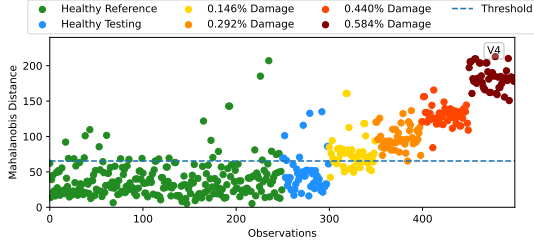

(a) MD for V2 from SSI-COV – MDE.

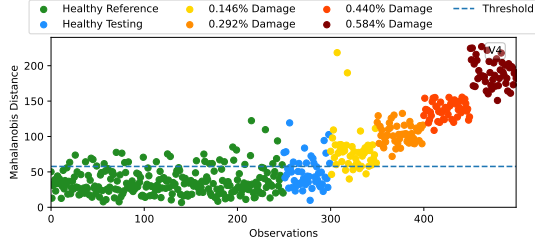**(b)** MD for V2 from EFDD – MDE.
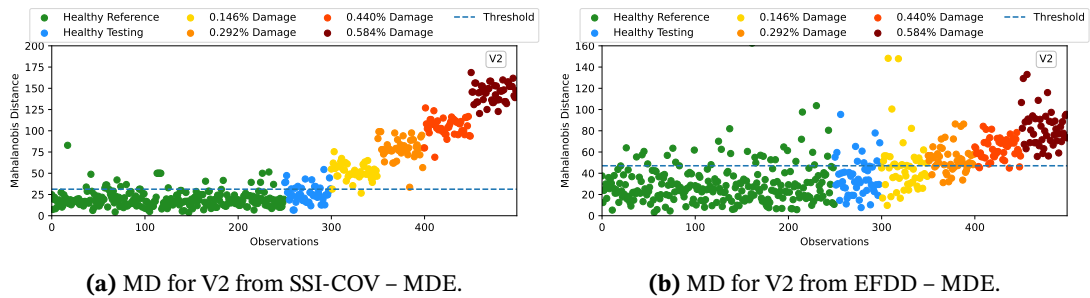
Figure B.14. Mahalanobis Distances obtained from the SSI-COV and the EFDD methods for all observations of the experimental application, considering the case where real sensors are placed on the top of the beam, virtual responses from MDE sensor V2 are added and damage is on the bottom.
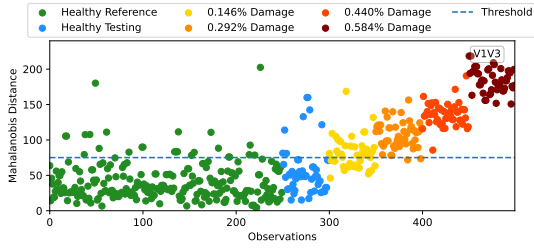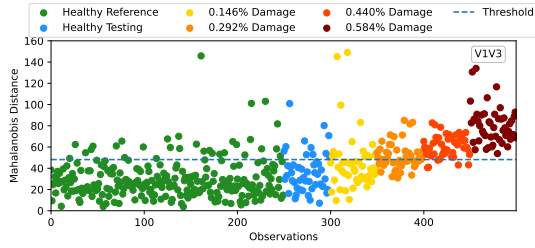

(a) MD for V3 from SSI-COV – MDE.

(b) MD for V3 from EFDD – MDE.

Figure B.15. Mahalanobis Distances obtained from the SSI-COV and the EFDD methods for all observations of the experimental application, considering the case where real sensors are placed on the top of the beam, virtual responses from MDE sensor V3 are added and damage is on the bottom.

117

(a) MD for V4 from SSI-COV – MDE.

(b) MD for V4 from EFDD – MDE.

Figure B.16. Mahalanobis Distances obtained from the SSI-COV and the EFDD methods for all observations of the experimental application, considering the case where real sensors are placed on the top of the beam, virtual responses from MDE sensor V4 are added and damage is on the bottom.
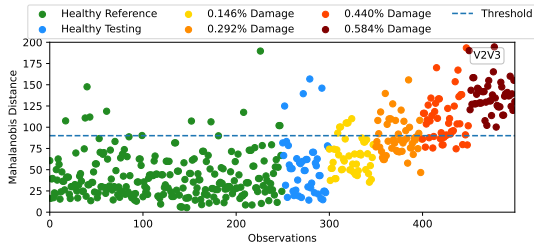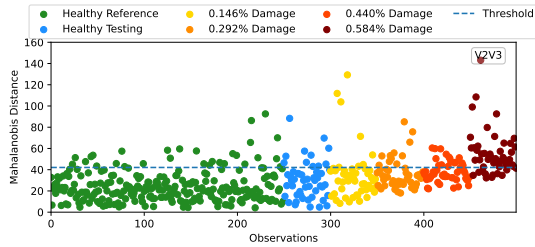

(a) MD for V1V3 from SSI-COV – MDE.

(b) MD for V1V3 from EFDD – MDE.

Figure B.17. Mahalanobis Distances obtained from the SSI-COV and the EFDD methods for all observations of the experimental application, considering the case where real sensors are placed on the top of the beam, virtual responses from MDE sensors V1V3 are added and damage is on the bottom.
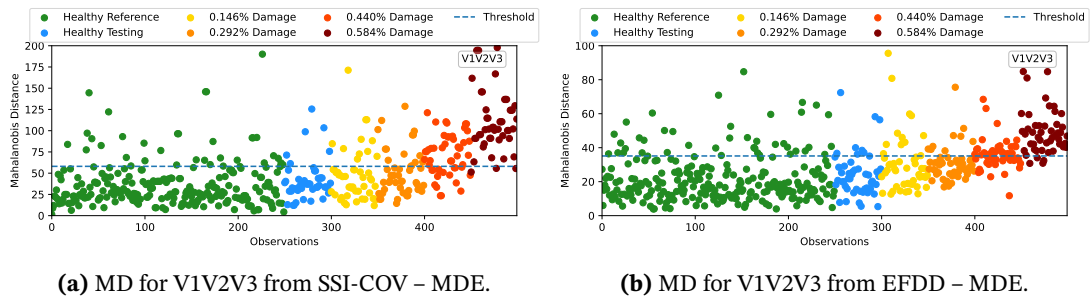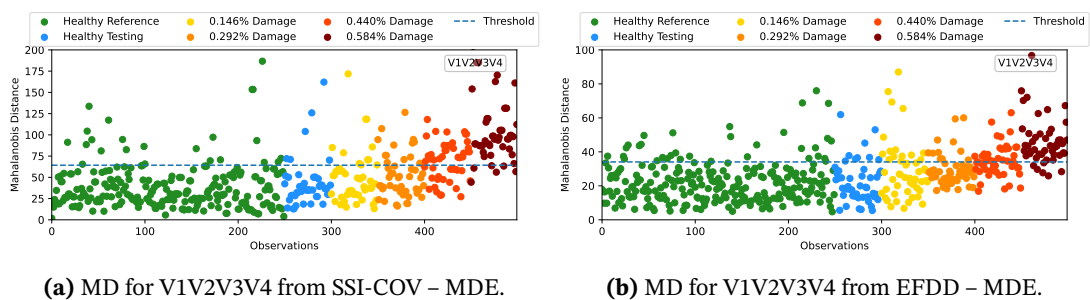

(a) MD for V2V3 from SSI-COV – MDE.

(b) MD for V2V3 from EFDD – MDE.

Figure B.18. Mahalanobis Distances obtained from the SSI-COV and the EFDD methods for all observations of the experimental application, considering the case where real sensors are placed on the top of the beam, virtual responses from MDE sensors V2V3 are added and damage is on the bottom.

(a) MD for V1V2V3 from SSI-COV – MDE.

**(b)** MD for V1V2V3 from EFDD – MDE.

Figure B.19. Mahalanobis Distances obtained from the SSI-COV and the EFDD methods for all observations of the experimental application, considering the case where real sensors are placed on the top of the beam, virtual responses from MDE sensors V1V2V3 are added and damage is on the bottom.

(a) MD for V1V2V3V4 from SSI-COV – MDE.

(b) MD for V1V2V3V4 from EFDD – MDE.

Figure B.20. Mahalanobis Distances obtained from the SSI-COV and the EFDD methods for all observations of the experimental application, considering the case where real sensors are placed on the top of the beam, virtual responses from MDE sensors V1V2V3V4 are added and damage is on the bottom.
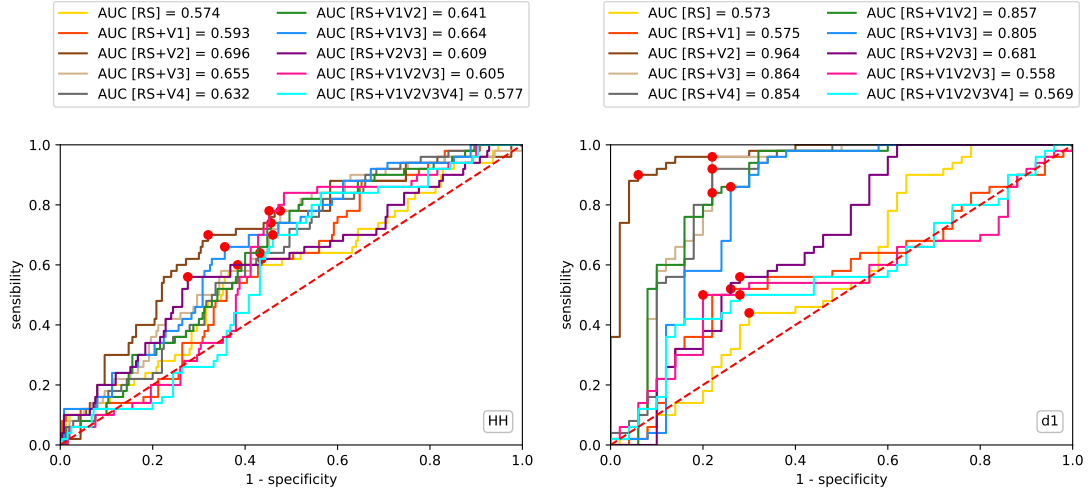
(a) AUC for undamaged observations from SSI-COV – MDE.

**(b)** AUC for the first damage level from SSI-COV – MDE.
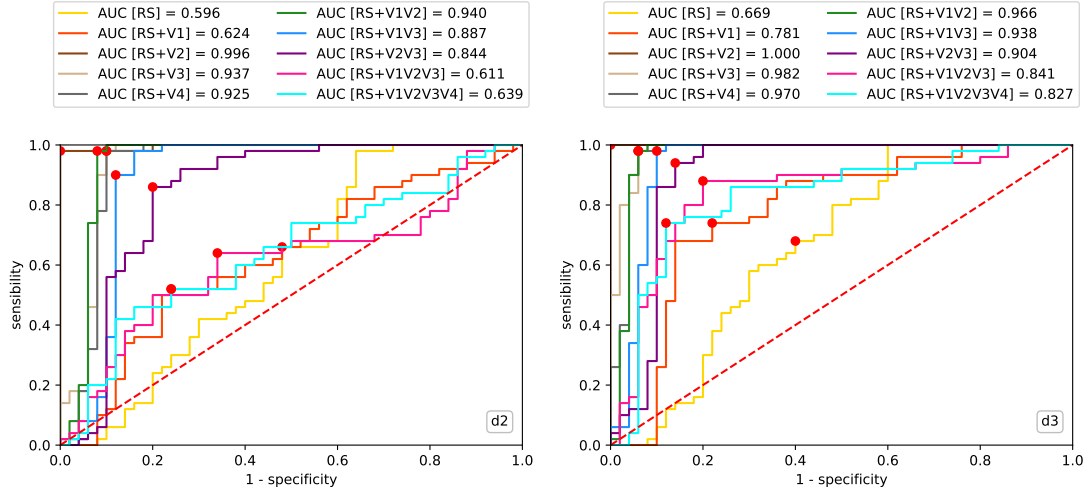
(c) AUC for the second damage level from SSI-COV – MDE.

**(d)** AUC for the third damage level from SSI-COV – MDE.

Figure B.21. Areas Under the Receiver Operating Curves obtained from the SSI-COV method for all observations and all virtual sensor combinations (undamaged and the three first damage levels applied), considering the experimental application, the case where real sensors are placed on the top of the beam, virtual sensors from MDE and damage on the bottom.

(a) AUC for undamaged observations from EFDD – MDE.

(b) AUC for the first damage value from EFDD – MDE.

(c) AUC for the second damage value from EFDD – MDE.

(d) AUC for the third damage value from EFDD – MDE.
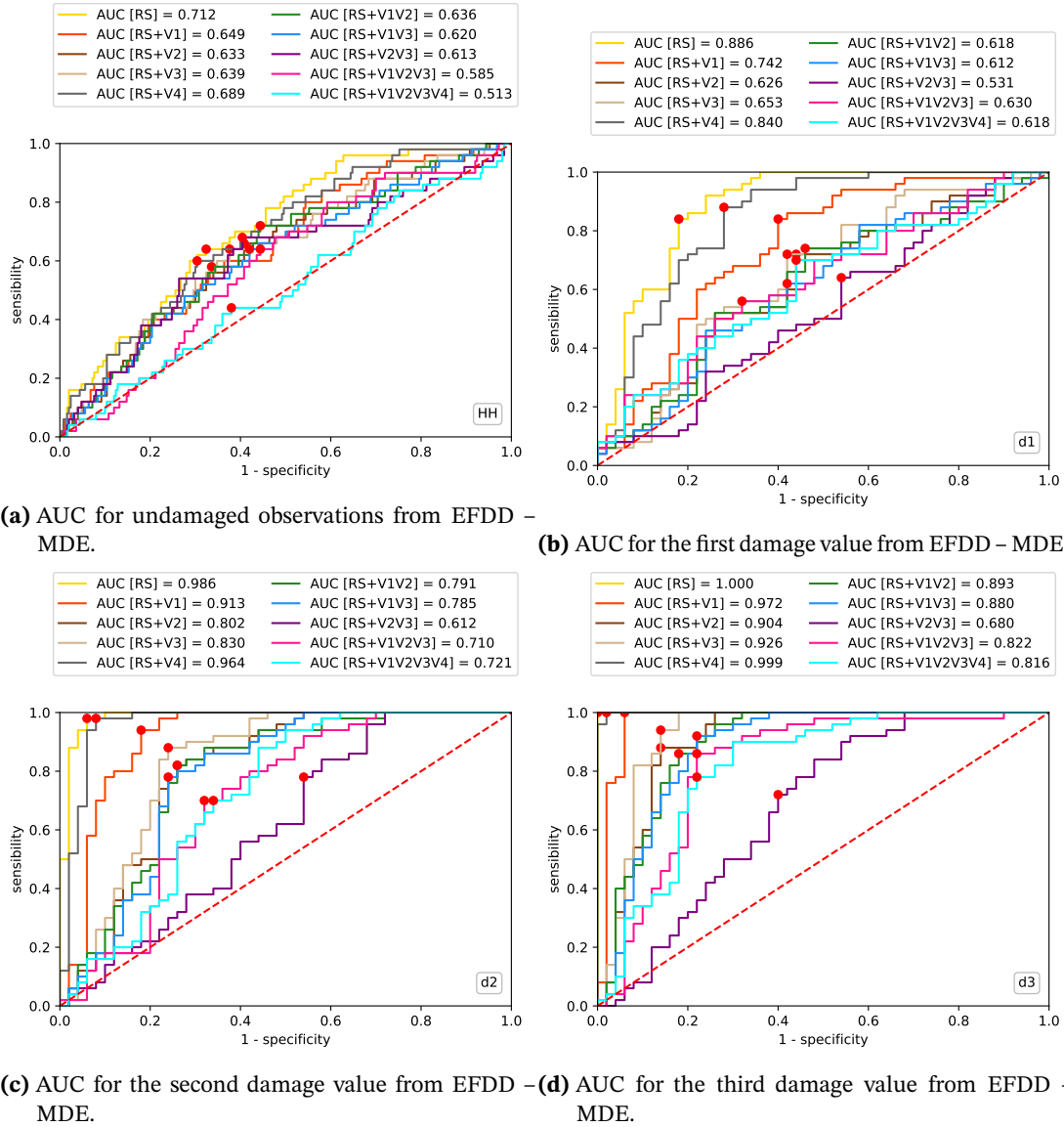
Figure B.22. Areas Under the Receiver Operating Curves obtained from the EFDD method for all observations and all virtual sensor combinations (undamaged and the three first damage values applied), considering the experimental application, the case where real sensors are placed on the top of the beam, virtual sensors from MDE and damage on the bottom.
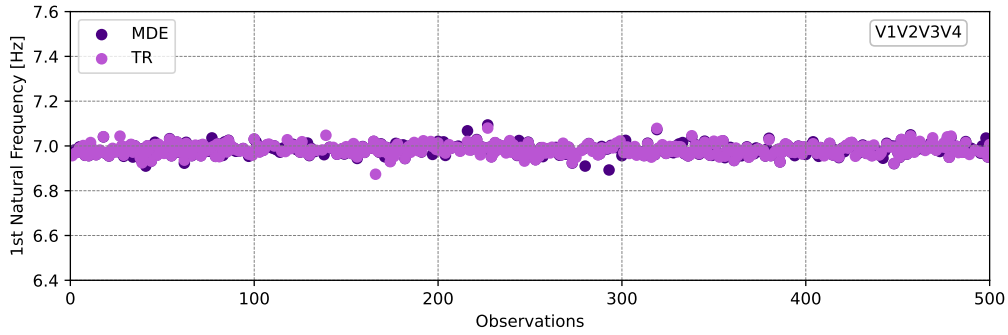
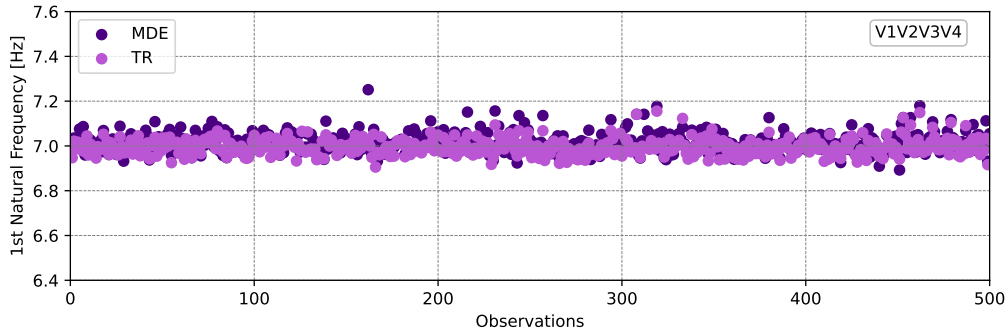**(a)** 1st Natural Frequency comparison from SSI-COV for V1V2V3V4 between MDE and TR.
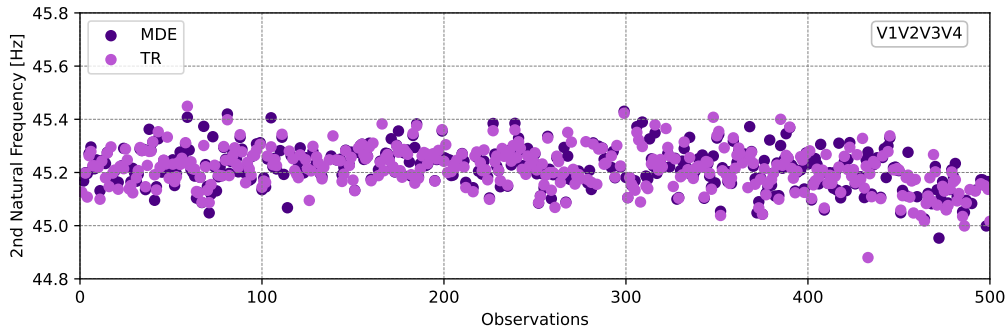
(b) 2nd Natural Frequency comparison from SSI-COV for V1V2V3V4 between MDE and TR.
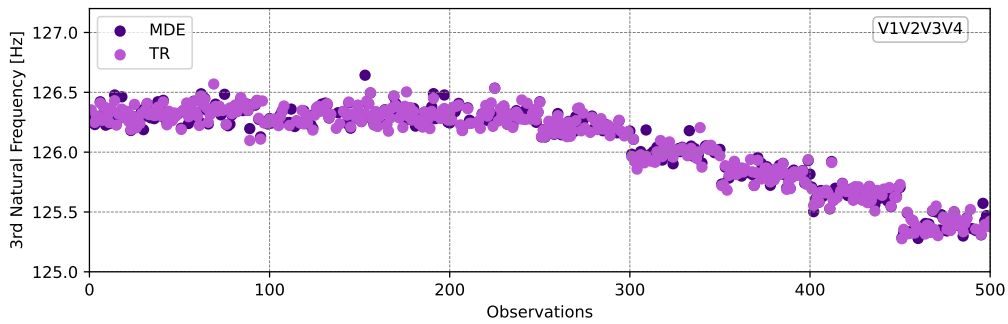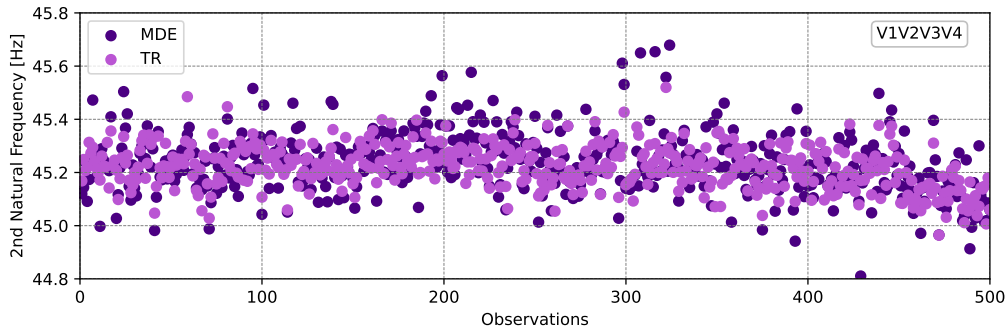

(c) 3rd Natural Frequency comparison from SSI-COV for V1V2V3V4 between MDE and TR.
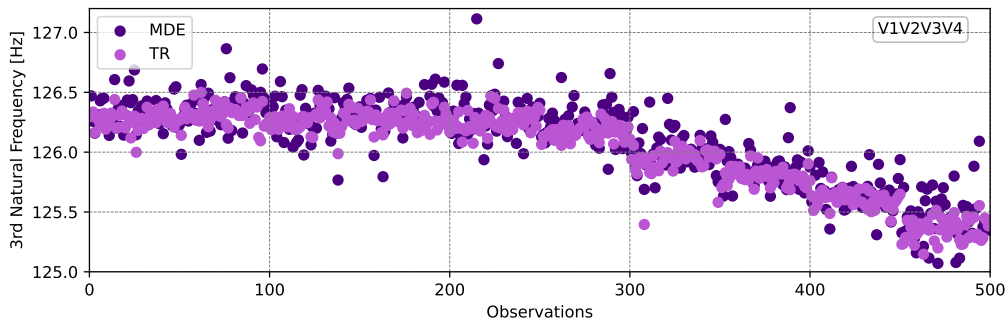
Figure B.23. Comparison between each of the first three natural frequencies identified using SSI-COV for MDE and Transmissibility (TR) expansions, for all observations of the Transmissibility numerical application, for the case considering real sensors on top of the beam, virtual responses from sensors V1V2V3V4 and damage on the bottom.

(a) 1st Natural Frequency comparison from EFDD for V1V2V3V4 between MDE and TR.

(b) 2nd Natural Frequency comparison from EFDD for V1V2V3V4 between MDE and TR.

(c) 3rd Natural Frequency comparison from EFDD for V1V2V3V4 between MDE and TR.

Figure B.24. Comparison between each of the first three natural frequencies identified using EFDD for MDE and Transmissibility (TR) expansions, for all observations of the Transmissibility numerical application, for the case considering real sensors on top of the beam, virtual responses from sensors V1V2V3V4 and damage on the bottom.